ALMA MATER STUDIORUM – UNIVERSITÀ DI BOLOGNA

DOTTORATO DI RICERCA IN BIOINGEGNERIA
Ciclo XXV

Settore concorsuale di afferenza: 09/G2
Settore scientifico disciplinare: ING-INF/06

Computational Modeling of Cardiac Excitation-Contraction Coupling in Physiological and Pathological Conditions

Presented by
Stefano Morotti

Ph.D. Coordinator
Prof. Angelo Cappello, Ph.D.

Supervisor
Prof. Mauro Ursino, Ph.D.

Reviewers
Prof. Gianni Gnudi
Prof. Massimiliano Zaniboni, Ph.D.

Co-Supervisor
Stefano Severi, Ph.D.

Year 2013, Final Exam

ACKNOWLEDGEMENTS

I owe my gratitude to all those people who have made this thesis possible and because of whom this experience has been one that I will cherish forever.

First, I would like to acknowledge my advisor, Dr. Stefano Severi, who introduced me to the world of scientific research. Thank you for your guidance, friendship, understanding, and support during these years.

I want to express my sincere gratitude also to the reviewers of this thesis and to all the Ph.D. committee members for their helpful suggestions through all stages of my doctoral studies.

My special thanks go to Dr. Donald Bers for welcoming me (many times) in Davis and guiding my research to meet his high standards.

I am most grateful to Dr. Ele Grandi, my unofficial mentor, for the time and energy spent in supporting me as well as her commitment to my projects. Your help and friendship have been invaluable for me.

Finally, I would like to thank all the other precious collaborators I have been honored to work with for their fundamental contributions to the achievement of the results which this thesis will present.

KEYWORDS

Computational Biology

Cardiac Electrophysiology

Excitation-Contraction Coupling

Ventricular Myocytes

Arrhythmogenesis

ABSTRACT

The cardiomyocyte is a complex biological system where many mechanisms interact non-linearly to regulate the coupling between electrical excitation and mechanical contraction. For this reason, the development of mathematical models is fundamental in the field of cardiac electrophysiology, where the use of computational tools has become complementary to the classical experimentation. My doctoral research has been focusing on the development of such models for investigating the regulation of ventricular excitation-contraction coupling at the single cell level. In particular, the following researches are presented in this thesis:

1) Study of the unexpected deleterious effect of a Na channel blocker on a long QT syndrome type 3 patient. Experimental results were used to tune a Na current model that recapitulates the effect of the mutation and the treatment, in order to investigate how these influence the human action potential. Our research suggested that the analysis of the clinical phenotype is not sufficient for recommending drugs to patients carrying mutations with undefined electrophysiological properties.

2) Development of a model of L-type Ca channel inactivation in rabbit myocytes to faithfully reproduce the relative roles of voltage- and Ca-dependent inactivation. The model was applied to the analysis of Ca current inactivation kinetics during normal and abnormal repolarization, and predicts arrhythmogenic activity when inhibiting Ca-dependent inactivation, which is the predominant mechanism in physiological conditions.

3) Analysis of the arrhythmogenic consequences of the crosstalk between β-adrenergic and Ca-calmodulin dependent protein kinase signaling pathways. The descriptions of the two regulatory mechanisms, both enhanced in heart failure, were integrated into a novel murine action potential model to investigate how they concur to the development of cardiac arrhythmias.

These studies show how mathematical modeling is suitable to provide new insights into the mechanisms underlying cardiac excitation-contraction coupling and arrhythmogenesis.

CONTENTS

INTRODUCTION

The term "excitation-contraction coupling" describes the fundamental electrophysiological process that links the electrical stimulation and the mechanical contraction in a muscle cell. Given the impact of heart diseases in the developed societies, a deep investigation of the mechanisms underlying cardiac excitation-contraction coupling and its derangements is extremely important. In the past 60 years, the research in cardiac electrophysiology has been benefiting from the use of mathematical models, now commonly adopted to support and drive the classical experimental work. Here, I will summarize the foundations of computational cardiac electrophysiology and provide with an outline of the subsequent chapters of this thesis.

Historical development of experimental electrophysiology

Electrophysiology is the branch of physiology that deals with the electrical properties of excitable cells and tissues (such as neurons and muscles). The history of this field dates back to the 17th century, when Jan Swammerdam first induced the contraction in a frog leg muscle by stimulating a nerve (Cobb, 2002). Swammerdam came close to understanding the nature of signal propagation between nerve and muscle, but at that time, the theory of electricity was still at its dawn. In fact, only about 100 years later, Benjamin Franklin, believed by many to be the "father of electricity", performed his famous experiment of flying a kite during a thunderstorm. At the end of 18th century, Luigi Galvani proposed his theory of electrical excitation of biological tissues (Galvani, 1791). He observed the relationship between stimulus density and muscle contraction, described the muscle refractoriness, and demonstrated the propagation of the stimulus, or action potential (AP). Galvani first hypothesized the existence of ion channels, described as water-filled channels penetrating into the fibers to allow excitability. Although the innovative concept of "animal electricity" proposed by Galvani has been initially countered by Alessandro Volta (a physicist known for the invention of the electric battery), it rapidly spread throughout Europe, also because of new findings by Giovanni Aldini, Galvani's nephew, which reinforced the theory of electrical excitation of biological tissue (Aldini, 1804) by studying the stimulation of body parts of freshly executed criminals. Furthermore, his experiments made a strong impact on the public opinion (Verkhratsky *et al.*, 2006), inspiring even the famous Mary Shelley's "Frankenstein" (1817).

Table 1. Perspectives of historical development of electrophysiology. From (Verkhratsky *et al.*, 2006; Luderitz, 2009; Priori, 2010).

Year	Event
1660s	Swammerdam pioneered the frog nerve muscle preparation.
1790s	Galvani developed the theory of electrical excitation of biological tissues, speculating about the existence of ion channels .
1800s	Aldini applied electrical currents to mammalian brains, reinforcing Galvani's theory.
1828	Nobili instrumentally recorded animal electricity using an electromagnetic galvanometer
1840s	Matteucci demonstrated AP-induced muscle contraction, and measured the resting current between the intact and cut surface of the muscle potential.
1848-1884	Du Bois-Reymond correctly interpreted Matteucci's experiments and refined the methods to record muscle currents from frogs and humans.
1850s	Von Helmotz determined the AP propagation speed along the nerve cell.
1868	Bernstein made the first true recordings of resting and action potentials.
1887	Waller first studied the electrical phenomena of the heart and recorded the first human ECG.
1895	Langendorff pioneered the isolated perfused mammalian heart.
1896-1902	Nernst electrolytic theory has been adopted to explain the membrane excitability by Bernstein and Overton and it has been suggested that the AP results from the exchange of Na and K cations.
1902	Einthoven developed the first practical ECG.
1910s	Morgan demonstrated that genes are carried on chromosomes and are the mechanical basis of heredity.
1925	Gorter and Grendel found the bilayer structure of the cellular membranes.
1930s	Pioneering experiments on Chara and Nitella (algae in the family Characeae) by Harris, Osterhout, and Hill.
1936	Young introduced the squid axon into physiological practice.
1939	Cole and Curtis directly measured the giant squid axon AP by performing impedance measurements.
1943	Hämmerling discovered the role of the nucleus as the repository of genetic information in eukaryotes.
1944	Avery, McLeod and McCarty identified the molecule responsible for transformation as DNA.
1949	Cole and Marmont developed the voltage-clamp technique.
1952	Hodgkin and Huxley formulated the ionic theory of membrane excitation, and developed a squid axon AP model.
1953	Watson and Crick determined the DNA double helix structure.
1960	Noble developed the first cardiac AP model.
1960s	Nirenberg, Khorana and Holley discovered the genetic code.
1963	Müller and Rudin measured ion currents in artificial lipid membranes.
1976	Neher and Sakmann developed the patch-clamp technique.
1977	Sanger developed the “chain termination” method for sequencing DNA. McAllister, Noble, and Tsien developed the first ventricular AP model.
1980	Discovery of giga-seal between micropipette tip and surface cell membrane.
1983	Mullis developed the polymerase chain reaction.
1990s	Development of species-specific ventricular AP models, and introduction of Markov models.
1995	The Keating group identified mutations responsible for long QT syndrome.

During the following century many scientists gave important contributions to the progress of experimental electrophysiology (Table 1), both by developing new instruments and by providing novel interpretations of observed phenomena. Thus, by the mid-1930s, the fundamental features of AP were already known, the structure of the cell membrane was identified and the existence of ion channels suggested. The introduction of the giant squid axon into physiological practice allowed the first direct measures of APs by Cole and Curtis (Cole & Curtis, 1939), obtained by performing impedance measurements (first using extracellular, and then intracellular electrodes). About 10 years later, the voltage-clamp technique has been developed by Cole (Cole, 1949) and Marmont (Marmont, 1949), and applied by Hodgkin and Huxley to formulate the ionic theory of membrane excitation (Hodgkin & Huxley, 1952; Hodgkin *et al.*, 1952), which demonstrated that membrane excitability is determined by passive ion fluxes, according to their electro-chemical gradients. The importance of their findings has also been recognized by the Nobel committee in 1963, when the Hodgkin and Huxley were awarded with the Nobel Prize in Physiology or Medicine.

Moreover, the Hodgkin and Huxley theory implied the existence of ion channel currents, whose instrumental recordings required to overcome several technical barriers, like the need to access mammalian cells, to control both the extra- and intracellular environments, and, above all, to deal with electrical signals characterized by a very small amplitude and a strong noise (Verkhratsky *et al.*, 2006). The improvement in measurement techniques culminated with the development of the patch-clamp technique (Neher & Sakmann, 1976; Sigworth & Neher, 1980), which allowed the systematic measurement of ion currents and entirely new types of electrophysiological experiments. Patch-clamp technique became not only the workhorse of modern electrophysiology (Petersen *et al.*, 2005), but also one of the most important techniques for the study of signal-transduction mechanisms. Thus, Neher and Sakmann, the developers of this technique, received the Nobel Prize in Physiology or Medicine in 1991.

The 20th century saw also the parallel development of modern genetics. Although genes were known to exist on chromosomes, only in the 1940s the role of DNA as molecule responsible for inheritance has been discovered. In 1953 Watson and Crick (then awarded with the Nobel Prize in Physiology or Medicine in 1962) determined the double helix structure of DNA (Watson & Crick, 1953), suggesting the fundamental mechanisms of DNA semi-conservative duplication (based on the separation of the two strands and the following reconstruction of two DNA filaments). How DNA influences the behavior of cells became clear only in the 1960s, when the studies of Nirenberg, Khorana and Holley (Nobel Prize in Physiology or Medicine in 1968) contributed to discover the role of RNA, messenger created from the DNA and responsible for protein synthesis (Rammler & Khorana, 1962; Nirenberg & Leder, 1964; Holley *et al.*, 1965). With the understanding of the genetic code, the introduction of the Sanger method for sequencing DNA (Sanger & Coulson, 1975) and the development of the polymerase chain reaction for isolating and amplifying a specific section of a DNA (Mullis & Faloona, 1987), scientific research accelerated and, in late 1980s, the search for disease-causing mutations started. Like several other fields, electrophysiology has been strongly impacted by the innovation brought by these techniques (Priori, 2010). The search for the genetic bases of inherited arrhythmogenic diseases was initiated by the Keating group, that first identified genomic mutations able to disrupt structure and function of cardiac ion channels and to cause life threatening arrhythmias (Curran *et al.*, 1995). Thus, the concept

of "cardiac channelopathies" emerged, leading to the redefinition of the paradigms for management of patients with inherited arrhythmogenic diseases.

Hodgkin and Huxley laid the foundation for the use of integrative models in biology, that have been progressively developed (and widely used) in the second half of 20th century. The close interplay between model development and experimentation, together with the improvement in laboratory instrumentations and the introduction of novel techniques (such as patch-clamp and genetic manipulation), led to the discovery of a great number of cellular structures and regulatory mechanisms, thus to a deeper comprehension of the behavior of the cardiomyocyte both in health and in disease (Grandi & Bers, in press).

ECC in ventricular myocyte

Cardiac excitation-contraction coupling (ECC) is the physiological process that links the electrical excitation of the membrane potential (E_m) to the consequent mechanical contraction of the myocyte. ECC is mediated by Ca (Fig. 1, inset), an universal intracellular second messenger that is released in the cytosol at every beat to directly activate the myofilaments (Bers, 2001).

Under physiological conditions and in absence of excitation, ventricular cells maintain a relatively stable E_m of about -85 mV (resting potential). When an excitatory stimulus depolarizes the membrane beyond the threshold potential (about -70 mV), an AP is produced (Fig. 1, inset). The AP is manifest as a propagating wave of transient depolarization (ten Eick

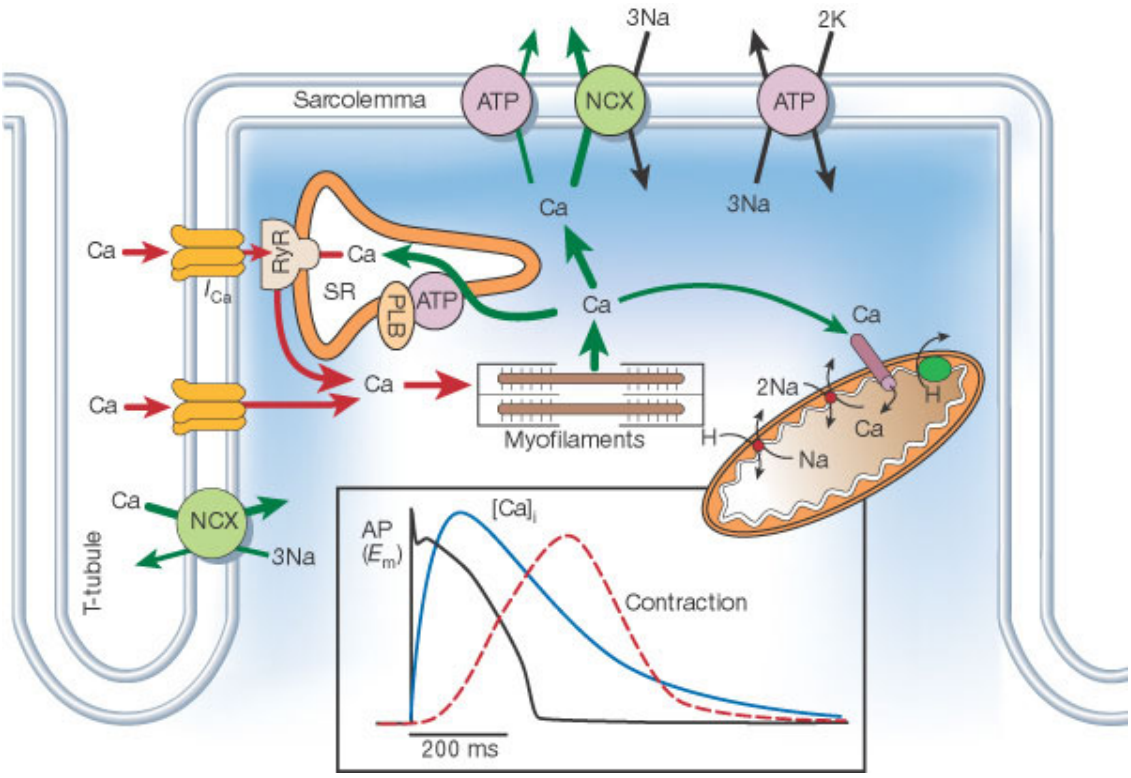

Figure 1. Schematic representation of cardiac ECC. Main panel summarizes Ca transport mechanisms in ventricular myocytes; inset shows the time course of AP, CaT and contraction measured in a rabbit ventricular myocyte at 37°C. From (Bers, 2002).

et al., 1992), and arises as a result of the dynamic behavior of a diverse population of membrane ion channels. Thus, the AP is characterized by different morphologies across the regions of the heart (Fig. 2) and in different species. Ventricular AP in human (depicted in Fig. 3A) is similar to that in rabbit (Fig. 1, inset), and exhibits a steep upstroke (phase 0), followed by a brief steep repolarization (phase 1) and a sustained slowly decaying plateau phase (2). The plateau phase is followed by a steeper repolarization (phase 3) that restores the resting potential (phase 4) (Grandi & Bers, in press).

Depolarization to the threshold potential activates Na channels and results in a large Na current (I_{Na}, Fig. 3B), responsible for the AP upstroke, which quickly inactivates. Upon membrane depolarization, L-type Ca current (I_{Ca}, Fig. 3B) activates as well, but inactivates slowly and incompletely, allowing for the inward I_{Ca} to balance the outward K currents and maintain the plateau phase of the AP. About the 90% of the L-type Ca channels (LTCCs) are localized in the transverse-tubules (t-tubules), deep invaginations of the sarcolemma (Fig. 1), and this particular localization facilitates the Ca entered via LTCC to trigger the Ca release from the sarcoplasmic reticulum (SR). This phenomenon is called Ca-induced Ca release (CICR) and is mediated by the ryanodine receptors (RyRs), that are sensitive to Ca in the dyadic space (the space between t-tubules and SR). During diastole, most of the intracellular Ca is stored in the SR. Once CICR occurs, Ca is free to diffuse throughout the sarcomere, where it binds to the Ca binding protein troponin in the myofilaments and initiates cell contraction, then the SR actively resequesters Ca via the sarco/endoplasmatic reticulum Ca pump (SERCA).

Membrane repolarization is mainly due to various types of K currents (Fig. 3C): the transient outward currents (I_{to} and I_{ClCa}, carried by K and Cl respectively) determine the notch that follows the upstroke, the components of the delayed rectifier K current (I_{Kr} and I_{Ks})

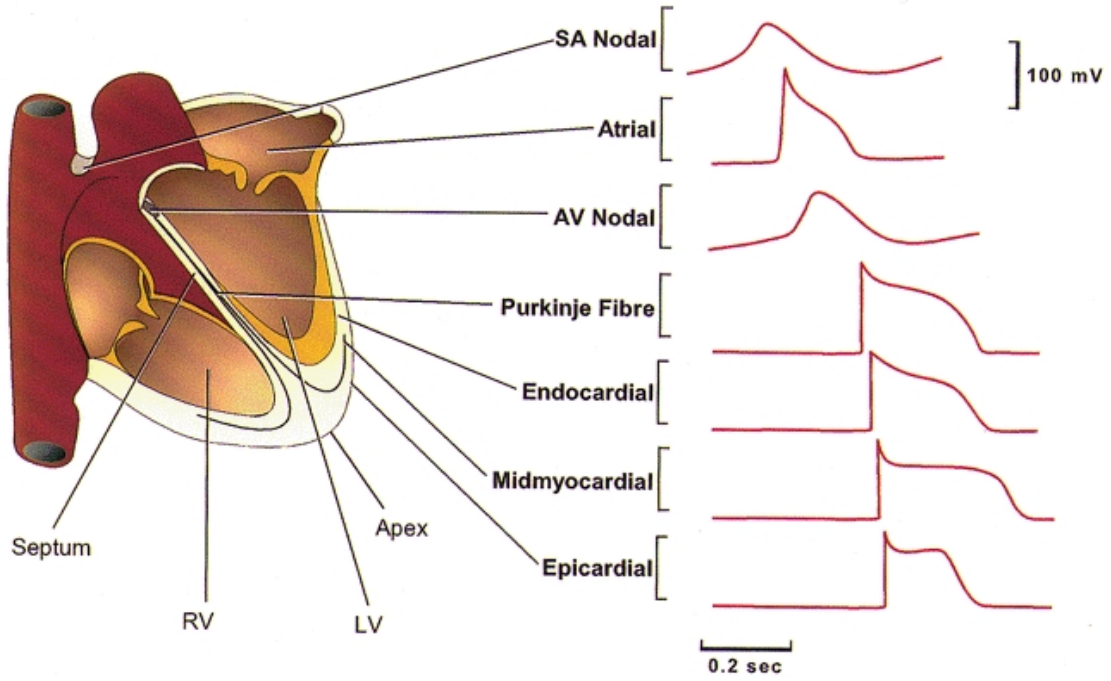

Figure 2. AP waveforms in different regions of the heart. AP waveforms are displaced in time to reflect the temporal sequence of propagation through the heart (SA, sino-atrial node; AV, atrio-ventricular node; RV, right ventricle; LV, left ventricle). From (Nerbonne, 2000).

contribute to complete the repolarization, and the inward rectifier K current (I_{K1}) maintains the resting potential. Ca entered the cell is extruded by Na-Ca exchanger (NCX), that yields a net inward charge movement (I_{NaCa}, Fig. 3D) when 1 Ca cation (divalent) is exchanged for 3 Na cations (monovalent); also the plasma membrane Ca pump contributes to Ca extrusion and regulation of cytosolic intracellular [Ca] ($[Ca]_i$). The Na-K pump (NKA) generates an outward current (I_{NaK}, Fig. 3D) by extruding 3 Na ions and importing 2 K cations (monovalent) on each cycle (Grandi & Bers, in press).

While E_m influences $[Ca]_i$, changes in $[Ca]_i$ and Ca transporters in turn alter E_m. For example, the intracellular Ca transient (CaT) feeds back on the LTCC, mediating I_{Ca} inactivation, and therefore influences AP morphology. In pathological conditions, these mechanisms can also lead to triggered activity (Bers, in press), especially early and delayed

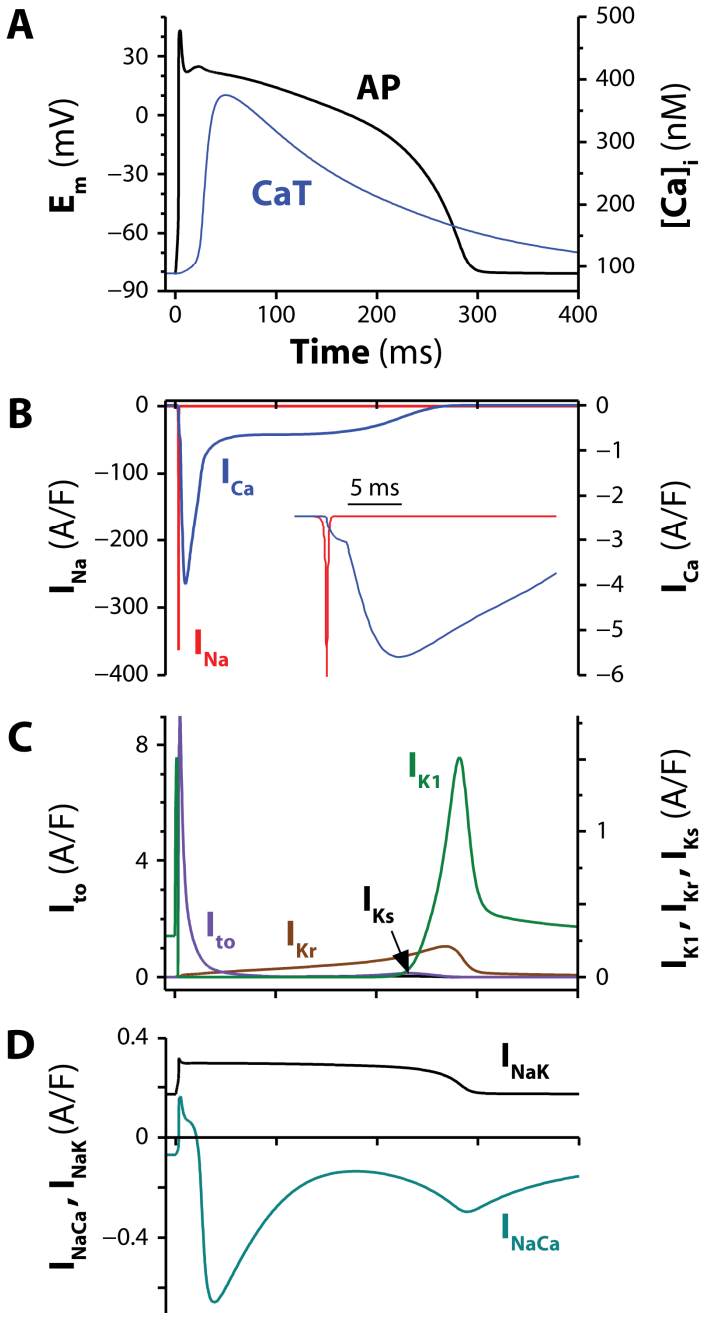

Figure 3. Schematic representation of ionic currents and CaT underlying the ventricular AP. Simulated (Grandi *et al.*, 2010) human ventricular AP and CaT (panel A), Na and Ca currents (B, inset shows the different activation and decay times), K currents (C), and NKA and NCX currents. Modified from (Grandi & Bers, in press).

afterdepolarizations (EADs and DADs). EADs and DADs are abnormal depolarizations of the cell membrane (respectively occurring during AP phases 2 or 3, and during phase 4) associated to the development of cardiac arrhythmias. DADs usually occur in a condition of Ca overload, where an increased Ca leak from the SR triggers Ca extrusion via NCX, which depolarizes the membrane (Priori & Corr, 1990). The same mechanism has also been associated to phase 3 EADs (Luo & Rudy, 1994b), that are characterized by low take-off potential. Phase 2 EADs are typically observed when the APD is prolonged (*e.g.*, I_{Kr} block or long QT syndromes), and are commonly associated to I_{Ca} reactivation during the prolonged plateau (January & Riddle, 1989; Luo & Rudy, 1994b; Zeng & Rudy, 1995).

Cardiac electrophysiology, contraction, metabolism, and gene regulation are also subject to modulation by a number of subcellular signaling pathways, which involve cascades of signaling molecules resulting in post-translational modifications (*e.g.*, phosphorylation) of target proteins (Grandi & Bers, in press). One of the most widely studied signaling pathways is that induced by β-adrenergic (βAR) receptor stimulation, whose macroscopic effect is an enhancement of cardiac function. At the single cell level, βAR regulation of ECC is mediated by the phosphorylation of a wide spectrum of target proteins (Bers, 2002), including LTCC, RyR, and phospholamban (PLB, which controls SERCA activity), which leads to an enhancement of CaT (and thus contraction). Recently, Ca-calmodulin dependent protein kinase (CaMKII) has emerged as important in ECC regulation (Maier & Bers, 2007), and its overexpression has been associated to pathological phenotypes. Furthermore, CaMKII and βAR signaling pathways are closely interrelated, since they share some phosphorylation targets and, above all, βAR stimulation can directly or indirectly (via enhanced intracellular Ca) activate CaMKII.

Modeling the mechanisms underlying ECC at the single cell level

The cardiomyocyte is a complex biological system where many regulatory mechanisms interact with dynamically changing ionic concentrations and varying E_m. These non-linear interactions make the single cell an interactive system where a high degree of synthesis and integration occurs (Rudy & Silva, 2006). Thus, analysis and synthesis of such complex systems can benefit from a mathematical approach.

The first computational AP model was formulated by Hodgkin and Huxley for the giant squid axon in 1952 (Hodgkin & Huxley, 1952; Hodgkin *et al.*, 1952), and has been used as the basis to develop many modern neuronal and cardiac AP models. In Hodgkin and Huxley (H&H) model the inward movement of Na is responsible for the strong positive deflection of the E_m observed in intracellular recordings, upon depolarization, while outward flow of K causes repolarization to the resting state. In this formulation the gating mechanisms regulate membrane permeability, whereby distinct entities (*i.e.* gates) controls the flux of both Na and K ions (Grandi & Bers, in press).

In the early 1960s Noble developed the first models of a cardiac myocyte AP (Noble, 1960, 1962), adapting the H&H formulation to the Purkinje cell. Since I_{Ca} had not yet been discovered at that time, the plateau was supported by inward Na flux. LTCC model was introduced only in the 1975 (McAllister *et al.*, 1975), and the idea that a balance between K and Ca currents maintains the plateau was reinforced in the first computational ventricular

myocyte model (Beeler & Reuter, 1977). Aspects of intracellular Ca handling were first introduced in the Purkinje cell in 1985 (DiFrancesco & Noble, 1985). In 1994 Luo and Rudy published a ventricular AP model (Luo & Rudy, 1994b, a) that included the intracellular SR compartment, time varying intracellular ion concentrations, and ion pumps and exchangers. The Luo-Rudy model (Luo & Rudy, 1994a) became one of the landmarks in the development of computational ventricular electrophysiology. Based on data recorded mostly in guinea pig, it was formulated using the traditional H&H scheme.

More recently, a large body of knowledge has been accumulated on the relationships between ion channel structure and function, the kinetic properties of single ion channels, and the modification of ion channel structure and function by genetic defects (Nickerson & Hunter, 2010). Thus, a major challenge has been the integration of new findings into the AP model in order to mechanistically relate molecular level findings to whole cell function, and it has become clear that models with explicit representation of single ion channel states are required. For this reason, Markov models have been adopted (Clancy & Rudy, 1999, 2002) to replace the H&H formulation (where the gating parameters do not represent specific kinetic states of ion channels). Markov models are based on the assumption that transitions between channel states depend on the present conformation of the channel, but not on previous behavior. As the molecular interactions of channels are often state-dependent, Markov model transitions typically represent specific channel movements that have been characterized experimentally (Rudy & Silva, 2006).

While most of the early AP models generically integrated experimental data from mammalian hearts (mostly guinea pig), many electrophysiological studies had shown species differences in AP waveforms and ionic currents. Thus, based on data obtained from isolated cells from one particular species, ventricular AP models have been developed for mouse (Bondarenko *et al.*, 2004; Li *et al.*, 2010), rat (Pandit *et al.*, 2001), rabbit (Puglisi & Bers, 2001; Shannon *et al.*, 2004; Mahajan *et al.*, 2008), and dog (Winslow *et al.*, 1999; Greenstein *et al.*, 2000; Hund & Rudy, 2004). The first human ventricular cell model was developed by Priebe and Beuckelmann (Priebe & Beuckelmann, 1998), adapting the major ionic currents of the Luo-Rudy model to the data available for human ventricular cells. More recently developed human models (Iyer *et al.*, 2004; ten Tusscher *et al.*, 2004; ten Tusscher & Panfilov, 2006; Grandi *et al.*, 2010; O'Hara *et al.*, 2011) included new measured data in human, providing a more accurate description of electrophysiological properties and Ca and Na handling in the human ventricular myocyte.

The Ca handling system was represented in the Luo-Rudy model by a phenomenological description (mimicking CICR) unable to capture the biophysical details involved (Grandi & Bers, in press). In 1998 Jafri *et al.* incorporated in a model of the guinea pig ventricular myocyte mechanistic Markov models for both LTCCs and RyRs and a restricted subspace (a single compartment representing the total volume of all dyads) into which all Ca fluxes through these channels are directed (Jafri *et al.*, 1998). This "common pool" model, whereby sarcolemmal Ca influx enters the same Ca pool into which SR Ca is released and by which is regulated, cannot reproduce both high gain and graded release (Stern, 1992), that arises from local stochastic interactions between LTCCs and RyRs in thousands of Ca release units. In 2002 Greenstein and Winslow (Greenstein & Winslow, 2002) developed a comprehensive model of the ventricular myocyte based on the theory of local control of SR Ca release. Another cytosolic Ca compartment (sub-sarcolemma) has been

then introduced (Shannon *et al.*, 2004), based on experiments suggesting that NCX senses elevated Ca levels (compared to the bulk [Ca]), contributing to the improvement of Ca handling description.

Thesis outline

Nowadays computational models play an important role in electrophysiology research and their use is complementary to that of classical experimentation. The general purpose of a model is to translate a set of hypotheses into predictions of observable events, and these predictions can be compared to observations, and the underlying hypotheses can be rejected or corroborated (Potse, 2012). In the past 50 years, many mathematical models of cardiac AP have been developed for different mammalian species and different heart regions, and successfully applied to test whether and how the known mechanisms contribute for all the experimentally observed phenomena, to predict the effects on cell function induced by a mutation (Clancy & Rudy, 1999), or to understand under which circumstances a cell would contribute to arrhythmogenesis (Kurata *et al.*, 2005). By coupling AP models together, it is possible to create tissue models in which study AP propagation and arrhythmia (Comtois *et al.*, 2008). Furthermore, it is possible to study the effect of modified cardiac activation on cardiac pump function, by integrating the electro-mechanical coupling, mechanical contraction, mechano-electric feedback (Trayanova & Rice, 2011).

The present thesis will focus on the regulation of AP and Ca handling, which comprehension is essential to understand cardiomyocyte physiology and arrhythmogenesis (Bers, in press). I will describe three projects, in which computational models have been developed to investigate different mechanisms underlying ventricular ECC in different mammalian species, both in physiological and pathological conditions.

The next chapter will describe the use of computational modeling in a clinical context. The clinicians treated a patient presenting the phenotype of long QT syndrome type 3 (LQT3, an inherited arrhythmogenic disease) with a drug commonly used as a LQT3 gene-specific therapy. Unexpectedly, administration of the drug worsened the patient conditions, thus a deeper investigation of the effects of the specific mutation was needed. Our collaborators from the group of Dr. Silvia Priori (at the Salvatore Maugeri Foundation, Pavia, Italy, and Leon H. Charney Division of Cardiology, New York University School of Medicine, USA) performed the characterization *in vitro*, while we investigated *in silico* the effects of both mutation and drug administration on the corresponding gene/protein (encoding the cardiac Na channel) and on the human ventricular AP.

The second project focused on the study of the biophysical properties of I_{Ca}, which is one of the most important players in cardiomyocytes electrophysiology. The inactivation of this current is regulated by both Ca- and voltage-dependent inactivation mechanisms (CDI and VDI). Since the inhibition of both mechanisms has been associated to perturbed cardiomyocyte function, understanding of how CDI and VDI contribute to total inactivation is critical. Different strategies have been adopted in both experimental and theoretical studies to differentiate between the two mechanisms, and their accuracy is debatable. In collaboration with researchers from the group of Dr. Donald M. Bers (at the Department of Pharmacology, University of California in Davis, USA), we analyzed those strategies to select the most

accurate one. Based on this, we identified and validated an improved model of LTCC inactivation in rabbit ventricular myocyte, which was applied to study the relative roles of CDI and VDI during normal and abnormal repolarization.

The third chapter will present a study carried out in the Bers Lab in collaboration with researchers from the group of Dr. Andrew D. McCulloch (at the Department of Bioengineering, University of California in San Diego, USA), with the aim of investigating the crosstalk between CaMKII and βAR signaling pathways in the context of heart failure (HF). It has been shown that both CaMKII expression and βAR tone are upregulated in HF, thus it is important to understand how their interaction could contribute to ECC regulation and arrhythmogenesis. To this aim, we developed a model of murine ventricular ECC, where descriptions of Ca, βAR and CaMKII signaling pathways are integrated. The use of transgenic mouse models has proven to be particularly appropriate in the context of HF, given the wealth of experimental data that can be measured in mice, but cannot be obtained as easily in humans. Our work established the basis for the development of a systematic framework that, accounting for electrophysiological differences among species, is necessary to extrapolate findings in the genetically engineered mouse to the most relevant clinical setting.

References

Aldini G. (1804). *Essai théorique et expérimental sur le galvanisme*, vol. 2. Fournier et Fils, Paris.

Beeler GW & Reuter H. (1977). Reconstruction of the action potential of ventricular myocardial fibres. *The Journal of physiology* **268,** 177-210.

Bers DM. (2001). *Excitation-contraction coupling and cardiac contractile force*. Kluwer Academic Publishers, Dordrecht ; Boston.

Bers DM. (2002). Cardiac excitation-contraction coupling. *Nature* **415,** 198-205.

Bers DM. (in press). Excitation-Contraction Coupling. In *Cardiac Electrophysiology: From Cell to Bedside*, 6th edn, ed. Zipes DP & Jalife J. Expert Consult.

Bondarenko VE, Szigeti GP, Bett GC, Kim SJ & Rasmusson RL. (2004). Computer model of action potential of mouse ventricular myocytes. *American journal of physiology Heart and circulatory physiology* **287,** H1378-1403.

Clancy CE & Rudy Y. (1999). Linking a genetic defect to its cellular phenotype in a cardiac arrhythmia. *Nature* **400,** 566-569.

Clancy CE & Rudy Y. (2002). Na(+) channel mutation that causes both Brugada and long-QT syndrome phenotypes: a simulation study of mechanism. *Circulation* **105,** 1208-1213.

Cobb M. (2002). Timeline: exorcizing the animal spirits: Jan Swammerdam on nerve function. *Nature reviews Neuroscience* **3,** 395-400.

Cole KS. (1949). Dynamic electrical characteristics of the squid axon membrane. *Arch Sci Physiol* **3,** 253-258.

Cole KS & Curtis HJ. (1939). Electric Impedance of the Squid Giant Axon during Activity. *The Journal of general physiology* **22,** 649-670.

Comtois P, Sakabe M, Vigmond EJ, Munoz M, Texier A, Shiroshita-Takeshita A & Nattel S. (2008). Mechanisms of atrial fibrillation termination by rapidly unbinding Na+ channel blockers: insights from mathematical models and experimental correlates. *American journal of physiology Heart and circulatory physiology* **295,** H1489-1504.

Curran ME, Splawski I, Timothy KW, Vincent GM, Green ED & Keating MT. (1995). A molecular basis for cardiac arrhythmia: HERG mutations cause long QT syndrome. *Cell* **80,** 795-803.

DiFrancesco D & Noble D. (1985). A model of cardiac electrical activity incorporating

ionic pumps and concentration changes. *Philosophical transactions of the Royal Society of London Series B, Biological sciences* **307,** 353-398.

Galvani L. (1791). De viribus electricitatis in motu musculari commentarius. *Bon Sci Art Inst Acad Comm* **7,** 363–418.

Grandi E & Bers DM. (in press). Models of the Ventricular Action Potential in Health and Disease. In *Cardiac Electrophysiology: From Cell to Bedside*, 6th edn, ed. Zipes DP & Jalife J. Expert Consult.

Grandi E, Pasqualini FS & Bers DM. (2010). A novel computational model of the human ventricular action potential and Ca transient. *Journal of molecular and cellular cardiology* **48,** 112-121.

Greenstein JL & Winslow RL. (2002). An integrative model of the cardiac ventricular myocyte incorporating local control of Ca2+ release. *Biophysical journal* **83,** 2918-2945.

Greenstein JL, Wu R, Po S, Tomaselli GF & Winslow RL. (2000). Role of the calcium-independent transient outward current I(to1) in shaping action potential morphology and duration. *Circulation research* **87,** 1026-1033.

Hodgkin AL & Huxley AF. (1952). A quantitative description of membrane current and its application to conduction and excitation in nerve. *The Journal of physiology* **117,** 500-544.

Hodgkin AL, Huxley AF & Katz B. (1952). Measurement of current-voltage relations in the membrane of the giant axon of Loligo. *The Journal of physiology* **116,** 424-448.

Holley RW, Everett GA, Madison JT & Zamir A. (1965). Nucleotide Sequences in the Yeast Alanine Transfer Ribonucleic Acid. *The Journal of biological chemistry* **240,** 2122-2128.

Hund TJ & Rudy Y. (2004). Rate dependence and regulation of action potential and calcium transient in a canine cardiac ventricular cell model. *Circulation* **110,** 3168-3174.

Iyer V, Mazhari R & Winslow RL. (2004). A computational model of the human left-ventricular epicardial myocyte. *Biophys J* **87,** 1507-1525.

Jafri MS, Rice JJ & Winslow RL. (1998). Cardiac Ca2+ dynamics: the roles of ryanodine receptor adaptation and sarcoplasmic reticulum load. *Biophysical journal* **74,** 1149-1168.

January CT & Riddle JM. (1989). Early afterdepolarizations: mechanism of induction and block. A role for L-type Ca2+ current. *Circulation research* **64,** 977-990.

Kurata Y, Hisatome I, Matsuda H & Shibamoto T. (2005). Dynamical mechanisms of pacemaker generation in IK1-downregulated human ventricular myocytes: insights from bifurcation analyses of a mathematical model. *Biophysical journal* **89,** 2865-2887.

Li L, Niederer SA, Idigo W, Zhang YH, Swietach P, Casadei B & Smith NP. (2010). A mathematical model of the murine ventricular myocyte: a data-driven biophysically based approach applied to mice overexpressing the canine NCX isoform. *American journal of physiology Heart and circulatory physiology* **299,** H1045-1063.

Luderitz B. (2009). Historical perspectives of cardiac electrophysiology. *Hellenic journal of cardiology : HJC = Hellenike kardiologike epitheorese* **50,** 3-16.

Luo CH & Rudy Y. (1994a). A dynamic model of the cardiac ventricular action potential. I. Simulations of ionic currents and concentration changes. *Circulation research* **74,** 1071-1096.

Luo CH & Rudy Y. (1994b). A dynamic model of the cardiac ventricular action potential. II. Afterdepolarizations, triggered activity, and potentiation. *Circulation research* **74,** 1097-1113.

Mahajan A, Shiferaw Y, Sato D, Baher A, Olcese R, Xie LH, Yang MJ, Chen PS, Restrepo JG, Karma A, Garfinkel A, Qu Z & Weiss JN. (2008). A rabbit ventricular action potential model replicating cardiac dynamics at rapid heart rates. *Biophysical journal* **94,** 392-410.

Maier LS & Bers DM. (2007). Role of Ca2+/calmodulin-dependent protein kinase (CaMK) in excitation-contraction coupling in the heart. *Cardiovascular research* **73,** 631-640.

Marmont G. (1949). Studies on the axon membrane; a new method. *Journal of cellular physiology* **34,** 351-382.

McAllister RE, Noble D & Tsien RW. (1975). Reconstruction of the electrical activity of cardiac Purkinje fibres. *The Journal of physiology* **251,** 1-59.

Mullis KB & Faloona FA. (1987). Specific synthesis of DNA in vitro via a polymerase-catalyzed chain reaction. *Methods in enzymology* **155,** 335-350.

Neher E & Sakmann B. (1976). Single-channel currents recorded from membrane of denervated frog muscle fibres. *Nature* **260,** 799-802.

Nerbonne JM. (2000). Molecular basis of functional voltage-gated K+ channel diversity in the mammalian myocardium. *The Journal of physiology* **525 Pt 2,** 285-298.

Nickerson DP & Hunter PJ. (2010). Cardiac Cellular Electrophysiology Modeling. In *Cardiac Electrophysiology Methods and Models*, ed. Sigg DC, Iaizzo PA, Xiao YF & He B. Springer, Inc.

Nirenberg M & Leder P. (1964). Rna Codewords and Protein Synthesis. The Effect of Trinucleotides Upon the Binding of Srna to Ribosomes. *Science* **145,** 1399-1407.

Noble D. (1960). Cardiac action and pacemaker potentials based on the Hodgkin-Huxley equations. *Nature* **188,** 495-497.

Noble D. (1962). A modification of the Hodgkin--Huxley equations applicable to Purkinje fibre action and pace-maker potentials. *The Journal of physiology* **160,** 317-352.

O'Hara T, Virag L, Varro A & Rudy Y. (2011). Simulation of the undiseased human cardiac ventricular action potential: model formulation and experimental validation. *PLoS computational biology* **7,** e1002061.

Pandit SV, Clark RB, Giles WR & Demir SS. (2001). A mathematical model of action potential heterogeneity in adult rat left ventricular myocytes. *Biophysical journal* **81,** 3029-3051.

Petersen OH, Michalak M & Verkhratsky A. (2005). Calcium signalling: past, present and future. *Cell calcium* **38,** 161-169.

Potse M. (2012). Mathematical modeling and simulation of ventricular activation sequences: implications for cardiac resynchronization therapy. *Journal of cardiovascular translational research* **5,** 146-158.

Priebe L & Beuckelmann DJ. (1998). Simulation study of cellular electric properties in heart failure. *Circulation research* **82,** 1206-1223.

Priori SG. (2010). The fifteen years of discoveries that shaped molecular electrophysiology: time for appraisal. *Circulation research* **107,** 451-456.

Priori SG & Corr PB. (1990). Mechanisms underlying early and delayed afterdepolarizations induced by catecholamines. *The American journal of physiology* **258,** H1796-1805.

Puglisi JL & Bers DM. (2001). LabHEART: an interactive computer model of rabbit ventricular myocyte ion channels and Ca transport. *American journal of physiology Cell physiology* **281,** C2049-2060.

Rammler DH & Khorana HG. (1962). A new approach to the specific synthesis of the C3'-C5' inter-ribonucleotide linkage. *Biochemical and biophysical research communications* **7,** 147-150.

Rudy Y & Silva JR. (2006). Computational biology in the study of cardiac ion channels and cell electrophysiology. *Quarterly reviews of biophysics* **39,** 57-116.

Sanger F & Coulson AR. (1975). A rapid method for determining sequences in DNA by primed synthesis with DNA polymerase. *Journal of molecular biology* **94,** 441-448.

Shannon TR, Wang F, Puglisi J, Weber C & Bers DM. (2004). A mathematical treatment of integrated Ca dynamics within the ventricular myocyte. *Biophysical journal* **87,** 3351-3371.

Sigworth FJ & Neher E. (1980). Single Na+ channel currents observed in cultured rat muscle cells. *Nature* **287,** 447-449.

Stern MD. (1992). Theory of excitation-contraction coupling in cardiac muscle. *Biophysical journal* **63,** 497-517.

ten Eick RE, Whalley DW & Rasmussen HH. (1992). Connections: heart disease, cellular electrophysiology, and ion channels. *FASEB journal : official publication of the Federation of American*

Societies for Experimental Biology **6,** 2568-2580.

ten Tusscher KH, Noble D, Noble PJ & Panfilov AV. (2004). A model for human ventricular tissue. *American journal of physiology Heart and circulatory physiology* **286,** H1573-1589.

ten Tusscher KH & Panfilov AV. (2006). Alternans and spiral breakup in a human ventricular tissue model. *American journal of physiology Heart and circulatory physiology* **291,** H1088-1100.

Trayanova NA & Rice JJ. (2011). Cardiac electromechanical models: from cell to organ. *Frontiers in physiology* **2,** 43.

Verkhratsky A, Krishtal OA & Petersen OH. (2006). From Galvani to patch clamp: the development of electrophysiology. *Pflugers Archiv : European journal of physiology* **453,** 233-247.

Watson JD & Crick FH. (1953). Molecular structure of nucleic acids; a structure for deoxyribose nucleic acid. *Nature* **171,** 737-738.

Winslow RL, Rice J, Jafri S, Marban E & O'Rourke B. (1999). Mechanisms of altered excitation-contraction coupling in canine tachycardia-induced heart failure, II: model studies. *Circulation research* **84,** 571-586.

Zeng J & Rudy Y. (1995). Early afterdepolarizations in cardiac myocytes: mechanism and rate dependence. *Biophysical journal* **68,** 949-964.

CHAPTER 1

Trafficking Defects and Gating Abnormalities of a Novel SCN5A Mutation Question Gene-Specific Therapy in Long QT Syndrome Type 3

Short title: Paradoxical Effect of Mexiletine on LQT3.

The content of this chapter has been published in:

Ruan Y, Denegri M, Liu N, Bachetti T, Seregni M, **Morotti S**, Severi S, Napolitano C & Priori SG. (2010). Trafficking defects and gating abnormalities of a novel SCN5A mutation question gene-specific therapy in long QT syndrome type 3. *Circulation Research* **106,** 1374-1383.

Abstract

Na channel blockers are used as gene-specific treatments in long QT syndrome type 3 (LQT3), which is caused by mutations in the Na channel gene (SCN5A). The response to treatment is influenced by biophysical properties of mutations and we sought to investigate the unexpected deleterious effect of mexiletine in a mutation combining gain-of-function and trafficking abnormalities. A LQT3 child experienced paradoxical QT prolongation and worsening of arrhythmias after mexiletine treatment. The SCN5A mutation F1473S expressed in HEK293 cells presented a right-ward shift of steady-state inactivation, enlarged window current, and huge sustained Na current (I_{Na}). Unexpectedly, it also reduced I_{Na} peak by 80%. Immunostaining showed that mutant $Na_V1.5$ is retained in the cytoplasm. Incubation with 10 μmol/L mexiletine rescued the trafficking defect of F1473S, causing a significant increase in peak current, whereas sustained current was unchanged. Using a I_{Na} Markov model and a model of human ventricular action potential (AP), we showed that simulated exposure of F1473S to mexiletine paradoxically increased AP duration, mimicking QT prolongation seen in the index patient on mexiletine treatment. We provided evidence that Na channel blockers, which are largely used to shorten QT intervals in carriers of SCN5A mutations, may facilitate trafficking of mutant proteins, thus exacerbating QT prolongation. These data suggest that caution should be used when recommending this class of drugs to carriers of mutations with undefined electrophysiological properties, and *in vitro* and *in silico* analysis may help to choose the proper treatment.

INTRODUCTION

Long QT syndrome (LQT) is an inherited arrhythmogenic disease characterized by QT interval prolongation and susceptibility to ventricular tachyarrhythmias. LQT type 3 (LQT3) is a variant of LQT characterized by high lethality (Priori *et al.*, 2003), marked prolongation of repolarization, poor response to β-blockers (Priori *et al.*, 2004), and cardiac events occurring preferentially at rest. LQT3 is caused by mutations in the SCN5A gene that encode for the α subunit of the channel that conducts the inward Na current (I_{Na}) responsible for fast depolarization and critical for maintenance of intracardiac conduction (Clancy & Kass, 2005; George, 2005). Following the identification of the first SCN5A mutation published in 1995 (Wang *et al.*, 1995), more than 80 SCN5A mutations have been identified in LQT3 patients.

SCN5A mutations associated with LQT3 increase I_{Na} by augmenting either the sustained current (I_{sus}) or the window current, thus prolonging cardiac repolarization (Ruan *et al.*, 2009). Based on this evidence, the use of Na channel blockers to treat LQT3 patients and reduce QT interval has been proposed. Early *in vitro* studies (Priori *et al.*, 1996) demonstrated that mexiletine is effective in shortening action potential duration (APD) in cardiac myocytes exposed to anthopleurin, a compound that mimics LQT3 cellular phenotype. Furthermore early clinical studies on the use of mexiletine or flecainide were successful in shortening repolarization (Schwartz *et al.*, 1995; Windle *et al.*, 2001) and paved the way to the clinical use of Na channel blockers in LQT3 patients as a gene-specific therapy.

As the experience with the use of these drugs accumulated, the early enthusiasm was dimmed, and it became clear that flecainide might not be always appropriate for LQT3 patients. Indeed, the response of selected mutations could induce an electrocardiographic

pattern of coved type ST segment elevation in right precordial leads typical of Brugada syndrome (Priori *et al.*, 2000; Makita *et al.*, 2008). Shortly thereafter, it also became clear that Na channel blockers do not invariably shorten the QT interval, suggesting that SCN5A mutations act through other mechanisms, questioning the "gain-of-function" paradigm that all LQT3 mutations lead to a common channel dysfunction.

This view is supported by the fact that "some" SCN5A mutations cause "overlapping syndromes" in which QT prolongation is associated with "loss-of-function" clinical phenotypes (Brugada syndrome or conduction defects) (Bezzina *et al.*, 1999; Grant *et al.*, 2002; Antzelevitch *et al.*, 2005). It has been recently demonstrated that biophysical diversity of SCN5A mutations is a determinant of response to mexiletine in the clinical setting (Ruan *et al.*, 2007).

Here, we bring the characterization of the diversity of SCN5A mutations to the next level by showing that the interplay between protein trafficking and biophysical abnormalities may detrimentally affect the response to Na channel blockers and represent a hazard rather than a cure.

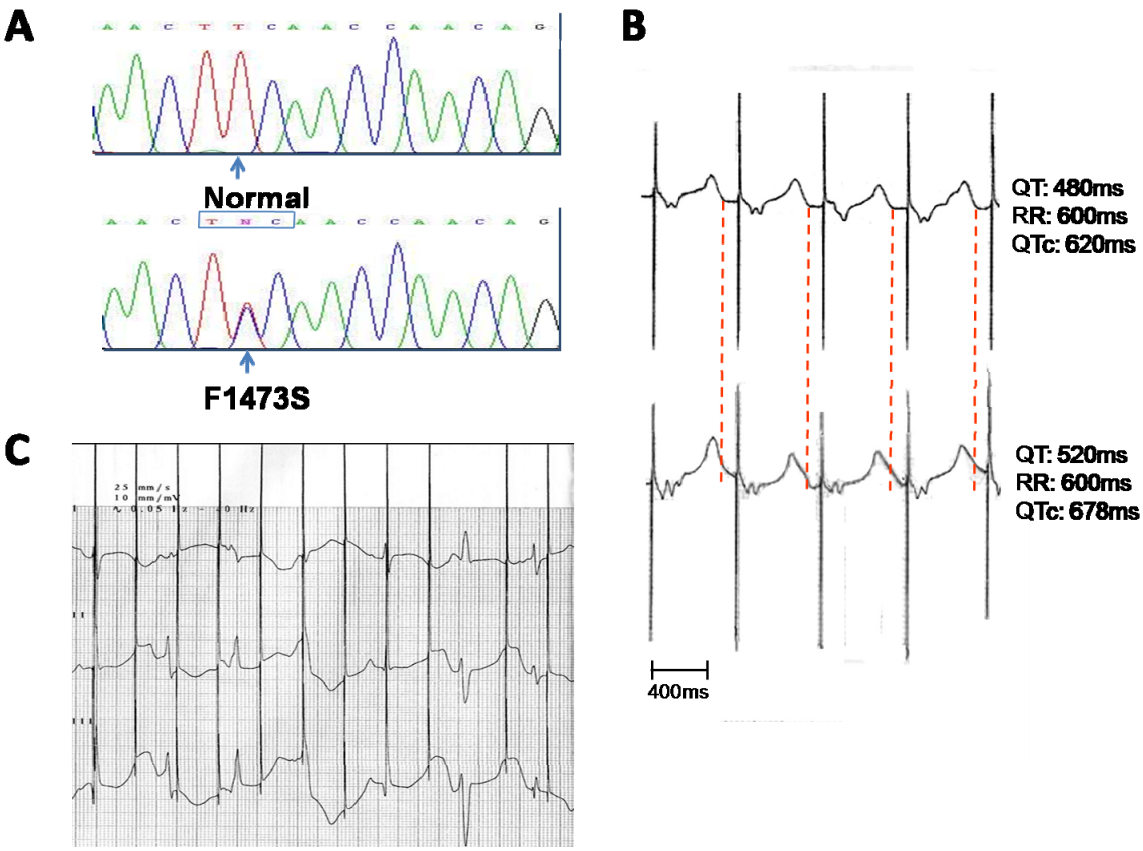

Figure 1. Mexiletine failed to shorten QTc and to prevent malignant ventricular arrhythmia. Panel A, DNA sequence encoding a portion of DIII~DIV is shown for a normal control and for the index patient. The affected codon is enclosed by a rectangle indicating the heterozygous F1473S missense mutation. B, ECG recorded at day 1 (upper trace) and day 10 (lower trace) of mexiletine treatment. Further QTc prolongation is evident and T wave is almost fused with the subsequent stimulation spike. C, ECG tracing recorded at day 10 on mexiletine showing failures of pacemaker capture with extremely prolonged cardiac repolarization.

METHODS

In vitro characterization has been performed by our collaborators from Priori group, while we investigated *in silico* the consequences of mutation and mexiletine administration on the human ventricular action potential (AP).

In vitro

Molecular Screening

Genetic analysis was performed by screening of the open reading frame of the SCN5A, KCNH2, KCNQ1, KCNE1, and KCNE2 genes as previously reported (Napolitano *et al.*, 2005).

Site-directed Mutagenesis and Transfection in HEK293 Cells

The SCN5A mutations were engineered into wild-type (WT) cDNA cloned in pcDNA3.1 (Invitrogen, Carlsbad, CA, USA) and confirmed by sequence analysis of the entire cDNA of

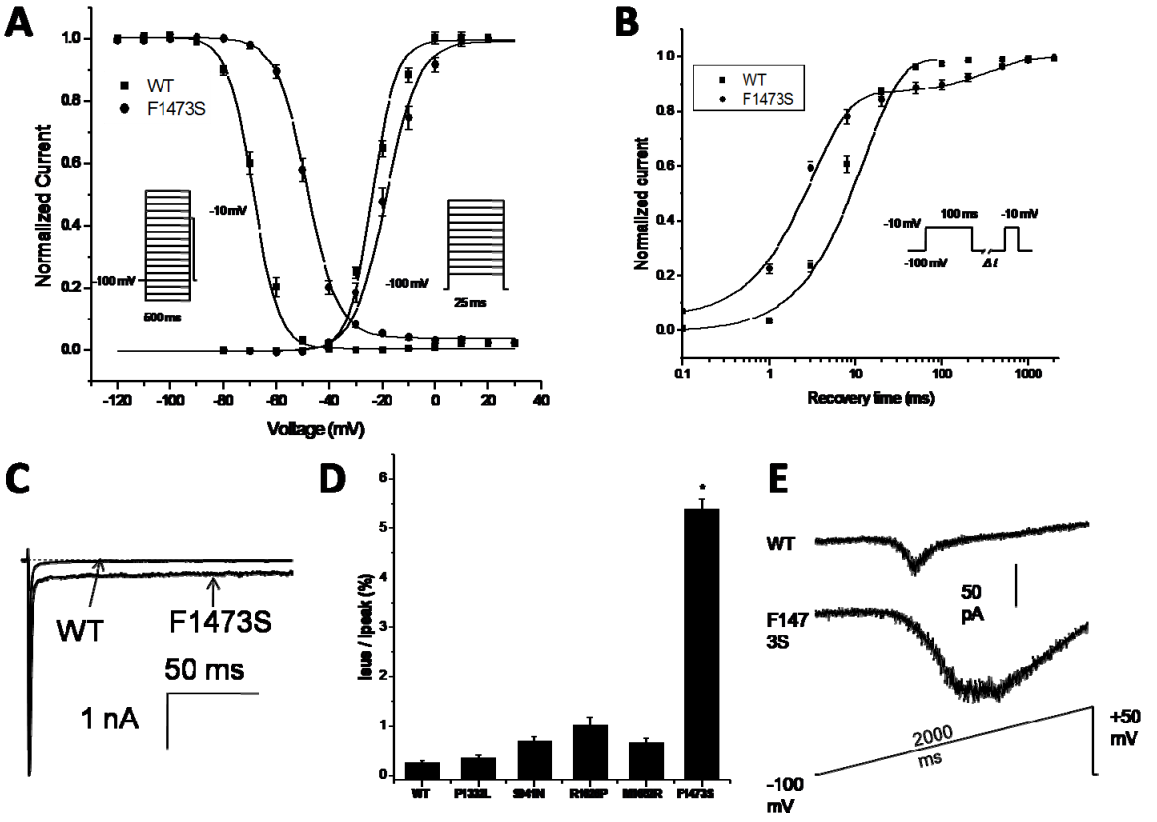

Figure 2. Gating properties of F1473S. Panel A, The voltage dependence of SSI and SSA of F1473S, measured with standard pulse protocols shown in inset. B, Recovery from inactivation was assessed by the double-pulse protocol shown in inset and fitted using a biexponential function. C, Representative current traces evoked by 150 ms pulses to -10mV for cells expressing WT or F1473S channels. Currents have been normalized to facilitate comparison of WT and F1473S current traces. Besides reduced peak current, F1473S impair channel inactivation and induce a huge I_{sus}. D, The amplitude of I_{sus} in F1473S expressed in percentage of peak current is more than 20-fold larger than in WT; and it is also significantly larger than in P1332L, S941N, R1626P and M1652R, the LQT3-causing SCN5A mutations previously studied. N=7 to 21 cells for each group. * $P < 0.001$ compared with WT, P1332L, S941N, R1626P and M1652R. E, WT and F1473S currents in response to a ramp test.

SCN5A. HEK293 cells were transfected with equal amount of Na channel α and β_1 subunit by lipofectamine as previously described (Ruan *et al.*, 2007).

Electrophysiology

Membrane currents were measured using whole-cell patch-clamp procedures, with Axopatch 200B amplifiers (Axon Instruments, Foster City, CA, USA). Internal pipette solution contained (mmol/L) aspartic acid 50, CsCl 60, Na_2-ATP 5, EGTA 11, HEPES 10, $CaCl_2$ 1, and $MgCl_2$ 1, with pH 7.4 adjusted with CsOH. External solutions consisted of (mmol/L) NaCl 130, $CaCl_2$ 2, CsCl 5, $MgCl_2$ 1.2, HEPES 10, and glucose 5, with pH 7.4 adjusted with CsOH. In experiments designed to measure the voltage dependence of activation, external Na was reduced to 30 mmol/L with N-methyl-glucamine used as a Na substitute. Recordings were made at room temperature. Holding potentials were -100 mV. I_{sus} was measured 150 ms

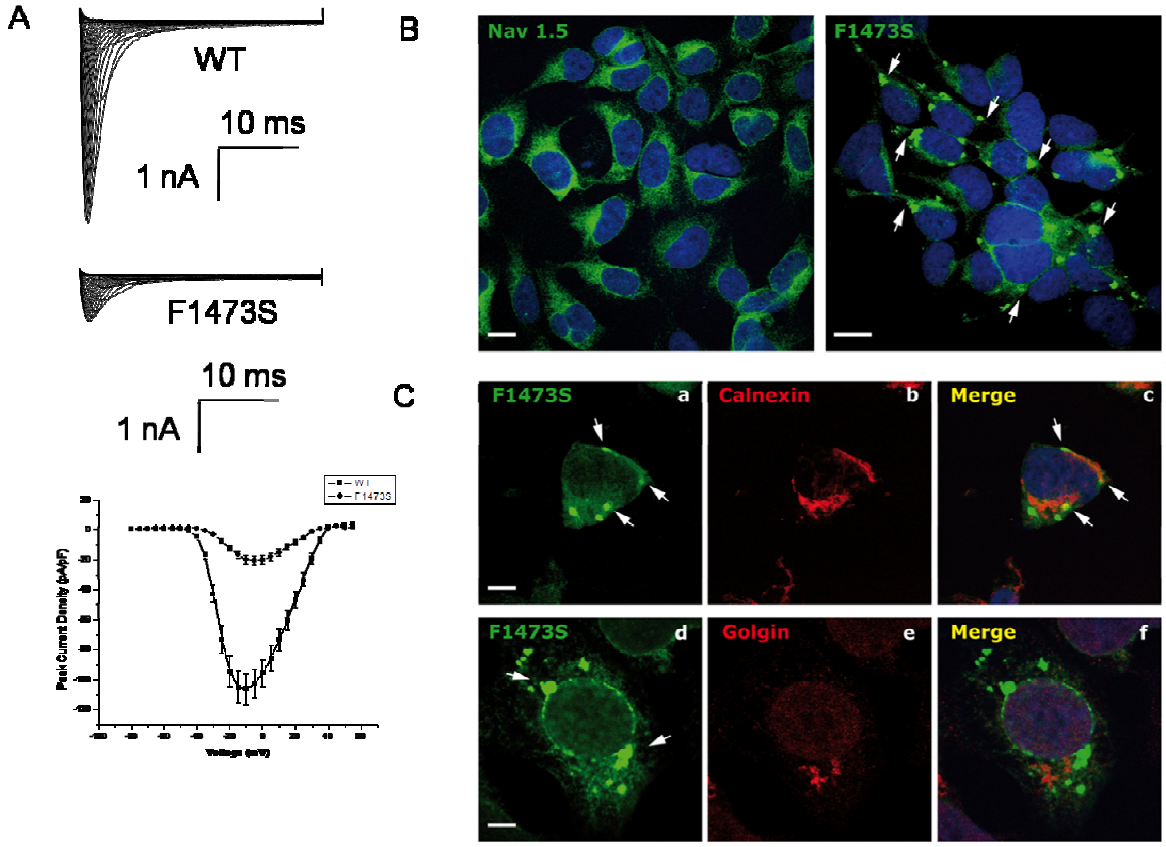

Figure 3. F1473S induced a large I_{sus} and reduced peak current in SCN5A channel. Panel A, Representative whole-cell current traces in HEK293 cell expressing WT (upper) and F1473S (middle) channels. Lower: Current-voltage (I-V) relationship of peak inward current. B, Cells expressing either WT (left) or F1473S (right) SCN5A were immunostained with anti-SCN5A primary antibody (Alomone ASC-005, green). The nuclei were highlighted by the DAPI staining (blue) (scale-bar 10 nm). WT channels were distributed mainly in the cytoplasm and on the plasma membrane; F1473S mutant channels show many condensed spots within the cytoplasm, suggesting a trafficking impairment (white arrows). C, Cytoplasmic distribution of F1473S mutant channel in HEK-SCN5A stable cell lines. Fixed cells were co-stained with the anti-SCN5A polyclonal antibody (green, a and d) and either with anti-Calnexin mAb for the ER (red, b) or anti-Golgin 97 mAb for the Golgi Apparatus (red, e). Protein localization was revealed by indirect immunofluorescence using DyLight 488-conjugated anti-rabbit IgG donkey antibodies and DyLight 594-conjugated anti mouse IgG donkey antibodies. The nuclei were stained with DAPI (blue) (scale-bar 10 nm).F1473S showed many condensed spots (white arrows) proximal to and partially co-localizing with the ER but not with the Golgi apparatus revealing that F1473S mutant channels are either kept in the ER or in the cytoplasm.

after depolarization to -10 mV and determined by subtracting background currents measured in the presence of tetrodotoxin (30 μmol/L, Sigma) from tetrodotoxin-free records. This subtraction procedure was also used for voltage ramp experiments. Steady-state inactivation (SSI) was determined after application of conditioning pulses (500 ms) applied to a series of voltages with an interpulse interval of 5 seconds for control and 30 seconds for mexiletine. Steady-state activation (SSA) was estimated by measuring peak current during a variable test potential. Current at each membrane potential was divided by the electrochemical driving force for Na ions and normalized to the maximum Na conductance. Data for the voltage dependence of activation and inactivation were fitted with the Boltzmann equation. Recovery from inactivation was measured in paired pulse experiments. Details of pulse protocol are given schematically in the figures. Data for the time course of recovery were fitted with biexponential function. Tonic block was measured at 0.033 Hz after steady-state was

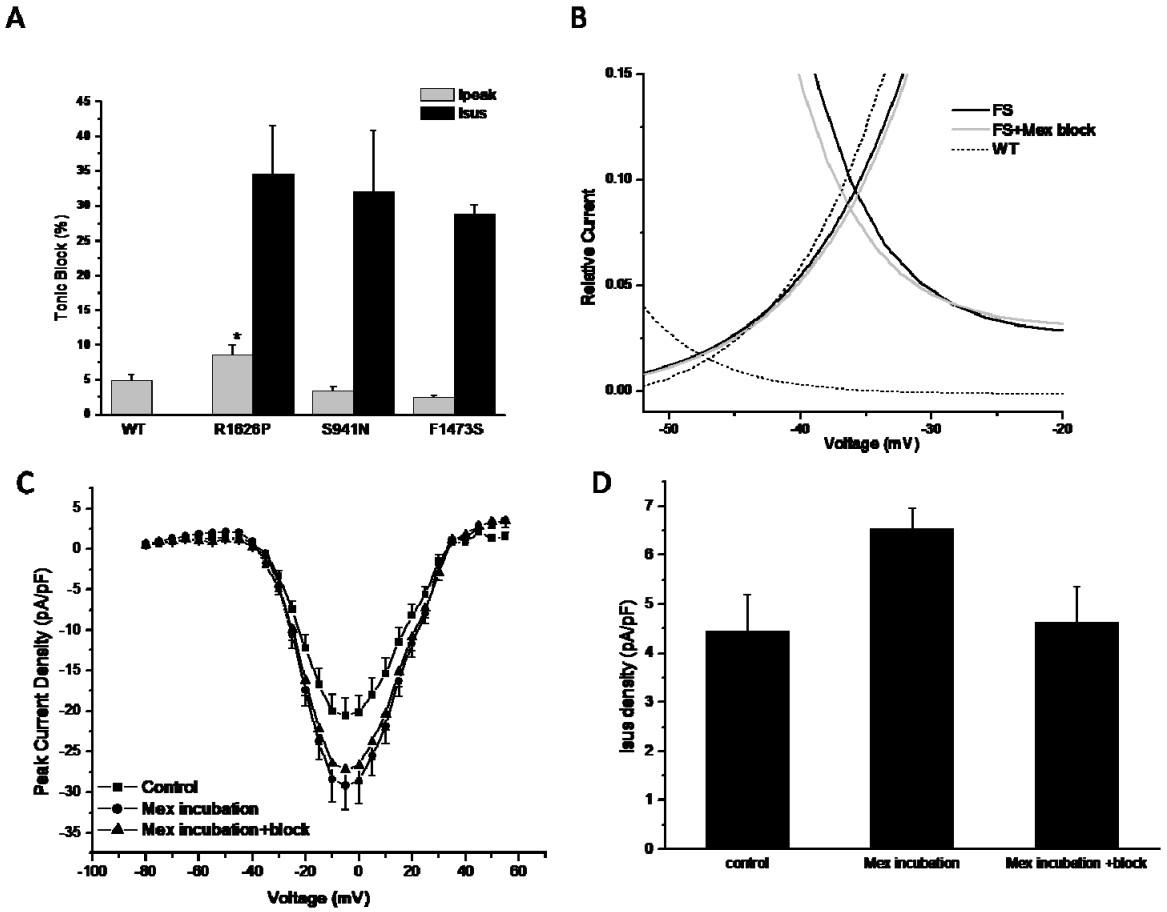

Figure 4. Rescue effect and block effect of mexiletine. Panel A, Tonic block for WT, R1626P (mexiletine sensitive), S941N (mexiletine insensitive), and F1473S, determined by the first test pulse after application of mexiletine. B, F1473S depolarizing shift SSI produced an enlarged window current (black solid line) compared with WT (block dash line); effect of 10 μmol/L mexiletine on window current was marked as grey solid line. C, Peak current density of three conditions: F1473S control (control, 20.54±2.22 pA/pF at -5mV, n=33), F1473S incubated with 10 μmol/L mexiletine for 48 hours with current recording without the drug (w/out tonic block, 29.17±2.87 pA/pF at -5mV, n=44, P<0.05 *vs*. control), and F1473S incubated with 10 μmol/L mexiletine for 48 hours and current recording in the presence of mexiletine (mex w/ tonic block, 27.17±2.3 pA/pF at -5mV, n=36, P<0.05 *vs*. control). D, I_{sus} density of three conditions: F1473S control, F1473S incubated with 10 μmol/L mexiletine for 48 hours with current recording without (and with) the drug.

achieved in the presence of mexiletine. In drug rescue experiments, freshly prepared 10 µmol/L mexiletine was added to the culture media.

Immunofluorescence

For immunofluorescence (IF) experiments HEK293 cells were seeded on 0.1% gelatincoated coverslips and allowed to attach for 24 h, where indicated 10 µmol/L mexiletine was added for 48 hours. Following PBS washed cells were fixed with 4% PFA for 10 min and permeabilised with 0.2% Triton for 10 min. Blocking of unspecific sites were achieved by incubation with 10% BSA for 1 hour at room temperature. Primary antibodies used were: polyclonal $Na_V1.5$ (Alomone, ASC-005, 1:100), monoclonal Calnexin (Alexis, clone AF18, 1:200), monoclonal Golgin 97 (Molecular Probes, CDF4, 1:50). Secondary antibodies used were: DyLight 488-conjugated donkey anti-rabbit IgG and Dy-Light-conjugated 594-conjugated donkey anti-mouse IgG (Jackson Laboratories, 1:100). The coverslips were then mounted using a DAPI-containing mounting medium (Vectashield, Vector Laboratories, Burlingame, CA, USA). Confocal microscopy was performed with a Leica TCS-SP2 digital scanning confocal microscope equipped with a HCX PL APO 40x/numerical aperture=1.25 oil immersion objective. The 488-nm Argon laser line has been used for excitation of DyLight 488-conjugated donkey anti-rabbit IgG (detected at 500-530 nm) and the 594 nm He/Ne laser

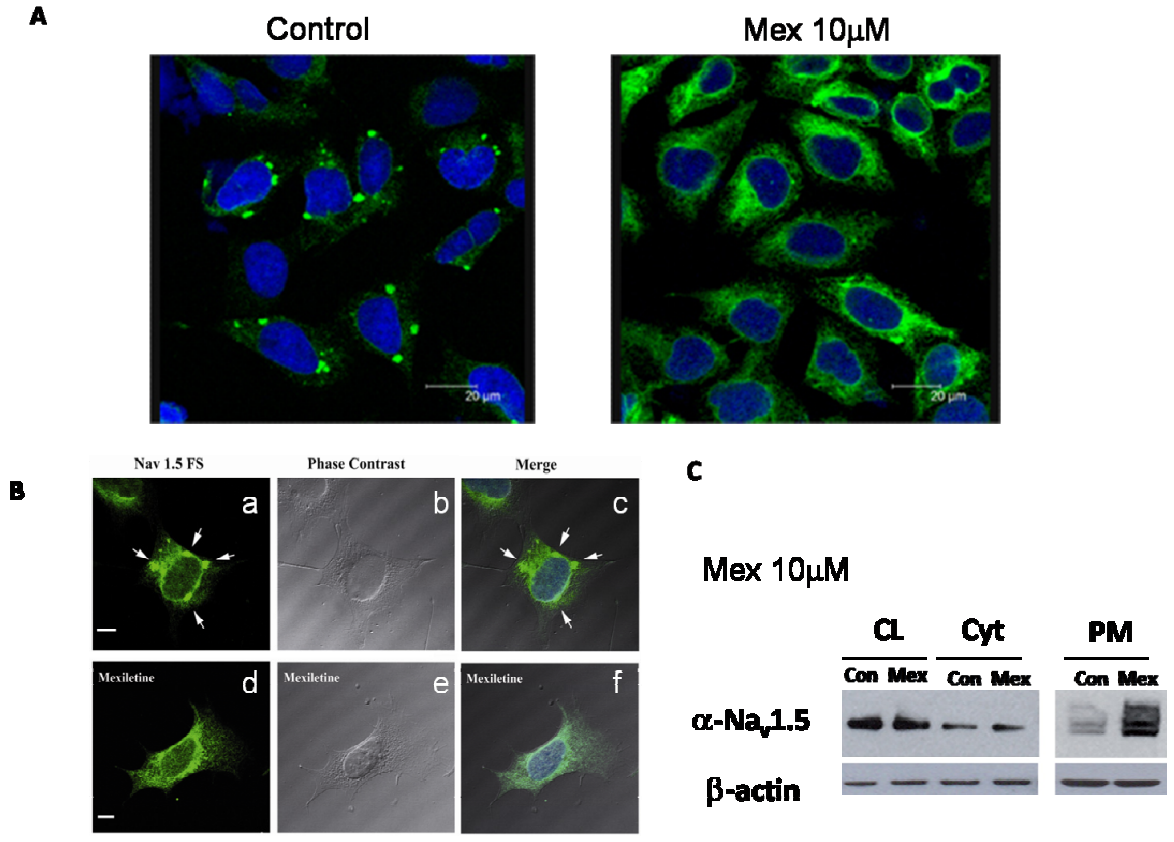

Figure 5. Rescued membrane expression of F1473S SCN5A channel with 10 µmol/L mexiletine. Panel A, mexiletine incubation increased the cytoplasmic distribution of F1473S and released the intracellular condensed spots of F1473S (scale-bar 20 nm). B, Confocal images of F1473S distribution with phase contrast in control condition (upper) and with 10 µmol/L mexiletine incubation (lower) (scale-bar 10 nm). C, Plasma membrane fraction of F1473S SCN5A was increased by mexiletine incubation. PM indicates plasma membrane, Cyt, cytosol, CL, total cell lysate; Con, control, no mexiletine incubation, Mex, 10 µmol/L mexiletine incubation for 48 hours. β-Actin was used as the normalizing control.

line for excitation of Dy-Light-conjugated 594-conjugated donkey anti-mouse IgG (detected at 580-630 nm). The pinhole diameter was kept at Airy 1. Images were exported to Adobe Photoshop (Adobe Systems, Mountain View, CA, USA).

Immunoblotting for Quantification of Plasma Membrane Protein Expression

First our collaborators confirmed that the I_{Na} observed in stable cell lines expressing F1473S-$Na_V1.5$ was identical to the current observed in cells with transient expression of the mutant α and β1 subunit and they were able to show that the same large I_{sus}, reduced peak current, trafficking defect and gating properties were also present in the transiently transfected cells expressing F1473S-$Na_V1.5$ (data not shown). HEK293 cells which stably expressed F1473S SCN5A were lysed and total proteins extracted; plasma membrane and cytosolic fractions were isolated using a plasma membrane protein extraction kit according to manufacturer's instructions (Biovision). Total proteins (15 micrograms/sample, quantified by the BCA assay) were resolved by SDS-gel electrophoresis on Novex 4-12% BisTris gradient gels using MES-SDS buffer (Invitrogen), and blotted on nitrocellulose membranes using a submarine system (Invitrogen). A monoclonal anti-human $Na_V1.5$ antibody (1:500, Alomone, Asc-005) was used to probe for the Na channel while a polyclonal anti β-Actin antibody (1:5000, Affinity Bioreagents) was used to detect a reference protein. Secondary antibodies were conjugated with HRP (1:3000, Promega). Mouse heart was used as positive control. Specific signals were developed using the Supersignal West Pico Chemiluminescent substrate (Pierce) and detected using X-ray films (Kodak).

Statistics

Pclamp9.2 (Axon Instruments, Foster City, CA, USA) and Excel (Microsoft, Seattle, WA, USA) were used for data acquisition and analysis. Data are presented as mean values ± S.E. Statistical comparisons were made using an unpaired 2-tailed t-test or ANOVA with the Tukey post hoc test to evaluate the significance of differences between means. $P<0.05$ was considered statistically significant.

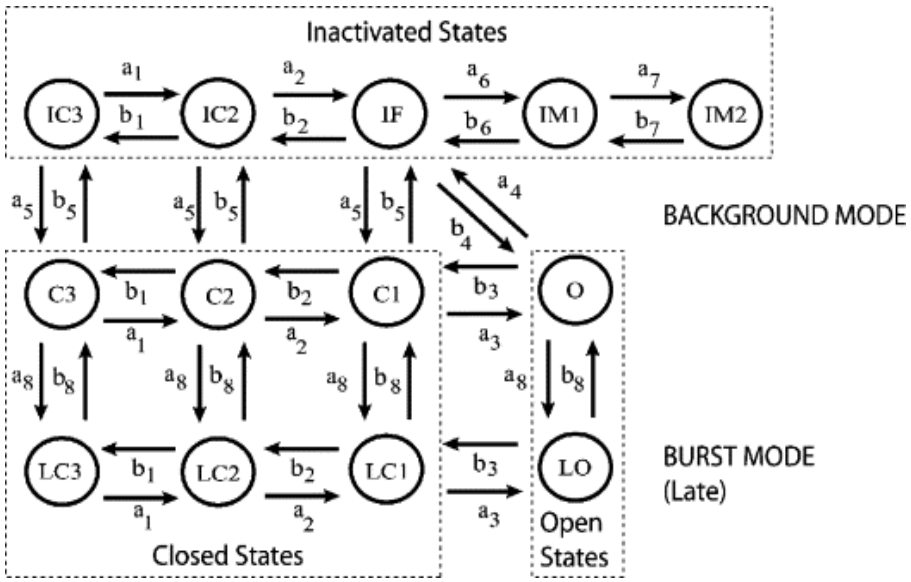

Figure 6. Markov model of the cardiac Na channel. The channel model contains background (upper nine states) and burst (lower four states) gating modes. The burst mode reflects a population of channels that transiently fail to inactivate. From (Grandi *et al.*, 2007).

In silico

The Na channel Markov model was based on the structure originally proposed by Clancy and colleagues (Clancy & Rudy, 1999; Clancy *et al.*, 2002), depicted in Fig. 6. The whole-cell I_{Na} is given by:

$$I_{Na} = G_{Na} P_O (E_m - E_{Na}),$$

where the variable P_O represents the sum of the probabilities to be in the open states (O and LO), E_m is the membrane potential, E_{Na} is the Na Nerst potential and G_{Na} is the maximum conductance. The expressions of the transition rates are reported in Table 1. The transition rate parameters were identified by a manual fitting procedure to simulate the experimental data of whole-cell cardiac I_{Na} from HEK cells expressing WT or F1473S SCN5A. The following voltage-clamp protocols were simulated for parameter identification: SSA and SSI, recovery from inactivation, positive voltage ramp and long-depolarization voltage step to assess I_{sus}. The model results for each protocol were compared with experimental data. The parameter values proposed by in a previous study (Grandi *et al.*, 2007) were chosen where possible as initial guesses in the identification procedure of the transition rate parameters that allowed the best fitting of our WT data. We modified a_2 and a_4 to reproduce the experimental data on SSA; a_5 was tuned to correctly simulate the channel availability curve; a_6, b_6 and a_7, b_7 were adjusted to represent the observed characteristics of recovery from inactivation, a_5, b_6, b_7 were modified to reproduce the response to voltage ramp in the mutant channels and the ratio a_8/b_8 was tuned to reproduce the experimental data accounting for I_{sus}. The identified WT set was subsequently used as initial guess to identify the F1473S channel parameters, and two parameters of the F1473S set were tuned to reproduce the effect of mexiletine treatment: P_{2a5} was modified to introduce the SSI shift and P_{1a8} to reduce I_{sus}. Table 2 reports the three sets of model parameters.

We integrated the I_{Na} model into a model of AP in human epicardial ventricular myocyte (ten Tusscher & Panfilov, 2006) as modified by Severi *et al.* to correctly reproduce

Table 1. Na channel model transition rate expressions.

Transition rate expressions
$a_1 = P_{1a1}/(1+\exp((-E_m+P_{2a1})/P_{3a1}))$
$a_2 = P_{1a1}/(1+\exp((-E_m+P_{2a2})/P_{3a2}))$
$a_3 = P_{1a3}/(1+\exp((-E_m+P_{2a3})/P_{3a1}))$
$b_1 = P_{1b1}\exp((-E_m+P_{2a1})/P_{2b1})$
$b_2 = P_{1b2}\exp((-E_m+P_{2b2})/P_{2b1})$
$b_3 = P_{1b3}\exp((-E_m+P_{2b3})/P_{2b1})$
$a_4 = P_{1a4}\exp((E_m-P_{2a1})/P_{2a4})$
$a_5 = (P_{1a5}/(1+\exp((E_m+P_{2a5})/P_{3a5})))(P_{7a5}+P_{4a5}/(1+\exp((-E_m+P_{5a5})/P_{6a5})))$
$a_6 = a_4/P_{1a6}$
$b_4 = (a_3\ a_4\ a_5)/(b_3\ b_5)$
$b_5 = P_{1b5}+P_{2b5}\ (E_m-P_{2a1})$
$b_6 = P_{1b6}\exp((-E_m+P_{2a1})/P_{2b6})+P_{5b6}/(1+\exp((-E_m+P_{4b6})/P_{3b6}))$
$a_7 = P_{1a7}\exp((E_m-P_{2a1})/P_{2a7})$
$b_7 = P_{1b7}\exp((-E_m+P_{2a1})/P_{2b7})+P_{5b7}/(1+\exp((-E_m+P_{4b7})/P_{3b7}))$
$a_8 = P_{1a8}$
$b_8 = P_{1b8}$

the experimental APD inverse dependence on extracellular [Ca] (Severi *et al.*, 2009). The kinetic rates were normalized to 37°C using a Q_{10} of 2.1 (Maltsev & Undrovinas, 2006). Extracellular [Ca] was set to the physiological value of 1.15 mmol/L. Since mutant patients reveal stronger I_{sus} and thereby higher intracellular [Na], the initial value of this concentration was set at 15 mmol/L in order to reach quickly the steady-state condition. Pacing was simulated by a current pulse train (pulse 1 ms duration, 52 pA/pF amplitude) at different frequencies (from 30 to 120 bpm, *i.e.* from 0.5 to 2 Hz). The stimulation was maintained at

Table 2. Na channel model parameters for WT and F1473S.

Parameters	WT	F1473S	F1473S + mexi
P_{1a1}	62.5	25	
P_{2a1}		$5.4e^{-3}$	
P_{3a1}	15	30	
P_{2a2}	$-5.4e^{-3}$	-6.0054	
P_{3a2}	17	7	
P_{1a3}	500	27	
P_{2a3}	29.995	$-5.4e^{-3}$	
P_{1b1}	0.47925	0.1917	
P_{2b1}		20.3	
P_{1b2}	0.5	0.2	
P_{2b2}		4.9946	
P_{1b3}	0.55	0.22	
P_{2b3}		9.9946	
P_{1a4}	1.175	5.1	
P_{2a4}	90	45	
P_{1a5}	0.021	0.265	
P_{2a5}	71.995	56.995	57.995
P_{3a5}		6	
P_{4a5}	0	400	
P_{5a5}		29.995	
P_{6a5}		7	
P_{7a5}		1	
P_{1b5}	0.126	0.42	
P_{2b5}		$2e^{-6}$	
P_{1a6}	50	17	
P_{1b6}		$3e^{-4}$	
P_{2b6}	11.394	13	
P_{5b6}	0	0.25	
P_{3b6}		5	
P_{4b6}		-18.005	
P_{1a7}	$3.543e^{-3}$	$3.19e^{-3}$	
P_{2a7}		23.27	
P_{1b7}	8	$5.8363\ e^{-5}$	
P_{2b7}	35.99	27	
P_{3b7}		3	
P_{4b7}		-30.005	
P_{5b7}	0	$4.5e^{-3}$	
P_{1a8}	$1.4e^{-6}$	$4.9e^{-6}$	$1.5e^{-6}$
P_{1b8}		$9.5e^{-4}$	

least for 200 s. To analyze the effects of mutations on cardiac AP in the heterozygous condition of F1473S patients, we replicated conditions with different percentage of mutant and WT Na channels.

Matlab and Simulink (Mathworks, Natick, MA, USA) were used for all the numerical computations. A variable order solver based on the numerical differentiation formulas (NDFs) was used to numerically solve the model equations (ode15s).

RESULTS

Clinical history of the carrier of F1473S mutation in the SCN5A gene

The mutation here characterized was identified in a patient born in 2003; no ECG was recorded at birth, and the baby was discharged as a healthy infant. At 12 months of age, he experienced 5 syncopal spells within a few days, was hospitalized and long QT syndrome was diagnosed. Propranolol (4 mg/kg per day) was initiated, and a blood sample was sent to the Priori group in Maugeri Foundation for genetic screening. They sequenced the opening reading frame of KCNQ1, KCNH2, SCN5A, KCNE1, and KCNE2 and identified a heterozygous single-nucleotide transition (4418T>C) in the SCN5A gene, leading to a single amino acid replacement at position 1473 (F1473S, Fig. 1A). This mutation was not present in either the parents of the index case or in 300 control DNA samples.

The patient remained asymptomatic for 2 years on β-blockers; however, in 2006, syncope recurred and torsade de pointes was documented; a ventricular-inhibited pacemaker was implanted, and the dose of β-blockers was increased. One year later, the patient experienced another syncopal episode, accompanied by several runs of torsade de pointes. Oral mexiletine was started in an attempt to shorten QT interval and to control arrhythmias; sinus rhythm was regained and QT duration appeared stable at day 1 of administration (Fig. 1B, upper trace); unfortunately, the effect of mexiletine (60 mg tid) decayed as the treatment continued. After 10 days, corrected QT interval (QTc) persistently exceeded 650 ms (Fig. 1B, lower trace); furthermore, progressive worsening of intraventricular conduction with QRS widening, and occasional pacemaker capture failures (Fig. 1C) were observed. At day 11, the patient developed incessant, intractable tachyarrhythmias and died. The clinicians who treated the patient were confounded by the worsening clinical status during mexiletine treatment. The inspection of the available ECG showed QTc shortening just at the beginning of therapy followed by prolongation (Fig. 1B). The Priori group and us attempted to understand this uncommon and paradoxical response to mexiletine by functional characterization of the mutant.

Functional *in vitro* characterization of F1473S mutation

As shown in Fig. 2A, F1473S depolarized the SSI curve by 18.9 mV and SSA curve by 4.4 mV. The SSI pattern of mutant channels was consistent with previous observations (Ruan *et al.*, 2007) showing that mexiletine-insensitive mutations are those causing a depolarizing shift of SSI and it also produced a greater overlap of activation and inactivation relations. As a consequence, the window current was markedly enhanced. Recovery from inactivation is shown in Fig. 2B.

Besides enlarged window current, F1473S showed a striking increase of I_{sus}. At -10 mV, F1473S channels continued to show 4.46±0.74 pA/pF (5.39±0.2% of the peak current) at 150 ms as compared to 0.64±0.22 pA/pF (0.25±0.05%) in WT (P<0.0001). Overall, F1473S showed a much higher I_{sus} than other mutations previously characterized (Ruan *et al.*, 2007) (Fig. 2C).

Our collaborators further characterized the gain-of-function behavior by ramp voltage protocol (from -100 mV to +50 mV). F1473S conducted larger peak currents than WT (F1473S -6.38±0.71 pA/pF, n=9 *vs*. WT -2.28±0.14 pA/pF, n=8; P<0.0001), and the voltage of the peak was shifted by about +20 mV (F1473S -17.1±3.5 mV, n=9 *vs*. WT -37.8±3.1 mV, n=8; P<0.0001). WT channels conduct current over a narrow range of voltages near -37 mV, whereas F1473S mutant channels conduct current over a broad range of voltages and increase the inward I_{Na} (Fig. 2D). The Priori group concluded that the remarkable increase of both the window current and the I_{sus} account for QT prolongation and the malignant clinical phenotype.

On the other hand, F1473S peak current density was unexpectedly reduced to 20% of

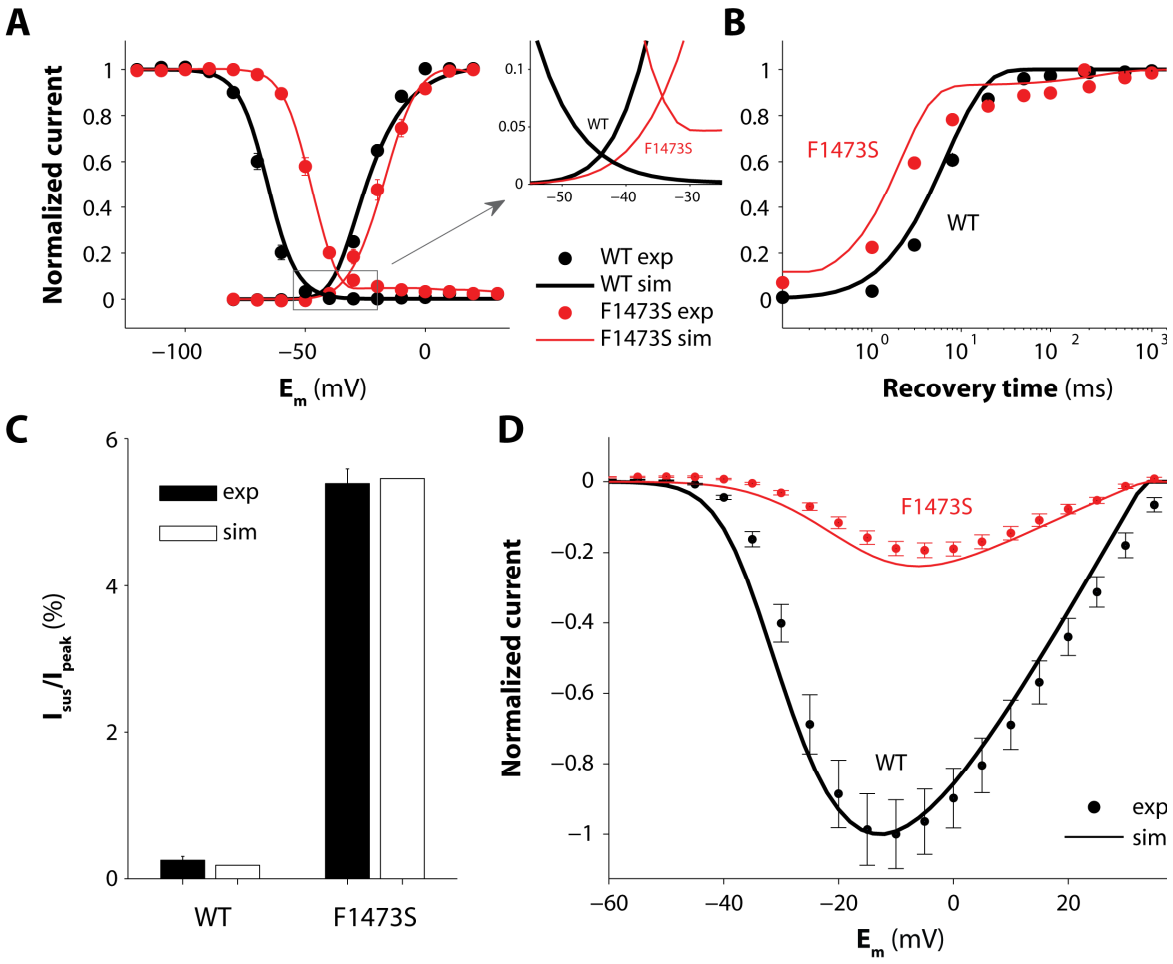

Figure 7. Experimentally determined and simulated effects of F1473S mutation on Na channel properties. Panel A, SSI and SSA, the inset highlights *in silico* results in window current region. B, recovery from inactivation. Dots represent data from *in vitro* experiments, solid lines represent simulated results. C, experimental (black) and simulated (white) ratio between sustained and peak current for WT and F1473S channels. D, experimental (symbols) and simulated (solid lines) I-V relations for WT and F1473S channels.

WT (Fig. 3A), suggesting a trafficking abnormality. This hypothesis was confirmed by confocal microscopy experiments that showed an abnormal protein distribution characterized by clusters/aggregates retained in the cytoplasm (Fig. 3B, F1473S). Our collaborators attempted to colocalize such clusters to determine whether the mutant polypeptides were retained either in the endoplasmic reticulum (ER) (anti-calnexin antibody) or in the Golgi apparatus (anti-Golgin antibody). The F1473S-$Na_V1.5$ clusters did not colocalize with Golgi (Fig. 3C, f) and only mildly colocalized with ER (Fig. 3C, c), suggesting that most of the abnormal protein is likely to be either free in the cytosol or segregated in yet unidentified subcellular domain(s).

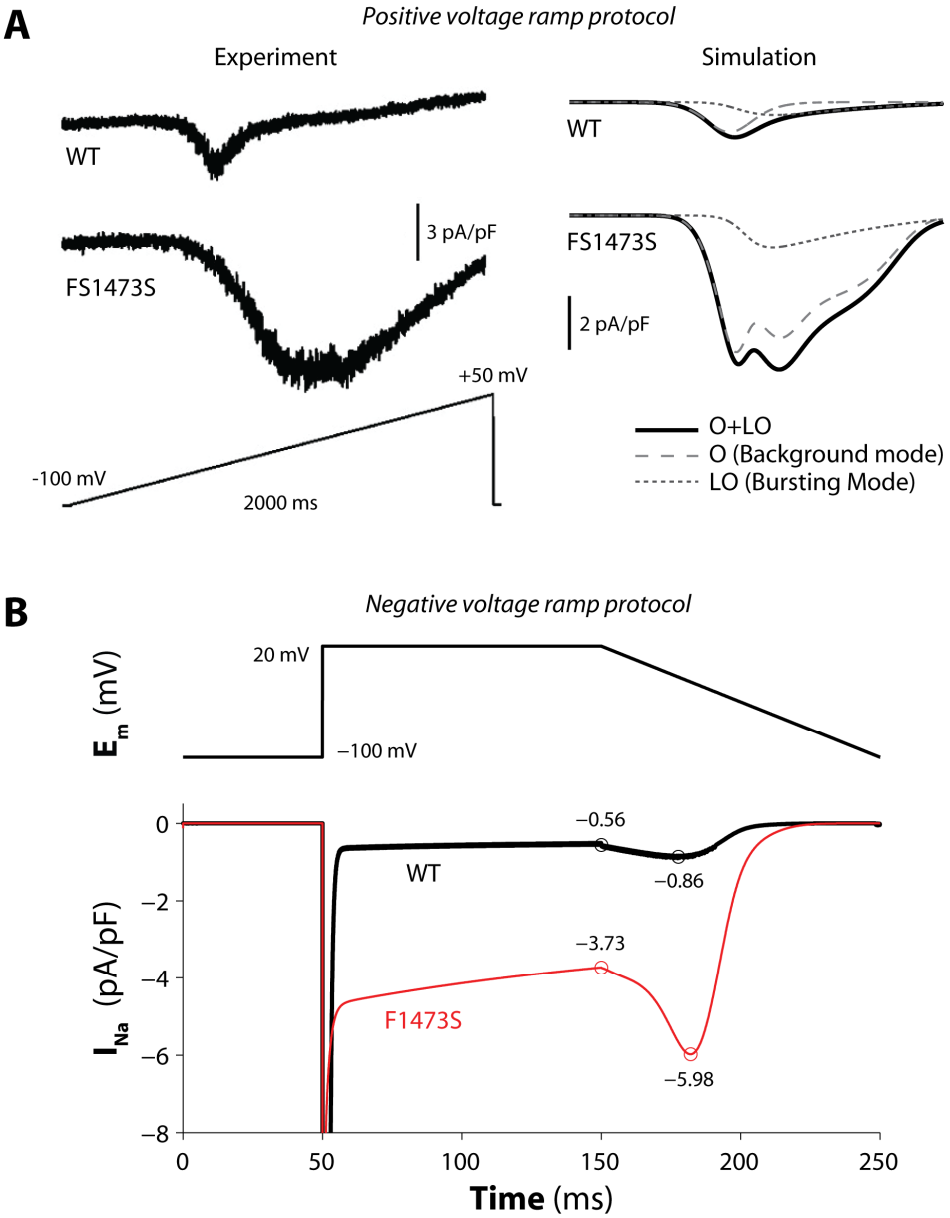

Figure 8. Simulated WT and F1473S current response to positive and negative voltage ramp protocols. Panel A, experimental (from Fig. 2E) and simulated WT and F1473S current obtained in response to a positive ramp test. B, simulated WT and F1473S current obtained in response to a negative ramp protocol.

Response of F1473S-$Na_V1.5$ channel to exposure to Na channel blockers

Our collaborators compared the tonic block of mexiletine in F1473S-$Na_V1.5$ with that observed in WT and in mexiletine-sensitive (R1626P) and mexiletine-insensitive mutations (S941N) previously characterized (Ruan *et al.*, 2007). Fig. 4A shows that tonic block of peak current with 10 µmol/L mexiletine was significantly higher in R1626P compared with WT, S941N, and F1473S; no significant difference was found between F1473S and WT or the insensitive mutation, S941N. Consistent with previous studies showing that Na channel blockers inhibit preferentially I_{sus} *vs*. peak current (Wang *et al.*, 1997), tonic block of I_{sus} was proportionally stronger than tonic block of peak current with 10 µmol/L mexiletine (Fig. 4A). The tonic block of I_{sus} was similar among the 3 mutants.

An additional well-known mechanism underlying the LQT3 phenotype is the reopening of Na channels over voltage ranges for which SSI and SSA overlap (*i.e.* the window current). The Priori group tested the effect of 10 µmol/L mexiletine on SSI and SSA in the F1473S mutation. SSI shifted toward the negative potential by -1.15 mV, SSA was slightly shifted toward the positive potential by 0.32 mV leaving the overlapping region substantially unchanged (Fig. 4B).

Mexiletine exposure and trafficking

Previous studies suggested mexiletine rescued impaired trafficking observed in selected loss-of-function SCN5A mutants associated with Brugada syndrome (Valdivia *et al.*, 2002; Tan *et al.*, 2006; Pfahnl *et al.*, 2007). Our collaborators therefore assessed whether the F1473S-Nav1.5 trafficking defect could be rescued by the drug. F1473S channels incubated with mexiletine (10 µmol/L for 48 hours) did not change their gating properties (data not shown) but showed significantly increased current density. Fig. 4C shows that I_{Na} peak at -5 mV increased by 42% after incubation but recorded in the absence of mexiletine, indicating that mexiletine does restore trafficking of F1473S. Interestingly, however, peak current density recorded in the presence of mexiletine (after incubation) was still increased by 32%, indicating that rescue effect overwhelmed the blocking effect.

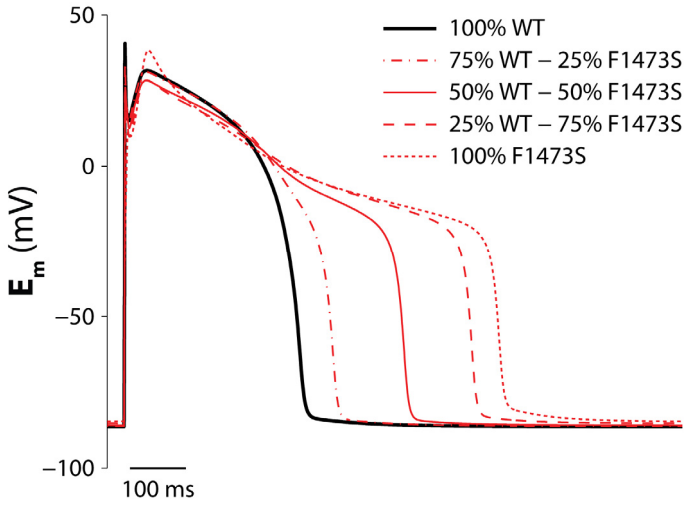

Figure 9. Simulated impact of increasing F1473S mutation expression on AP. APD increases when increasing the expression of mutant channel.

Similar approach was used to quantify I_{sus}: 1) incubation with 10 µmol/L mexiletine (48 hours) and recordings in the absence of mexiletine showed 46% increased I_{sus} density. The I_{sus} to peak current ratio remained the same as in untreated cells, implying that I_{sus} is increased by mexiletine incubation as a direct consequence of rescuing of the trafficking. 2) I_{sus} density recorded after incubation and in presence of 10 µmol/L mexiletine remained same as control (untreated cells) indicating that mexiletine treatment did not decrease I_{sus} density because the rescue effect balanced out the block effect (Fig. 4D).

Immunostaining with anti-h$Na_V1.5$ antibody confirmed that mexiletine incubation alleviates the trafficking impairment caused by F1473S. As shown in Fig. 5A and B, after mexiletine incubation the F1473S-$Na_V1.5$ clusters were markedly reduced with a redistribution of the protein in the cytoplasm and in correspondence of the cell membrane (Fig. 5B, f *vs*. c). Analysis of the different cell fractions by Western blot showed that incubation with 10 µmol/L mexiletine increased the abundance of Na_V-protein on the plasma membrane without affecting the total content of protein in whole cell homogenates (Fig. 5C).

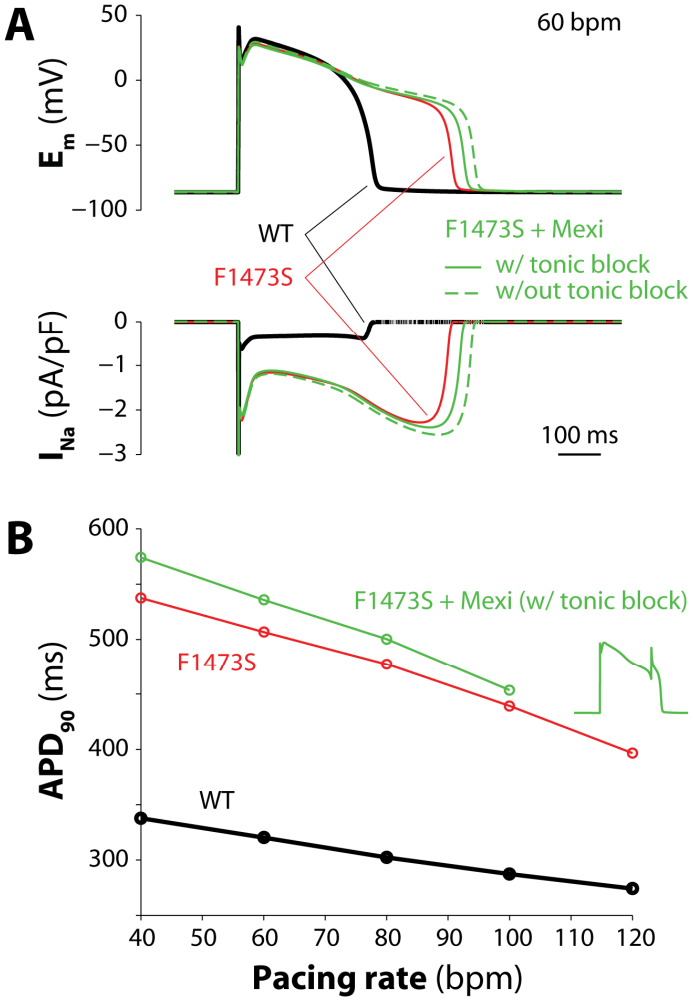

Figure 10. Simulated impact of F1473S mutation and mexiletine administration on AP. Panel A, membrane potential (upper) and I_{Na} (lower) obtained by pacing at 60 bpm the virtual cell in WT condition and when expressing heterozygous mutant channel. In the latter case the effect of mexiletine administration has been simulated by incorporating (or not) the effect of tonic block. B, F1473S prolongs AP over a broad range of pacing frequencies. The treatment with 10 µmol/L mexiletine induces a further AP prolongation, causing a capture failure at fast heart rate (inset shows the membrane potential obtained at 120 bpm). APD has been assessed at 90% of repolarization (APD_{90}).

Overall, our collaborators concluded that exposure to 10 μmol/L mexiletine did not decrease I_{sus}, because the rescued trafficking of F1473S channel offset the blockade of I_{sus}. On the contrary, peak current (and the resulting window current) was significantly increased by mexiletine as the rescuing effect overwhelmed the blocking effect on peak current.

In silico evaluation of F1473S-Na_V1.5 and mexiletine effects on AP

We evaluated *in silico* the consequences of the biophysical properties of F1473S-Na_V1.5. We tuned the Na channel Markov model (Clancy & Rudy, 1999; Clancy *et al.*, 2002; Grandi *et al.*, 2007) depicted in Fig. 6 to reproduces the experimentally observed mutant current behavior: we included the F1473S-induced effects on voltage-dependence of SSA and SSI (Fig. 7A) and time course of recovery from the inactivated state (Fig. 7B). We modified the model also to reproduce the ratio between sustained and peak current (Fig. 7C). In order to take into account the trafficking defect of mutant channels, G_{Na} (set to 57.5 mS/μF for WT) was reduced by 80% (to 11.5 mS/μF) in F1473S (Fig. 7D).

The model faithfully reproduces the WT and F1473S current response to the positive voltage ramp protocol shown in Fig. 2E (Fig. 8A). Moreover, we simulated another voltage-clamp protocol (characterized by a negative voltage ramp) to further study the non equilibrium Na channel gating properties (Clancy *et al.*, 2003). By applying an AP-like voltage command, we obtained a F1473S-induced increase in both sustained current at the end of the plateau and in I_{Na} reactivation during the repolarization (Fig 8B).

We incorporated the I_{Na} model into a comprehensive model of human ventricular AP (ten Tusscher & Panfilov, 2006; Severi *et al.*, 2009) in order to evaluate the effects of mutation and drug administration on the AP. Fig. 9 shows how AP prolongs when increasing the fraction of mutant Na channels. We assumed that, before treatment with mexiletine, in an heterozygote carrier of the F1473S mutation 50% WT proteins are entirely on the cell membrane whereas only 20% of the 50% defective trafficking F1473S-Na_V1.5 are available. In this case, the mutation prolongs the AP by more than 200 ms when pacing the virtual cell at 60 bpm, and this is due to the combination of the enlargement of window current and the increase in I_{sus} (Fig. 10A). We obtained a F1473S-induced AP prolongation over a broad range of pacing frequencies (Fig. 10B).

After exposure to mexiletine, we assumed that the 50% of WT current is blocked by 5% (in agreement with experimental findings) and that the F1473S current is increased by 32% by concurrent blocking and rescuing effect of mexiletine. The model predicts the further prolongation of the AP (Fig. 10A), that leads to a capture failure at the fastest heart rate we simulated (Fig. 10B).

We then simulated the consequence of mexiletine exposure in absence of the drug (*i.e.* tonic block omitted), by considering further 10% increase in F1473S current (leading to a 42% total increase), and found the maximal AP prolongation (Fig. 10A, dashed lines).

DISCUSSION

Mutations associated with LQT3 are characterized by a gain-of-function (George, 2005), suggesting that the pharmacological reduction of I_{Na} could attenuate the QT prolongation. Because its inception this hypothesis seemed to gather rapid confirmation in experimental

(Priori *et al.*, 1996) as well as in clinical investigations (Schwartz *et al.*, 1995; Benhorin *et al.*, 2000; Windle *et al.*, 2001), and it supported the view that LQT3 patients would respond to such a "corrective" pharmacological treatment. Thus, the use of Na channel blockers has been widely supported and it was incorporated into guidelines for clinical practice to reduce the arrhythmic burden with an appropriately cautious class IIb recommendation (Zipes *et al.*, 2006).

As more SCN5A mutations were studied over the years, it has become progressively clear that they may combine different electrophysiological properties and induce complex phenotypes (Bezzina *et al.*, 1999). Some mutations can bear, at the same time, gain-of-function and loss-of-function properties. The Priori group reported a single amino acid deletion (lysine at position 1500) resulting in LQT, Brugada syndrome, and conduction disease in the same family (Grant *et al.*, 2002). This observation was just one of several signals that raised concern that not all gain-of-function mutations should be considered equal and that the use of flecainide or mexiletine might be life saving for some but not for all LQT3 patients (Makita *et al.*, 2008).

In 2007, our collaborators attempted to establish whether the clinical response to mexiletine could be predicted on the basis of the biophysical properties detected with heterologous expression of SCN5A mutants. They suggested that the single most important factor that correlates with a positive response to therapy is represented by a left-ward displacement of SSI (Ruan *et al.*, 2007). These findings highlighted the concept that knowing the *in vitro* consequences of mutants could guide clinical management.

Heterogeneous biophysical properties of SCN5A mutations in LQT3

Here, we characterize a novel mutant that seems to open another chapter, with therapeutic implications, in support of the view that the loss-of-function/gain-of-function paradigm may dangerously oversimplify the clinical approach to SCN5A mutation carriers (Priori, 2004) and that *in vitro* and *in silico* analysis of mutants might become a prerequisite to gene-specific therapy. Indeed, the evidence clearly indicates that in selected SCN5A mutations associated with a clinical phenotype suggestive of gain-of-function, the use of Na channel blockers may result in harmful rather than curative effects.

The present investigation was prompted by a clinical case in which a patient affected by an early onset LQT3 showed no clinical improvement with mexiletine and possibly presented a worsening of the substrate leading to in-hospital death.

Interestingly, another mutation at the same site, F1473C, was recently reported to be insensitive to mexiletine (Silver *et al.*, 2009), and the carrier of the mutation continued to experience torsade de pointes after the drug, thus requiring implantable cardioverter defibrillator implantation and left stellate gangliectomy. The biophysical characterization of the F1473C reported by Bankston *et al.* (Bankston *et al.*, 2007) is a completely different profile as compared with F1473S. F1473C causes a much smaller I_{sus} (0.6% versus 5.39% in F1473S) and it does not reduce the peak current density. These observations highlight the fact that it is not possible to predict functional properties based on the location of a mutation and that in-depth functional studies are required.

Increased I_{sus} (Bennett *et al.*, 1995) and window current (Wang *et al.*, 1996) are two known mechanisms for QT prolongation in LQT3. F1473S induces both to a considerable extent. Thus, two parallel biophysical abnormalities concur to generate the severe clinical

phenotype observed in the proband. It is worth noting that whereas mexiletine has a strong blocking effect on I_{sus} it has only a mild blocking effect on peak current. In particular, we found that a clinically relevant concentration of mexiletine (10 μmol/L) blocked <3% of the peak current, whereas it blocked 28.8% of I_{sus}. As a result, the improved trafficking induced by mexiletine was offset for the I_{sus} but, because of the small peak I_{Na} blocking effect, the absolute amount of window current is greatly increased by this drug. When modeled *in silico* the effect of mexiletine resulted in a further AP prolongation, which is the likely culprit that tilted the balance toward the onset of life-threatening arrhythmias.

Mexiletine and the unexplained mechanisms for rescuing trafficking of $Na_V1.5$ mutants

Mexiletine trafficking-rescuing activity has been demonstrated for several $Na_V1.5$ mutants (Valdivia *et al.*, 2002; Valdivia *et al.*, 2004; Tan *et al.*, 2006; Pfahnl *et al.*, 2007) but the underlying mechanisms remain elusive. It has been suggested that drugs may act as "chemical chaperones" to promote protein folding and thereby facilitating the exit of mutant ion channel from the ER (Herfst *et al.*, 2004; Gong *et al.*, 2006). In the case of F1473S, we observed only a small fraction of the mutant protein in the ER, thus suggesting that this mechanism is unlikely to play a major role in improving membrane localization. Ankyrin-G dependent SCN5A trafficking (Lowe *et al.*, 2008) is another potential mechanism. The Priori group previously demonstrated that a human SCN5A mutation (E1053K) identified in a Brugada patient impairs ankyrin-G binding leading to a trafficking defect (Mohler *et al.*, 2004). E1053 is localized in the predicted 9-aa ankyrin binding motif in the DII-III intracellular loop of $Na_V1.5$ (VPIAVX[E]SD), but we cannot exclude that F1473S, which is in the DIII-DIV intracellular loop, similarly causes an impaired interaction with ankyrin-G.

Another poorly understood aspect of the efficacy of mexiletine in modulating protein localization is related to the concentration at which the effect is observed. Most of the studies used high concentrations of mexiletine, suggesting that a high dosage might be required to improve membrane targeting. Ackerman and colleagues were the first to report rescuing of G1743R (Valdivia *et al.*, 2004) using clinical concentrations of mexiletine (10 μmol/L), pointing to the evidence that the efficacy is independent of the dosage; experimental data (obtained with 10 μmol/L mexiletine) here provided support this view. It was suggested that only mutations located in extracellular loop region of the SCN5A could be rescued by Na channel blockers: the mutant studied here is located intracellularly; thus, it supports the idea that the position of the mutation is unlikely to be the key trafficking controlling factor of the $Na_V1.5$ polypeptide.

The need to revisit recommendations for the use of Na channel blockers in LQT3

Improvement of trafficking in defective SCN5A mutations has been considered as a therapeutic strategy that should be applied irrespective of the biophysical profile of mutants; our study provides *in vitro* and *in silico* proof of concept that this assumption may be incorrect and potentially harmful. In an interesting editorial, Bezzina and Tan hypothesized that rescuing mutant channels with abnormal gating behavior could pose a proarrhythmic threat (Bezzina & Tan, 2002). We now provide the first direct evidence of this hypothesis.

Our data establish a link between experimental data and clinical observations raising a warning flag to the "blanket indication" to use mexiletine in LQT3 patients. The improvement of trafficking of a gain-of-function mutant by mexiletine may be arrhythmogenic despite the channel blocking effect that would tend to counteract such a gain-of-function phenotype. The simulation shows that improvement of trafficking increases window current that is only minimally inhibited by mexiletine and thus contributes to APD prolongation.

It took the unfavorable outcome of the severely ill child affected by LQT3 to demonstrate that the loss-of-function/gain-of-function paradigm to classify SCN5A mutants is inadequate and that use of Na channel blockers in LQT3 patients may be a double-edged sword posing a hazard to patient carriers of a SCN5A mutation with undefined electrophysiological properties.

Study limitations

We acknowledge the presence of limitations in this study. *In vitro* experiments in heterologous systems are widely used but they do not get rid of factors that may importantly modulate the effect of a mutation in the "real world," such as temperature (Keller *et al.*, 2005) or genetic background (influence of modulatory polymorphisms) (Poelzing *et al.*, 2006; Tan *et al.*, 2006). Furthermore, *in vitro* experiments do not consider the important contribution to arrhythmogenesis of the signaling pathways, receptors, and autonomic modulation.

References

Antzelevitch C, Brugada P, Borggrefe M, Brugada J, Brugada R, Corrado D, Gussak I, LeMarec H, Nademanee K, Perez Riera AR, Shimizu W, Schulze-Bahr E, Tan H & Wilde A. (2005). Brugada syndrome: report of the second consensus conference. *Heart rhythm : the official journal of the Heart Rhythm Society* **2,** 429-440.

Bankston JR, Yue M, Chung W, Spyres M, Pass RH, Silver E, Sampson KJ & Kass RS. (2007). A novel and lethal de novo LQT-3 mutation in a newborn with distinct molecular pharmacology and therapeutic response. *PloS one* **2,** e1258.

Benhorin J, Taub R, Goldmit M, Kerem B, Kass RS, Windman I & Medina A. (2000). Effects of flecainide in patients with new SCN5A mutation: mutation-specific therapy for long-QT syndrome? *Circulation* **101,** 1698-1706.

Bennett PB, Yazawa K, Makita N & George AL, Jr. (1995). Molecular mechanism for an inherited cardiac arrhythmia. *Nature* **376,** 683-685.

Bezzina C, Veldkamp MW, van Den Berg MP, Postma AV, Rook MB, Viersma JW, van Langen IM, Tan-Sindhunata G, Bink-Boelkens MT, van Der Hout AH, Mannens MM & Wilde AA. (1999). A single Na(+) channel mutation causing both long-QT and Brugada syndromes. *Circulation research* **85,** 1206-1213.

Bezzina CR & Tan HL. (2002). Pharmacological rescue of mutant ion channels. *Cardiovascular research* **55,** 229-232.

Clancy CE & Kass RS. (2005). Inherited and acquired vulnerability to ventricular arrhythmias: cardiac Na+ and K+ channels. *Physiological reviews* **85,** 33-47.

Clancy CE & Rudy Y. (1999). Linking a genetic defect to its cellular phenotype in a cardiac arrhythmia. *Nature* **400,** 566-569.

Clancy CE, Tateyama M & Kass RS. (2002). Insights into the molecular mechanisms of bradycardia-triggered arrhythmias in long QT-3 syndrome. *The Journal of clinical investigation* **110,** 1251-1262.

Clancy CE, Tateyama M, Liu H, Wehrens XH & Kass RS. (2003). Non-equilibrium gating in cardiac Na+ channels: an original mechanism of arrhythmia. *Circulation* **107,** 2233-2237.

George AL, Jr. (2005). Inherited disorders of voltage-gated sodium channels. *The Journal of clinical investigation* **115,** 1990-1999.

Gong Q, Jones MA & Zhou Z. (2006). Mechanisms of pharmacological rescue of trafficking-defective hERG mutant channels in human long QT syndrome. *The Journal of biological chemistry* **281,** 4069-4074.

Grandi E, Puglisi JL, Wagner S, Maier LS, Severi S & Bers DM. (2007). Simulation of Ca-calmodulin-dependent protein kinase II on rabbit ventricular myocyte ion currents and action potentials. *Biophysical journal* **93,** 3835-3847.

Grant AO, Carboni MP, Neplioueva V, Starmer CF, Memmi M, Napolitano C & Priori S. (2002). Long QT syndrome, Brugada syndrome, and conduction system disease are linked to a single sodium channel mutation. *The Journal of clinical investigation* **110,** 1201-1209.

Herfst LJ, Rook MB & Jongsma HJ. (2004). Trafficking and functional expression of cardiac Na+ channels. *Journal of molecular and cellular cardiology* **36,** 185-193.

Keller DI, Rougier JS, Kucera JP, Benammar N, Fressart V, Guicheney P, Madle A, Fromer M, Schlapfer J & Abriel H. (2005). Brugada syndrome and fever: genetic and molecular characterization of patients carrying SCN5A mutations. *Cardiovascular research* **67,** 510-519.

Lowe JS, Palygin O, Bhasin N, Hund TJ, Boyden PA, Shibata E, Anderson ME & Mohler PJ. (2008). Voltage-gated Nav channel targeting in the heart requires an ankyrin-G dependent cellular pathway. *The Journal of cell biology* **180,** 173-186.

Makita N, Behr E, Shimizu W, Horie M, Sunami A, Crotti L, Schulze-Bahr E, Fukuhara S, Mochizuki N, Makiyama T, Itoh H, Christiansen M, McKeown P, Miyamoto K, Kamakura S, Tsutsui H, Schwartz PJ, George AL, Jr. & Roden DM. (2008). The E1784K mutation in SCN5A is associated with mixed clinical phenotype of type 3 long QT syndrome. *The Journal of clinical investigation* **118,** 2219-2229.

Maltsev VA & Undrovinas AI. (2006). A multi-modal composition of the late Na+ current in human ventricular cardiomyocytes. *Cardiovascular research* **69,** 116-127.

Mohler PJ, Rivolta I, Napolitano C, LeMaillet G, Lambert S, Priori SG & Bennett V. (2004). Nav1.5 E1053K mutation causing Brugada syndrome blocks binding to ankyrin-G and expression of Nav1.5 on the surface of cardiomyocytes. *Proceedings of the National Academy of Sciences of the United States of America* **101,** 17533-17538.

Napolitano C, Priori SG, Schwartz PJ, Bloise R, Ronchetti E, Nastoli J, Bottelli G, Cerrone M & Leonardi S. (2005). Genetic testing in the long QT syndrome: development and validation of an efficient approach to genotyping in clinical practice. *JAMA : the journal of the American Medical Association* **294,** 2975-2980.

Pfahnl AE, Viswanathan PC, Weiss R, Shang LL, Sanyal S, Shusterman V, Kornblit C, London B & Dudley SC, Jr. (2007). A sodium channel pore mutation causing Brugada syndrome. *Heart rhythm : the official journal of the Heart Rhythm Society* **4,** 46-53.

Poelzing S, Forleo C, Samodell M, Dudash L, Sorrentino S, Anaclerio M, Troccoli R, Iacoviello M, Romito R, Guida P, Chahine M, Pitzalis M & Deschenes I. (2006). SCN5A polymorphism restores trafficking of a Brugada syndrome mutation on a separate gene. *Circulation* **114,** 368-376.

Priori SG. (2004). Inherited arrhythmogenic diseases: the complexity beyond monogenic disorders. *Circulation research* **94,** 140-145.

Priori SG, Napolitano C, Cantu F, Brown AM & Schwartz PJ. (1996). Differential response to Na+ channel blockade, beta-adrenergic stimulation, and rapid pacing in a cellular model mimicking the SCN5A and HERG defects present in the long-QT syndrome. *Circulation research* **78,** 1009-1015.

Priori SG, Napolitano C, Schwartz PJ, Bloise R, Crotti L & Ronchetti E. (2000). The elusive link between LQT3 and Brugada syndrome: the role of flecainide challenge. *Circulation* **102,** 945-947.

Priori SG, Napolitano C, Schwartz PJ, Grillo M, Bloise R, Ronchetti E, Moncalvo C, Tulipani C, Veia A, Bottelli G & Nastoli J. (2004). Association of long QT syndrome loci and cardiac events among patients treated with beta-blockers. *JAMA : the*

journal of the American Medical Association **292,** 1341-1344.

Priori SG, Schwartz PJ, Napolitano C, Bloise R, Ronchetti E, Grillo M, Vicentini A, Spazzolini C, Nastoli J, Bottelli G, Folli R & Cappelletti D. (2003). Risk stratification in the long-QT syndrome. *The New England journal of medicine* **348,** 1866-1874.

Ruan Y, Liu N, Bloise R, Napolitano C & Priori SG. (2007). Gating properties of SCN5A mutations and the response to mexiletine in long-QT syndrome type 3 patients. *Circulation* **116,** 1137-1144.

Ruan Y, Liu N & Priori SG. (2009). Sodium channel mutations and arrhythmias. *Nature reviews Cardiology* **6,** 337-348.

Schwartz PJ, Priori SG, Locati EH, Napolitano C, Cantu F, Towbin JA, Keating MT, Hammoude H, Brown AM & Chen LS. (1995). Long QT syndrome patients with mutations of the SCN5A and HERG genes have differential responses to Na+ channel blockade and to increases in heart rate. Implications for gene-specific therapy. *Circulation* **92,** 3381-3386.

Severi S, Corsi C & Cerbai E. (2009). From in vivo plasma composition to in vitro cardiac electrophysiology and in silico virtual heart: the extracellular calcium enigma. *Philosophical transactions Series A, Mathematical, physical, and engineering sciences* **367,** 2203-2223.

Silver ES, Liberman L, Chung WK, Spotnitz HM, Chen JM, Ackerman MJ, Moir C, Hordof AJ & Pass RH. (2009). Long QT syndrome due to a novel mutation in SCN5A: treatment with ICD placement at 1 month and left cardiac sympathetic denervation at 3 months of age. *Journal of interventional cardiac electrophysiology : an international journal of arrhythmias and pacing* **26,** 41-45.

Tan BH, Valdivia CR, Song C & Makielski JC. (2006). Partial expression defect for the SCN5A missense mutation G1406R depends on splice variant background Q1077 and rescue by mexiletine. *American journal of physiology Heart and circulatory physiology* **291,** H1822-1828.

ten Tusscher KH & Panfilov AV. (2006). Alternans and spiral breakup in a human ventricular tissue model. *American journal of physiology Heart and circulatory physiology* **291,** H1088-1100.

Valdivia CR, Ackerman MJ, Tester DJ, Wada T, McCormack J, Ye B & Makielski JC. (2002). A novel SCN5A arrhythmia mutation, M1766L, with expression defect rescued by mexiletine. *Cardiovascular research* **55,** 279-289.

Valdivia CR, Tester DJ, Rok BA, Porter CB, Munger TM, Jahangir A, Makielski JC & Ackerman MJ. (2004). A trafficking defective, Brugada syndrome-causing SCN5A mutation rescued by drugs. *Cardiovascular research* **62,** 53-62.

Wang DW, Yazawa K, George AL, Jr. & Bennett PB. (1996). Characterization of human cardiac Na+ channel mutations in the congenital long QT syndrome. *Proceedings of the National Academy of Sciences of the United States of America* **93,** 13200-13205.

Wang DW, Yazawa K, Makita N, George AL, Jr. & Bennett PB. (1997). Pharmacological targeting of long QT mutant sodium channels. *The Journal of clinical investigation* **99,** 1714-1720.

Wang Q, Shen J, Splawski I, Atkinson D, Li Z, Robinson JL, Moss AJ, Towbin JA & Keating MT. (1995). SCN5A mutations associated with an inherited cardiac arrhythmia, long QT syndrome. *Cell* **80,** 805-811.

Windle JR, Geletka RC, Moss AJ, Zareba W & Atkins DL. (2001). Normalization of ventricular repolarization with flecainide in long QT syndrome patients with SCN5A:DeltaKPQ mutation. *Annals of noninvasive electrocardiology : the official journal of the International Society for Holter and Noninvasive Electrocardiology, Inc* **6,** 153-158.

Zipes DP, Camm AJ, Borggrefe M, Buxton AE, Chaitman B, Fromer M, Gregoratos G, Klein G, Moss AJ, Myerburg RJ, Priori SG, Quinones MA, Roden DM, Silka MJ, Tracy C, Smith SC, Jr., Jacobs AK, Adams CD, Antman EM, Anderson JL, Hunt SA, Halperin JL, Nishimura R, Ornato JP, Page RL, Riegel B, Blanc JJ, Budaj A, Dean V, Deckers JW, Despres C, Dickstein K, Lekakis J, McGregor K, Metra M, Morais J, Osterspey A, Tamargo JL & Zamorano JL. (2006). ACC/AHA/ESC 2006 Guidelines for Management of Patients With Ventricular Arrhythmias and the

Prevention of Sudden Cardiac Death: a report of the American College of Cardiology/American Heart Association Task Force and the European Society of Cardiology Committee for Practice Guidelines (writing committee to develop Guidelines for Management of Patients With Ventricular Arrhythmias and the Prevention of Sudden Cardiac Death): developed in collaboration with the European Heart Rhythm Association and the Heart Rhythm Society. *Circulation* **114,** e385-484.

CHAPTER 2

Theoretical Study of L-type Ca Current Inactivation Kinetics during Action Potential Repolarization and Early Afterdepolarizations

Short title: Model of L-type Ca Channel Inactivation.

The content of this chapter has been published in:

Grandi E, **Morotti S**, Ginsburg KS, Severi S & Bers DM. (2010). Interplay of voltage and Ca-dependent inactivation of L-type Ca current. *Progress in Biophysics and Molecular Biology* **103,** 44-50.

Morotti S, Grandi E, Summa A, Ginsburg KS & Bers DM. (2012). Theoretical study of L-type Ca^{2+} current inactivation kinetics during action potential repolarization and early afterdepolarizations. *The Journal of Physiology* **590,** 4465-4481.

Abstract

Sarcoplasmic reticulum (SR) Ca release mediates excitation-contraction coupling (ECC) in cardiac myocytes. It is triggered upon membrane depolarization by entry of Ca via L-type Ca channels (LTCCs), which undergo both voltage- and Ca-dependent inactivation (VDI and CDI). To differentiate VDI and CDI, several studies have considered the inactivation of Ba current through LTCC (I_{Ba}) as a measure of VDI. However, there is evidence that Ba can weakly mimic Ca, such that I_{Ba} inactivation is still a mixture of CDI and VDI. To avoid this complication, some have used the monovalent cation current through LTCC (I_{NS}, which can be measured when divalent cation concentrations are very low). I_{NS} inactivation rate does not depend on current amplitude, and hence may reflect purely VDI. However, based on analysis of existent and new data, we find that I_{NS} can inactivate more rapidly and completely than I_{Ba}, especially at physiological temperature. Thus, data about I_{Ba} inactivation have been considered in the development of improved model of L-type Ca current within the framework of the Shannon-Bers rabbit ventricular action potential (AP) model, in which the formulation of SR Ca release was modified to reproduce high ECC gain at negative membrane voltages. We extended an existing LTCC Markov model in order to reflect more faithfully contributions of CDI and VDI to total inactivation, by taking into account a small contribution of ion-dependent inactivation (in addition to pure VDI) when Ba is the charge carrier. Under physiological conditions (during an AP) LTCC inactivates predominantly via CDI, which is controlled mostly by SR Ca release during the initial AP phase, but by Ca through LTCCs for the remaining part. Simulations of decreased CDI or K channel block predicted the occurrence of early and delayed afterdepolarizations. Our model accurately describes ECC and allows dissection of the relative contributions of different Ca sources to total CDI, and the relative roles of CDI and VDI, during normal and abnormal repolarization.

INTRODUCTION

The L-type Ca current (I_{Ca}) critically regulates excitation-contraction coupling (ECC) in cardiomyocytes (Bers, 2001) by triggering sarcoplasmic reticulum (SR) Ca release, and modulating action potential (AP) shape and duration (APD), *i.e.* maintaining the long AP plateau. Moreover, I_{Ca} plays an important role in the development of cardiac arrhythmias. Indeed, at the single myocyte level it has been implicated in the development of early afterdepolarizations (EADs) in classical studies by January and colleagues (January *et al.*, 1988; January & Riddle, 1989), who presented evidence linking EADs in Purkinje fibers with reactivation of I_{Ca} during the AP plateau. Several modeling studies have highlighted the importance of I_{Ca} in EAD formation in different animal species and cardiac cell types (Zeng & Rudy, 1995; Tanskanen *et al.*, 2005; Corrias *et al.*, 2011). Under a number of patho-physiological conditions that tend to prolong APD (as in hypertrophic and failing hearts) I_{Ca} may become arrhythmogenic (Benitah *et al.*, 2010), even in the absence of disease-induced alteration of the current itself, as the longer AP plateau provides more time for Ca channel reactivation and facilitates the occurrence of EADs.

I_{Ca} is conducted by $Ca_V1.2$ channels consisting of a pore-forming α_{1C} subunit, with four homologous domains of six transmembrane segments, in association with β and α_2-δ subunits (Catterall, 2000). The C terminal domain of the α_{1C} subunit contains several

regulatory sites, such as a protein kinase A phosphorylation site, an EF-hand region and an IQ motif at which calmodulin (CaM) can bind. I_{Ca} is rapidly activated by membrane depolarization, whereas inactivation of L-type Ca channels (LTCC) is regulated by both Ca- and voltage-dependent inactivation (CDI and VDI) (Lee *et al.*, 1985). CDI is due to binding of Ca to CaM (Peterson *et al.*, 1999; Zuhlke *et al.*, 1999), which causes a channel conformational change that prevents the EF-hand in the C-terminus from interacting with the cytosolic I-II linker, which then occludes the channel pore, thus accelerating inactivation (Cens *et al.*, 2006). CDI is an important feedback mechanism that limits the amount of Ca entry during each Ca transient, regulates sarcoplasmic reticulum (SR) Ca load and modulates APD (Bers, 2001). Indeed, prevention of CDI by expression of a mutant Ca-insensitive CaM in adult cardiomyocytes induces a dramatic (4- to 5-fold) prolongation of the cardiac AP (Alseikhan *et al.*, 2002). Computational analysis also identified CDI as the key player in

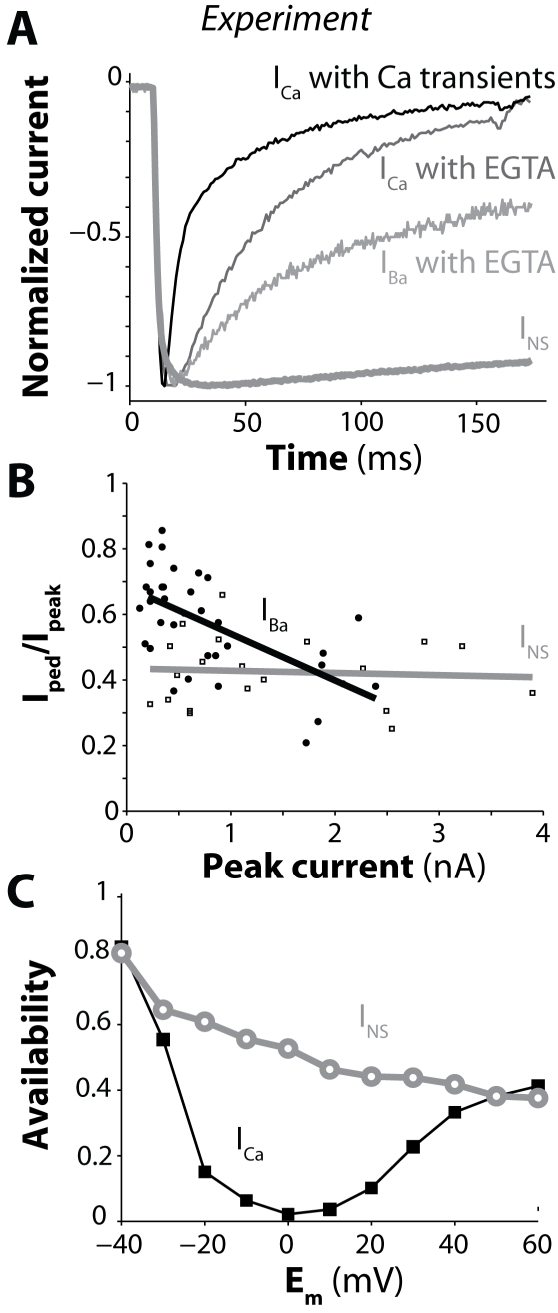

Figure 1. Ion current inactivation through the LTCC. A) Normalized Ca, Ba and Na currents (I_{Ca}, I_{Ba} and I_{NS}) measured at 0 mV (except I_{NS} at -30 mV to obtain comparable activation state). I_{Ca} was recorded under conditions where normal SR Ca release and Ca transients were allowed to occur (perforated patch) or prevented (ruptured patch with cells dialyzed with 10 mM EGTA). I_{Ba} was also recorded in absence of Ca release and transient. I_{NS} was measured in divalent-free conditions (10 mM EDTA inside and out). B) Ratio between pedestal and peak current, in response to a 1000 ms-depolarizing step to 0 mV, is plotted against current amplitude of I_{Ba} and I_{NS}. The lines represent linear regressions. Data are from (Brunet *et al.*, 2009). C) I_{NS} and I_{Ca} availability through Ca channels (at -10 mV) after 500 ms pulses to the indicated E_m in guinea pig ventricular myocytes (redrawn from (Hadley & Hume, 1987)).

shortening the AP when external [Ca] is increased (Grandi *et al.*, 2009). The physiological significance of VDI is illustrated by the dramatic consequences of Timothy syndrome (Splawski *et al.*, 2004; Splawski *et al.*, 2005; Brunet *et al.*, 2009), which impairs VDI and causes severe ventricular arrhythmias (and dysfunction in other tissues, *e.g.*, brain).

I_{Ca} inactivates with a biexponential time course when Ca is the charge carrier, and it has been widely assumed that the initial fast decay represents CDI, and the slower phase reflects VDI. During ECC, with normal SR Ca release and Ca transient (CaT), local $[Ca]_i$ near the LTCC is elevated and inactivation is rapid (Fig. 1A top I_{Ca} trace, $t_{1/2}$=17 ms). When Ca transients are abolished (*e.g.*, by ryanodine or very strong $[Ca]_i$ buffering), I_{Ca} inactivation is slower (Fig. 1A, $t_{1/2}$=37 ms) and reflects a small rise in local $[Ca]_i$ near the mouths of LTCCs due to Ca entering via the channels themselves. In addition to Ca, LTCCs allow permeation by other ions including Na, K, Sr, Cs, Ba, depending on ionic conditions, but inactivation is slower than with Ca and monoexponential when Ba, Sr, or Na are the charge carrier.

To differentiate VDI from CDI, several experimental and theoretical studies have used inactivation of Ba current via LTCC (I_{Ba}) as a measure of VDI (Lee *et al.*, 1985; Peterson *et al.*, 2000; Cens *et al.*, 2006; Mahajan *et al.*, 2008b; Thiel *et al.*, 2008). However, there is evidence that Ba can weakly mimic Ca (Ferreira *et al.*, 1997), such that I_{Ba} inactivation is still a mixture of CDI and VDI, and I_{Ba} inactivation depends on current amplitude (Fig. 1A, $t_{1/2}$=161 ms, and Fig. 1B). To avoid this complication, some have used the monovalent (non specific) cation current through LTCC (I_{NS}), which can be measured only when divalent cation concentrations are very low (Hadley & Hume, 1987; Hryshko & Bers, 1992; Yuan *et al.*, 1996; Sun *et al.*, 2000; Brunet *et al.*, 2009). That is, extracellular Ca and Mg block I_{NS} (k_i~1 and 50 μM respectively). Notably, I_{NS} inactivation rate does not depend on current amplitude (Fig. 1B, grey line) and hence could reflect purely VDI (Brunet *et al.*, 2009). Inward I_{NS} has been reported to inactivate very slowly (Fig. 1A, $t_{1/2}$>500 ms at a membrane potential (E_m) of -30 mV). Even at more positive E_m, where inactivation is faster, it is still incomplete (Fig. 1C). Note that extracellular divalent cations screen external membrane surface charge, shifting the membrane field and channel gating to more positive E_m. Thus, the activation state of I_{NS} at -30 mV is comparable to that of I_{Ca} or I_{Ba} at ~0 mV in Fig. 1A (Hadley & Hume, 1987; Linz & Meyer, 1998; Bers, 2001).

In the present study, we sought to determine whether I_{NS} or I_{Ba} is appropriate for the development of a I_{Ca} model in which the contributions of CDI and VDI to total inactivation are faithfully reproduced. New and existing data suggest that, at physiological temperature, I_{NS} inactivation is faster and more complete than I_{Ba} inactivation. Since I_{Ba} exhibits a weak ion-dependent inactivation (IDI), neither I_{Ba} nor I_{NS} are accurate measures of VDI for I_{Ca}, although I_{Ba} VDI is largely like I_{Ca} VDI. Accordingly, we improved a theoretical model of LTCC kinetics that accounts for the weak Ba-dependent inactivation, integrated into a rabbit ventricular AP model, in which the formulation of SR Ca release was modified to reproduce the experimentally measured E_m-dependence of ECC gain. With this updated myocyte model, which was validated against a broad range of experimental data, we showed that CDI, dominated by SR Ca release at the beginning of the AP and by Ca via LTCCs for the remaining part, outweighs VDI in physiological conditions. Impairment of CDI is predicted to cause to AP prolongation and triggered activity depending on its degree of reduction. New insights into EAD formation were obtained using the model, and I_{Ca} kinetics was analyzed during these abnormal APs.

METHODS

I_{NS} measurements

Ventricular myocytes were dissociated enzymatically from hearts of adult male New Zealand White rabbits using a standard Langendorff perfusion procedure, as has been described previously (Bassani *et al.*, 1994). Isolated cells were allowed to adhere to laminin-treated coverslips and were used acutely. Monovalent current via LTCCs was recorded in whole cell ruptured-patch mode as described previously (Yuan *et al.*, 1996). Cells were held at -65 mV and stimulated with infrequent (<0.1 Hz) depolarizing steps. The bathing solution contained

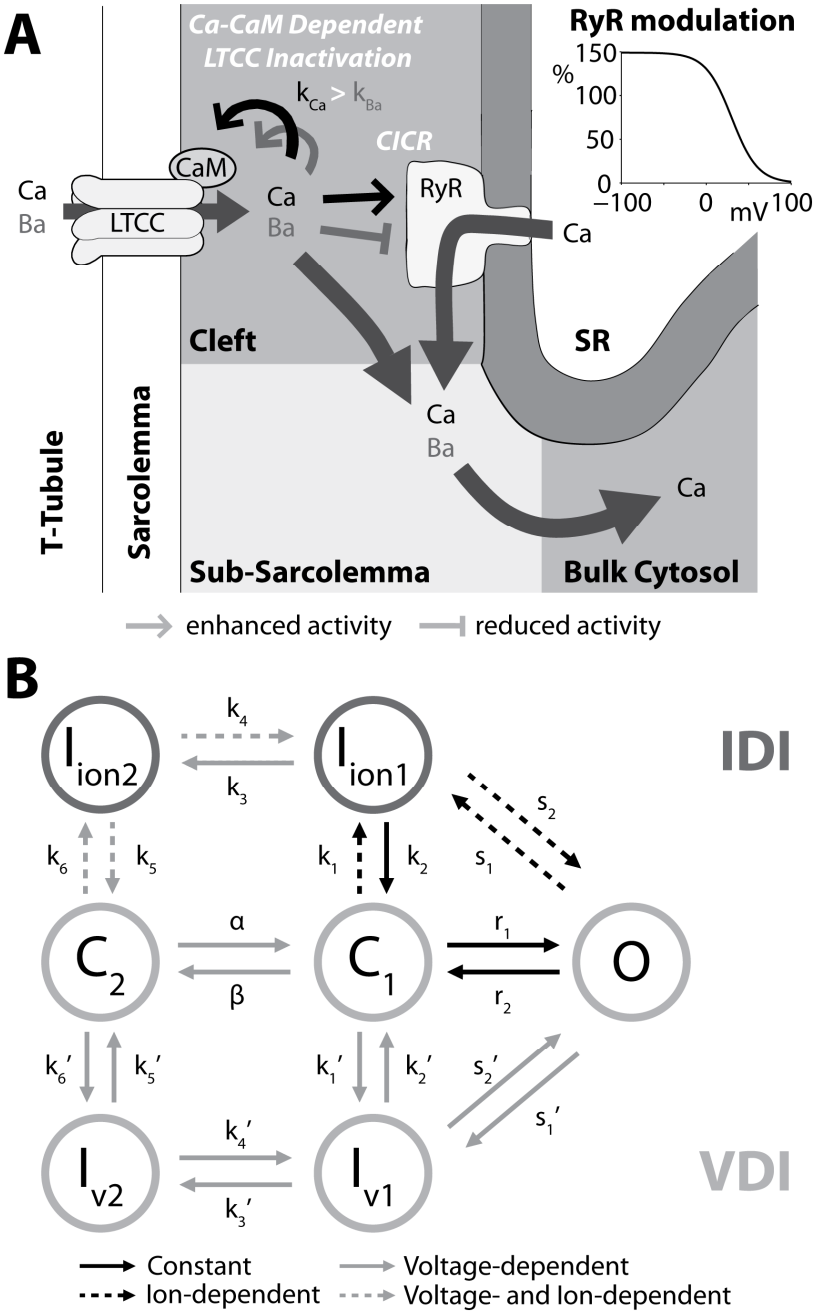

Figure 2. SR Ca release and LTCC models. A) Schematic diagram of dyadic cleft fluxes of the ventricular myocyte AP model (Shannon *et al.*, 2004). Voltage-dependence of SR Ca release was introduced as in inset. B) Structure of the LTCC Markov model (Mahajan *et al.*, 2008b) as modified for this study.

(mM): 10 NaCl, 6 CsCl, 5 EDTA, 120 TEA-Cl, 10 glucose and 10 H-Hepes, adjusted to pH 7.4 with TEA-OH. The pipette solution contained (mM): 3 NaCl, 120 CsCl, 10 EGTA, 5 MgATP, 0.3 GTP, buffered to pH 7.2 with 20 mM H-Hepes and CsOH. Importantly, in recording I_{NS}, EDTA was used to ensure chelation of both Ca and Mg, to prevent Mg from blocking the current (k_i~50 μM) (Matsuda, 1986; Hryshko & Bers, 1992). A measured liquid junction potential of 5 mV was corrected during analysis. Experiments were conducted at room temperature (22°C); a few recordings were obtained at 25°C and 35°C as specified in the results. Current decay was fitted with a monoexponential time constant (τ), with a steady-state plateau at the end of the voltage step. Use of biexponential functions did not improve the fitting.

Modeling Ba-dependent inactivation

A preliminary analysis was done in order to estimate a appropriate reduction factor to model the weaker affinity of Ba *vs*. Ca for CaM. We used a minimal Markov model for I_{Ca} (Fig. 2B) that was developed previously by the Weiss group (Mahajan *et al.*, 2008b), based on I_{Ca} and I_{Ba} measurements in rabbit ventricular myocytes at physiological temperature. Inactivation of I_{Ca} is described as occurring via VDI and CDI (or IDI) pathways. In the original formulation I_{Ba} inactivation was considered to define the VDI pathway only. Here, we used both their 5-state model of I_{Ba} and an alternative 7-state I_{Ba} model, which uses the IDI pathway with parameters tuned to mimic a reduced affinity of Ba *vs*. Ca for CaM (*i.e.* [Ba] was reduced by a factor 1, 3, 10, 20, 30, 50 100 in the expression of the ion-dependent transition rates). We scaled the permeability (and single channel conductance) of LTCCs for Ba in agreement with experimental results (Bers, 2001). Models of I_{Ba} were inserted into the AP a model developed by the Weiss group (Mahajan *et al.*, 2008b). Model differential equations were implemented in Matlab (Mathworks, Natick, MA, USA) and solved numerically using a variable order solver (ode15s). The digital cell was stimulated with voltage steps replicating the experimental protocols.

I_{Ca} and SR Ca release models development

The Shannon-Bers model of a rabbit ventricular myocyte (Shannon *et al.*, 2004) provided the computational framework for this study, where the only changes are on the ryanodine receptor (RyR) and I_{Ca} properties (Fig. 2).

A voltage-dependent modulation of RyR opening was included in the formulation of SR Ca release (Fig. 1A, inset). Specifically, SR Ca release flux was obtained by multiplying RyR open probability by the SR to cleft Ca concentration gradient and maximal release flux (as usual), and a E_m-dependent factor described by the following equation:

$$f(E_m) = \frac{a}{1 + e^{k(E_m - V)}},$$

where a=1.5, k=0.065 mV^{-1} and V=30 mV. This reduces RyR Ca flux at positive E_m (Fig. 2A, inset). This is not meant to imply that RyR has intrinsic E_m-dependence, but this phenomenological adjustment allows our common pool model to recapitulate experiments showing lower efficacy of macroscopic I_{Ca} to trigger SR Ca release at more positive E_m, as depicted in Fig. 3A (Beuckelmann & Wier, 1988; Bers, 2001; Altamirano & Bers, 2007). At more negative E_m, fewer LTCCs open, but the unitary flux is larger (due to larger driving

force), causing more efficient Ca-induced Ca release and higher ECC gain (measured as the ratio of CaT amplitude to peak I_{Ca} in Fig. 3B). Gain at negative E_m is high, in part, because a single Ca channel opening may trigger junctional release but as more channels are recruited (*e.g.*, approaching 0 mV) there is more trigger redundancy of LTCC opening per release unit, and a consequently smaller denominator in the gain equation (Altamirano & Bers, 2007). At increasingly positive E_m (where unitary currents are small), multiple openings are needed to assure RyR opening, which results in lower gain. This circumvents the need here for local stochastic interactions between LTCCs and RyRs in thousands of Ca release units (Restrepo *et al.*, 2008; Lee *et al.*, 2011). The modified formulation predicted higher CaT amplitude for a given I_{Ca} at negative E_m and lower amplitude at positive E_m (Fig. 3C) and the expected decreasing ECC gain with stronger depolarization (Fig. 3D).

The 7-state I_{Ca} model depicted in Fig. 2B (Mahajan *et al.*, 2008b) was incorporated into the ECC model and the total current was computed as follows:

$$I_{Ca} = \sum_i \sum_c I_{Ca-i,c} \,,$$

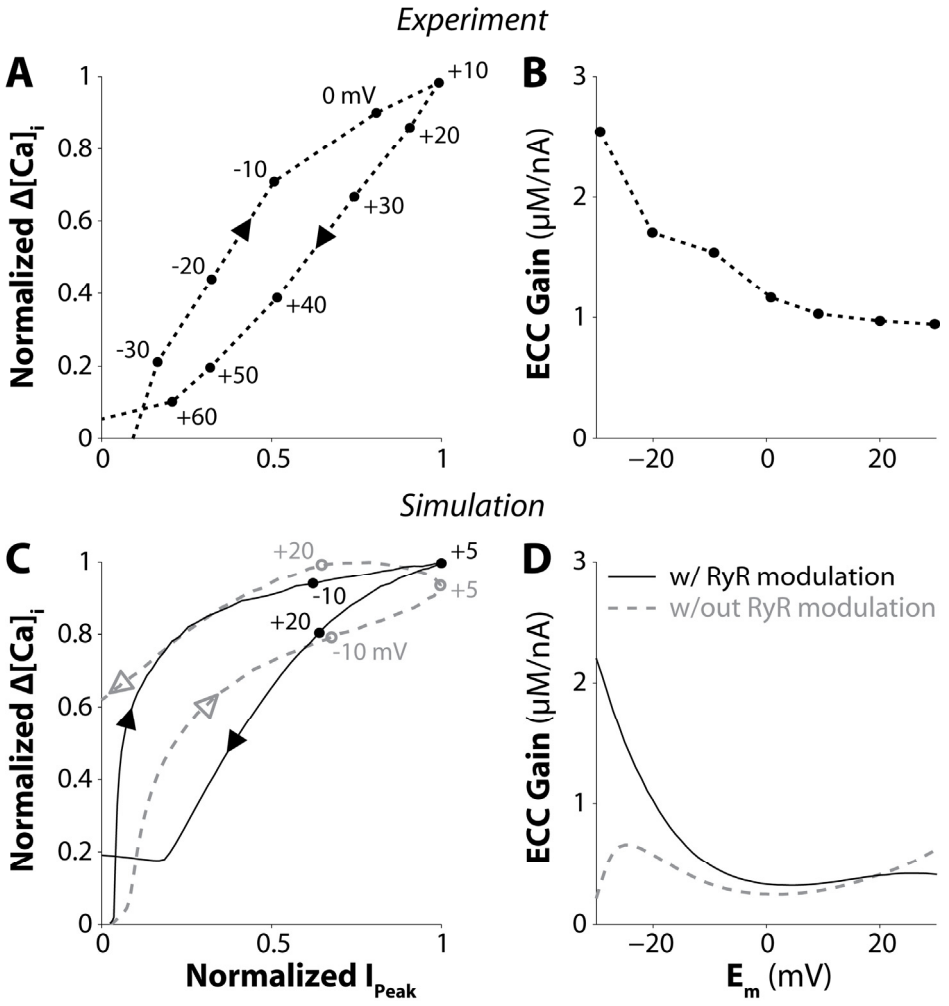

Figure 3. ECC gain. Experimental (guinea pig ventricular myocytes (Beuckelmann & Wier, 1988; Bers, 2001)) and simulated dependence of CaT amplitude on I_{Ca} (A and C) and ECC gain (ratio of CaT amplitude to peak I_{Ca}) on E_m (B and D). Simulated results were obtained in response to voltage steps from -80 mV to various E_m, and are shown with (solid black lines) and without (dashed grey) E_m-dependent modulation of SR Ca release (Fig. 2A, inset). Initial conditions were set as steady-state values obtained by stimulating the cell at 1.5 Hz with 300 ms voltage steps to 0 mV (from a resting potential of -80 mV).

where *c* are the compartments (cleft and sub-sarcolemma) and *i* are Ca (or alternatively Ba), Na and K ions. For each *c* and *i*:

$$I_{Ca-i,c} = F_{x-c} \cdot i_{Ca-i,c} \cdot P_{O-c},$$

where $F_{x\text{-}c}$ represents the fraction of the LTCCs in *c* (90% in cleft, 10% in sub-sarcolemma), $P_{O\text{-}c}$ is the LTCC open probability calculated solving the system of differential equations describing the rate of changes of state occupancies in Fig. 2B, and $i_{Ca\text{-}i,c}$ is the current across the membrane carried by ion *i* calculated with the Goldman-Hodgkin-Katz flux equation:

$$i_{Ca-i,c} = z_i^2 \cdot P_i \cdot \frac{E_m F^2}{RT} \cdot \frac{\gamma_{i-i}[i]_c e^{\frac{2E_m F}{RT}} - \gamma_{o-i}[i]_o}{e^{\frac{2E_m F}{RT}} - 1},$$

where P_i is the permeability of the membrane for ion *i*, z_i is the valence of ion *i*, *F* is the Faraday constant, *R* is the gas constant, *T* is the absolute temperature, $[i]_c$ is the concentration of ion *i* in *c*, and $[i]_o$ is the extracellular concentration of ion *i*. Markov model parameters were constrained to match experimental data obtained under various Ba/Ca homeostasis conditions. I_{Ba} was simulated by replacing Ca with Ba in the extracellular solution composition and Ba entering the cell via LTCC was assumed to affect local [Ba] (*i.e.* sub-sarcolemmal and cleft [Ba]) without altering bulk [Ba] (Fig. 2A) or triggering SR Ca release (Ferreira *et al.*, 1997). With Ba as the charge carrier, Mahajan and colleagues modeled inactivation to occur only via the VDI pathway. That is, during I_{Ba} the two upper states in Fig. 2B (CDI) are never visited, and the model is effectively reduced to the lower 5 states. In contrast, we obtained our I_{Ba} model parameters by fitting the voltage- and Ba-dependence of VDI and CDI rate constants to the measured I_{Ba} with 8-fold weaker apparent affinity of Ba *vs*. Ca for CaM (this reduction value has been adapted from that one estimated in the preliminary analysis). These parameters were also constrained to fit I_{Ca} data (with Ca as the charge carrier) with normal CaT, or without SR Ca release and with the Ca buffers EGTA or BAPTA. We made simplifying assumptions that, in the absence of release and presence of Ca buffers, Ca entering the cell via LTCC affects sub-sarcolemmal and cleft [Ca] without altering bulk [Ca] (for EGTA), or [Ca] is clamped at diastolic values in all compartments (for BAPTA). LTCC permeability values for Ba and Ca were set to reproduce the values of peak current experimentally measured (Mahajan *et al.*, 2008b) at physiological temperature. Model rate parameters were chosen to reproduce kinetics at 37°C, and a Q_{10} of 2 (Faber *et al.*, 2007) was used to scale the duration of voltage pulses of experimental data obtained at room temperature. Moreover, the scaling parameter $\gamma_{i\text{-}Ca}$ in the Goldman-Hodgkin-Katz equation was reduced to avoid reverse flux through LTCCs at elevated cleft [Ca]. The full list of model equations and parameters can be found in the Tables 1 and 2 (where E_m is in V, $[i]_c$, charge carrier (Ca or Ba) concentration in the compartment *c*, is in mM and *aff* is 1 with I_{Ca} and 1/8 with I_{Ba}). To simulate reduced VDI, parameters aRv1 and aRv2 were reduced by 70%, while CaM_{1234} expression was simulated by assuming that the overexpressed CaM_{1234} displaced the wild type (WT) CaM in a fraction α of LTCCs in the cell, such that this population of channels exhibited VDI but not CDI (*i.e.* $I_{Ca,VDI}$ with the reduced 5-state model), as done previously by the Weiss group (Mahajan *et al.*, 2008a). Thus, total $I_{Ca,CaM1234}$ is given by:

$$I_{Ca,CaM_{1234}} = (1-\alpha)I_{Ca} + \alpha I_{Ca,VDI}.$$

Table 1. LTCC model transition rate expressions.

Transition rate expressions
$k_1 = k1o\ fcp$
$k_2 = k2o$
$k_3 = P_T/sp1$
$k_5 = (1-P_S)/T_{Ca}$
$k_6 = P_S\ fcp/\ T_{Ca}$
$s_1 = s1o\ fcp$
$\alpha = R_2/T_2$
$\beta = (1-R_2)/T_2$
$r_1 = R_1/T_1$
$r_2 = (1-R_1)/T_1$
$k_6' = R_{v2}/T_{v2}$
$k_5' = (1-R_{v2})/T_{v2}$
$k_1' = R_{v1}/T_{v1}$
$k_2' = (1-R_{v1})/T_{v1}$
$k_3' = 1/(T_{rev2}\ (1+F_{rev2}))$
$k_4' = k_3'\ F_{rev2}$
$s_1' = 1/(T_{rev1}\ (1+F_{rev1}))$
$s_2' = s_1'\ F_{rev1}$
$k_4 = k_3\ (k_5/k_6)\ (k_1/k_2)\ (\alpha/\beta)$
$s_2 = s_1\ (k_2/k_1)\ (r_1/r_2)$
where
$fcp = 1/(1+(cpt/aff/[i]_c)^3)$
$T_{Ca} = P_Q\ ((R-tca)\ P_R+tca)$
$tca = (sp9/(1+([i]_c\ aff/cat)^4))+sp10$
$R = sp7+sp8\ \exp(E_m/sp6)$
$P_T = 1-(1/(1+\exp(-(E_m+sp2)/sp3)))$
$P_Q = 1+sp0/(1+\exp(-(E_m+sp2)/sp4))$
$P_R = 1-(1/(1+\exp(-(E_m+sp2)/sp4)))$
$P_S = 1/(1+\exp(-(E_m+sp2)/sp5))$
$R_2 = aR2/(1+\exp(-(E_m+sR2)\ pR2))$
$T_2 = aT2/(1+\exp(-(E_m+sT2)\ pT2))$
$R_1 = aR1/(1+\exp(-(E_m+sR1)\ pR1))$
$T_1 = aT1/(1+\exp(-(E_m+sT1)\ pT1))$
$R_{v2} = aRv2/(1+\exp(-(E_m+sRv2)\ pRv2))$
$T_{v2} = aTv2/(1+\exp(-(E_m+sTv2)\ pTv2))$
$R_{v1} = aRv1/(1+\exp(-(E_m+sRv1)\ pRv1))$
$T_{v1} = aTv1/(1+\exp(-(E_m+sTv1)\ pTv1))$
$T_{rev2} = aTrev2/(1+\exp(-(E_m-sTrev2)\ pTrev2))$
$F_{rev2} = (1-R_{v2})\ R_2\ R_{v1}/(R_{v2}\ (1-R_2)\ (1-R_{v1}))$
$T_{rev1} = aTrev1/(1+\exp(-(E_m-sTrev1)\ pTrev1))$
$F_{rev1} = (1-R_{v1})\ R_1/(R_{v1}\ (1-R_1))$

Ionic concentrations were set to the following values (in mM): $[Cl]_i$ 5, $[Cl]_o$ 146, $[K]_i$ 140, $[K]_o$ 5.4, $[Na]_o$ 135, $[Ca]_o$ 2 (or $[Ba]_o$ 1.8), as in (Mahajan *et al.*, 2008a). During EAD-like AP-clamp, the following values were changed: $[Cl]_i$ 15, $[Cl]_o$ 150, $[K]_i$ 135, $[Na]_o$ 140, $[Ca]_o$ 1.8, as in (Shannon *et al.*, 2004). The reduced Cl driving force diminished background Cl currents, thus reducing the repolarization reserve. Model equations were implemented in Simulink (Mathworks, Natick, MA, USA) and solved numerically with a stiff variable order

solver (ode15s) based on the numerical differentiation formulas (NDFs) with an adaptive time step ranging from 1 ms to 1 ps. The digital cell was stimulated in voltage- or AP-clamp to replicate experimental protocols. Initial conditions were set as steady-state values obtained by stimulating the cell (in various Ba and Ca homeostasis conditions) at 1 Hz with 300 ms voltage steps to 0 mV (from a resting potential of -80 mV). AP-clamp simulations were performed with a command AP simulated by pacing the cell in current-clamp (15 A/F current stimulus lasting 3 ms) at 0.33 Hz to steady-state with normal CaT. APs showing EADs were also used as a command voltage. A gapped double-pulse (GD-P) protocol was implemented in which the AP-clamp was interrupted at defined potentials. E_m was then stepped back to -40 mV for 2 ms, followed by a 200 ms rectangular test pulse to 5 mV. The fraction of available channels at each time during the AP was calculated by normalizing peak I_{Ca} evoked by the corresponding test pulse to the peak I_{Ca} elicited by a rectangular clamp step from -80 to 5 mV (when the channels are fully available). Inactivation (*i.e.* 1-availability) was plotted against the time elapsed between AP upstroke and interruption.

RESULTS

Experimental analysis of I_{NS} and I_{Ba} inactivation kinetics

Typical recordings of I_{NS} (with Na and Cs as charge carriers) are shown in Fig. 4A, elicited by depolarizing pulses described in inset. With increasing depolarization, the net current changes from inward to outward, due to reduction in the driving force for Na and an increased driving force for Cs (I_{NS} reversal potential is about -4.5 mV). We characterized I_{NS} kinetics by considering the time course of current decay throughout the duration of depolarization. Time constants (τs) of inactivation are reported in Fig. 4B for each depolarization E_m. Current decay is slower at E_m<-10 mV, and is hastened as the voltage steps are more depolarized (and the

Table 2. LTCC model parameters.

Parameter	Value	Unit
F	96845	C/mol
R	8.314	J/mol/K
T	310	K
z_{Ca}	2	-
z_{Ba}	2	-
z_K	1	-
z_{Na}	1	-
$\gamma_{i\text{-}Ca}$	0.0341	-
$\gamma_{o\text{-}Ca}$	0.341	-
$\gamma_{i\text{-}Ba}$	0.0341	-
$\gamma_{o\text{-}Ba}$	0.341	-
$\gamma_{i\text{-}K}$	0.75	-
$\gamma_{o\text{-}K}$	0.75	-
$\gamma_{i\text{-}Na}$	0.75	-
$\gamma_{o\text{-}Na}$	0.75	-
P_{Ca}	24.3e-6	m/s
…		

Parameter	Value	Unit
P_{Ba}	23.22321e-6	m/s
P_K	12.15e-9	m/s
P_{Na}	0.675e-9	m/s
$F_{x\text{-}cleft}$	0.9	-
$F_{x\text{-}sl}$	0.1	-
cpt	3.75e-3	mM
cat	7.617e-3	mM
s1o	18.2688	s^{-1}
k1o	24.168	s^{-1}
k2o	0.103615	s^{-1}
sp0	1.5	-
sp1	3e-3	s
sp2	40e-3	V
sp3	3e-3	V
sp4	4e-3	V
sp5	11.32e-3	V
sp6	15.6e-3	V
sp7	10e-3	s
sp8	4954e-3	s
sp9	78.0329e-3	s
sp10	0.1e-3	s
aR2	1	-
sR2	0.002	V
pR2	145	V^{-1}
aT2	0.001	s^{-1}
sT2	1	V
pT2	100	V^{-1}
aR1	0.09091	-
sR1	1	V
pR1	100	V^{-1}
aT1	0.00030303	s^{-1}
sT1	1	V
pT1	100	V^{-1}
aRv2	0.9	-
sRv2	0.029	V
pRv2	135	V^{-1}
aTv2	0.5	s^{-1}
sTv2	0.025	V
pTv2	50	V^{-1}
aRv1	0.85	-
sRv1	0.18	V
pRv1	90	V^{-1}
aTv1	0.27	s^{-1}
sTv1	0.18	V
pTv1	100	V^{-1}
aTrev1	0.20512	s^{-1}
sTrev1	0.065	V
pTrev1	100	V^{-1}
aTrev2	7e5	s^{-1}
sTrev2	0.06	V
pTrev2	130	V^{-1}

current becomes outward). Nevertheless, I_{NS} inactivation τs measured in rabbit ventricular myocytes at room temperature are relatively fast (especially compared to the I_{NS} trace in Fig. 1A). I_{NS} inactivation was assessed in the same cell at two different temperatures (25 and 35°C, Fig. 4 C *vs*. D). Availability curves were recorded using various durations of the inactivating pre-pulses, and τ of inactivation was estimated as described in (Findlay, 2002b). At physiological temperature I_{NS} inactivated more completely and rapidly than at room temperature. From these measurements, we calculated an average Q_{10} of ~1.85 for I_{NS} inactivation kinetics over the full range of E_m (although Q_{10} was larger at more negative E_m: ~2.3 at -20 mV). We compared our data (corrected at 37°C, Fig. 5A, diamonds) with previously published inactivation τs and found concordance with several previous studies of I_{NS} inactivation.

I_{NS} inactivation τs values were averaged (broken curve in Fig. 5A) and plotted *vs*. E_m as inactivation rate constants ($k=\tau^{-1}$) in Fig. 5B, along with rate constants of inactivation of I_{Ba} and I_{Ca} (biexponential for I_{Ca} from (Mahajan *et al.*, 2008b)). I_{Ca} inactivation is faster when SR Ca release is present (top curve). Notably, I_{NS} inactivation was much faster than I_{Ba} inactivation, which was comparable to the slow component of I_{Ca} inactivation. I_{NS} inactivation

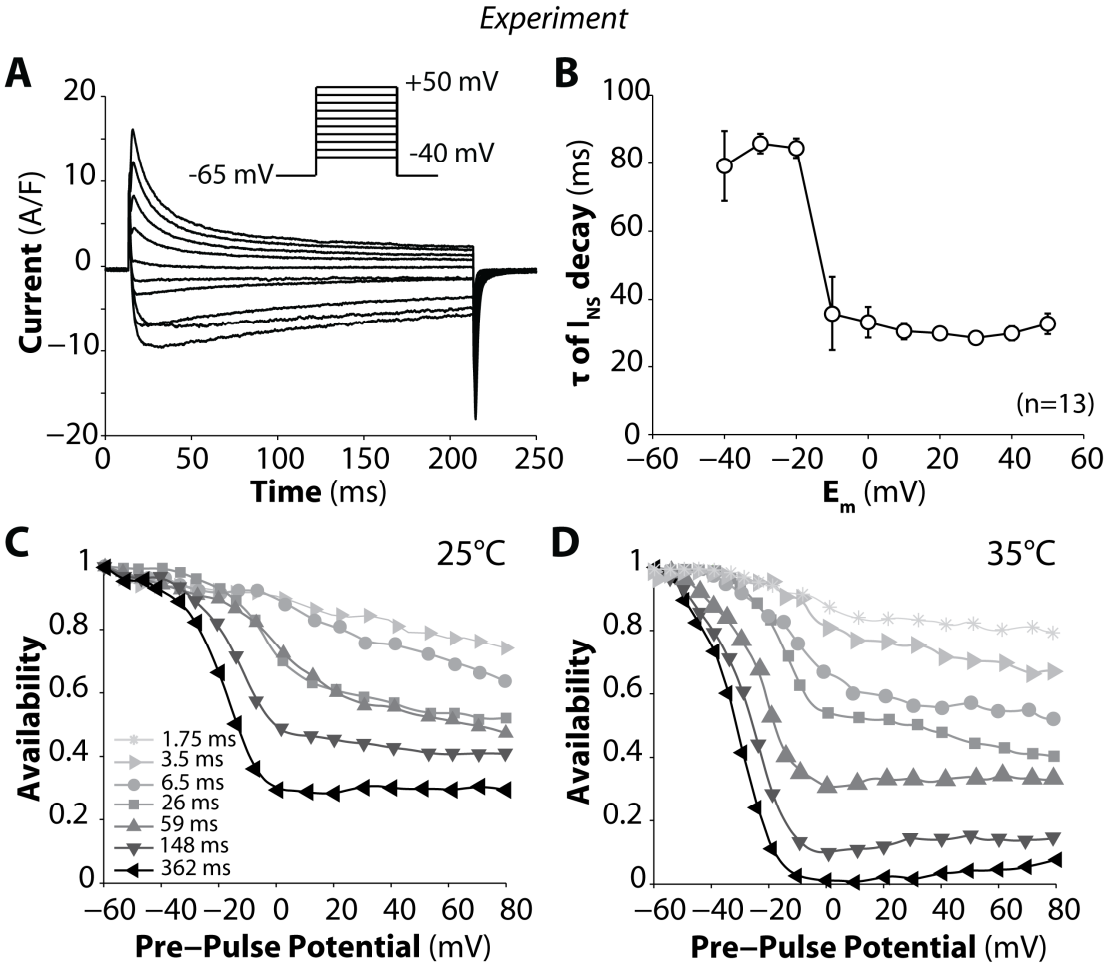

Figure 4. Kinetics of I_{NS} inactivation. A) Representative recordings of membrane currents in rabbit ventricular myocytes elicited by 200-ms steps (inset) from -65 mV to the indicated E_m. B) τ of I_{NS} decay. C and D) I_{NS} availability recorded at 25°C and 35°C following pre-pulse steps of 362, 148, 59, 26, 6.5, 3.5, 1.75 ms duration. Data from C and D have been transposed onto a time scale (availability against pre-pulse interval) and τs were calculated as in (Findlay, 2002c).

becomes faster with increasing depolarization consistent with VDI, and gets faster when the current is outward. Thus, I_{NS} inactivates more rapidly and completely than I_{Ba} at 35-37°C (even if one accounts for surface charge effects). Thus, these cannot both reflect the same VDI process. Moreover if I_{NS} exhibits pure VDI, then the rate of I_{Ba} inactivation (which may include some weak CDI) would have to be faster than I_{NS} inactivation (*i.e.* kVDI+*f*(kCDI)). So I_{NS} inactivation is too fast to reflect the VDI that occurs during I_{Ba}. On the other hand, I_{Ba} is not purely VDI either, because the rate of inactivation has a bell-shaped E_m-dependence (Fig. 5B, inset, and Fig. 6, circles, (Mahajan *et al.*, 2008b)) and increases with larger peak Ba current amplitude, as shown in Fig. 1B (Brunet *et al.*, 2009).

We suggest that I_{NS} inactivation is VDI, but that it is fundamentally (mechanistically) different from VDI that occurs during I_{Ba} or I_{Ca}, and may therefore not be useful to characterize the VDI component of I_{Ca}. Further, I_{Ba} inactivation includes a moderate component of CDI (where Ba substitutes for Ca) and also VDI that is the same as the VDI component of I_{Ca}. Indeed, with strong fast intracellular Ca buffering, I_{Ca} inactivation is reduced (Katzka & Morad, 1989; Linz & Meyer, 1998) and approaches that seen for I_{Ba}.

Quantitative assessment of Ba-dependent inactivation

We sought to determine whether and how experimental I_{Ba} inactivation (traditionally used in VDI experiments and models) could be recapitulated by extending a previously published model of CDI (Mahajan *et al.*, 2008b) to account for Ba-dependent inactivation. To mimic a reduced affinity of Ba (*vs*. Ca) in CDI, the parameters describing the Ca-dependent transitions (Fig. 2B) were modified to make it 3-100 times less sensitive to [Ba] (*vs*. [Ca]). In Fig. 6A normalized I_{Ba} simulated in response to a voltage step to 0 mV are shown. As the apparent affinity of Ba for CaM increases (approaching that of Ca), I_{Ba} exhibits faster inactivation (Fig.

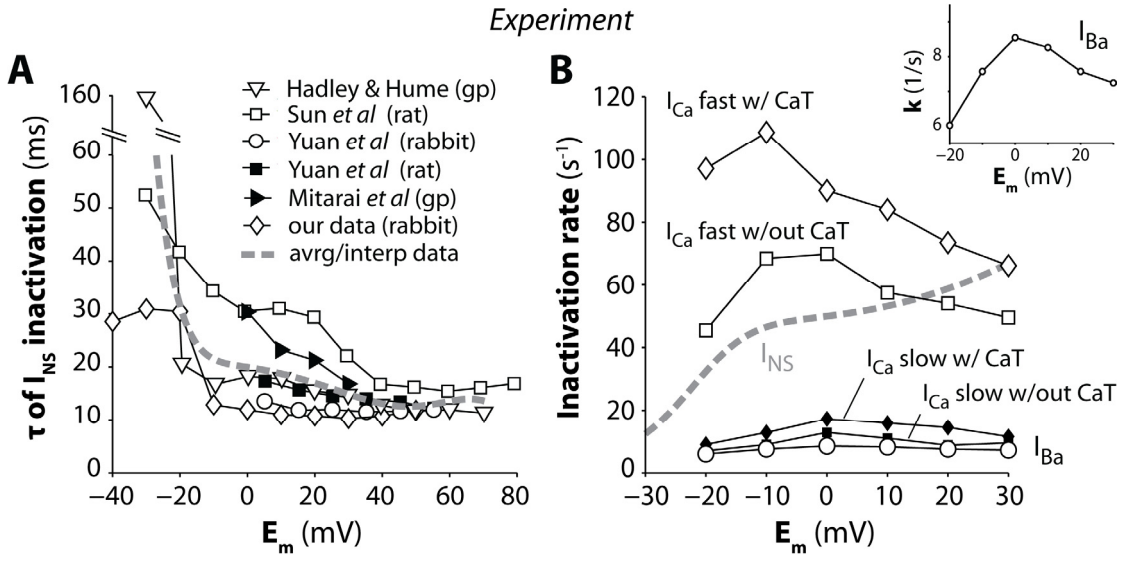

Figure 5. I_{NS}, I_{Ba} and I_{Ca} inactivation rates at physiological temperature. A) Voltage-dependence of the decay time of I_{NS}. Data from (Mitarai *et al.*, 2000) were collected at physiological temperature. All the other experimental data were obtained at room temperature and here rescaled at 37°C (Q_{10}=1.85). The dashed line is obtained by interpolation of the averaged τ. B) Rates of the fast and slow components of a double exponential fit of I_{Ca} decay *vs*. E_m recorded by (Mahajan *et al.*, 2008b) with and without CaT. Rates of I_{Ba} (shown also in the inset) and I_{NS} (dashed lines) inactivation are obtained from monoexponential fits of current decay.

5B). The τ of I_{Ba} decay (at 0 mV) is ~125 ms when the current inactivation is modeled as Ba-independent (*e.g.*, only including VDI). When Ba affinity is much smaller than that of Ca (20-100 times), the predicted Ba-dependent inactivation is negligible, still indistinguishable from only the 5-state VDI model. Only when the relative k_{Ca}/k_{Ba} affinity falls to 10 or below does Ba-dependent inactivation become appreciable. Fig. 6B also shows the maximal probability of occupancy of the two Ba-dependent inactivation states (filled and open squares). The channel never visits these states by design when only VDI is implemented, and state occupancies are infrequent when Ba affinity for CaM is low. Ion-dependent inactivated states are more likely to be occupied when Ba affinity increases (*e.g.*, when k_{Ca}/k_{Ba} is equal to 10, τ is reduced by about one fifth). When Ba affinity equals that of Ca, τ of I_{Ba} inactivation is the same as I_{Ca} (without SR Ca release), and the probabilities of occupancy of I_{ion1} and I_{ion2} are maximal. When Ba is used instead of Ca in experiments, the normal myocyte Ca extrusion pathways do not remove Ba well, so that intracellular Ba would accumulate over several beats. Simulations show that the τ of I_{Ba} decay decreases as intracellular [Ba] increases (Fig. 6C), whereas it is

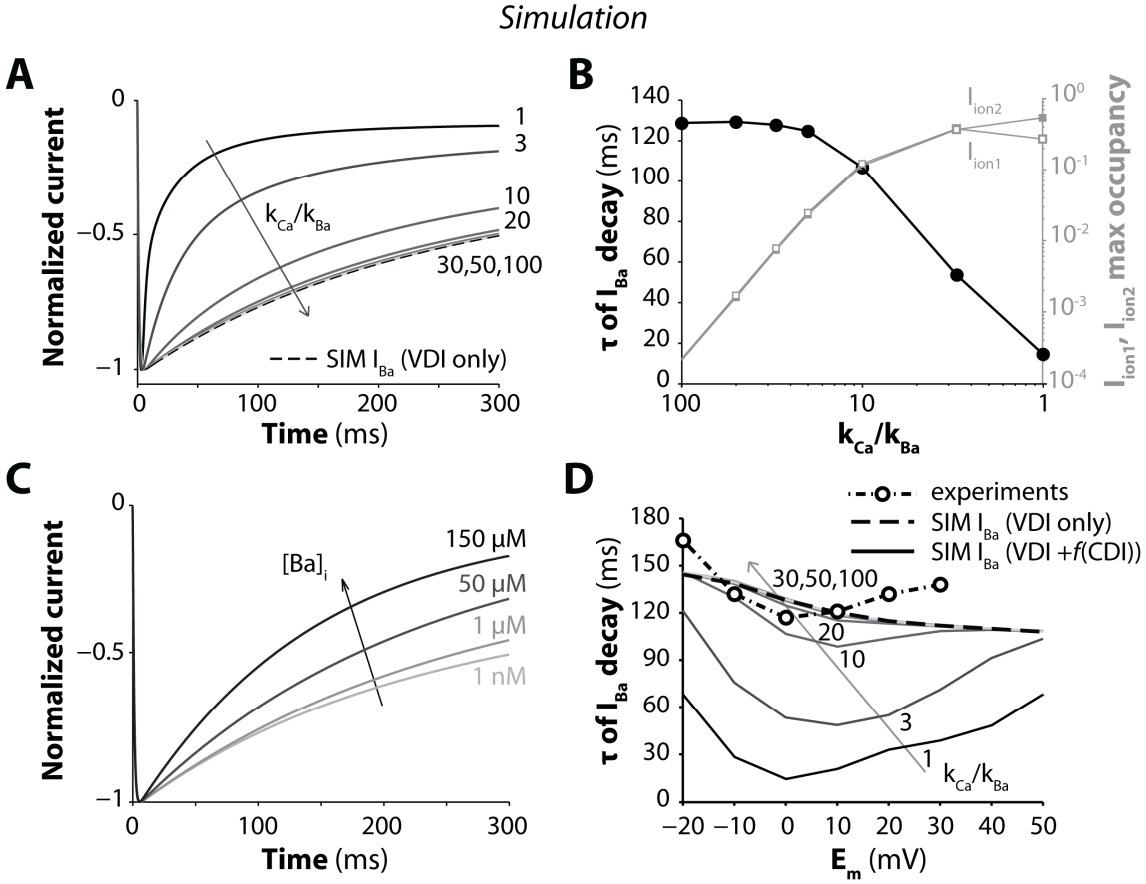

Figure 6. Kinetics of simulated I_{Ba} inactivation. A) Normalized I_{Ba} traces obtained when applying a voltage step to 0 mV (from a holding potential of -80 mV) and k_{Ca}/k_{Ba} is equal to 100, 50, 30, 20, 10, 3, 1 (VDI+*f*(CDI)). I_{Ba} was also simulated as independent of Ba flux (VDI only, dashed line). B) Left ordinate: τ of I_{Ba} decay decreases as the simulated Ba affinity for CaM is increased (*i.e.* k_{Ca}/k_{Ba} decreased). Right ordinate: ion-dependent state occupancy during I_{Ba} decay (in response to a voltage step to 0 mV) is enhanced with increasing affinity of Ba for CaM (*i.e.* decreasing k_{Ca}/k_{Ba}). C) Effect of intracellular Ba accumulation on current inactivation. Normalized I_{Ba} traces obtained in response to a voltage step to 0 mV are shown in correspondence of various levels of $[Ba]_i$ (from 1 nM to 150 µM). D) τ of I_{Ba} decay at the indicated E_m when I_{Ba} inactivation is simulated as independent of Ba flux (VDI only, dashed line) and when Ba affinity for CaM is varied ((VDI+*f*(CDI)), k_{Ca}/k_{Ba} from 100 to 1). Experimental data are from (Mahajan *et al.*, 2008b).

unchanged when using the 5-state VDI only I_{Ba} model (not shown). In Fig. 6D the effect of Ba-dependent inactivation is shown over a wide range of voltages. Note that the τ for I_{Ca} (or I_{Ba} at $k_{Ca}/k_{Ba}=1$) reflects the strong CDI seen for I_{Ca}, whereas the curve for $k_{Ca}/k_{Ba}=10$ approaches the shape seen for I_{Ba} measurements. While the model is an imperfect match to the data, this simple version provides a useful framework for separating VDI and CDI for I_{Ca} and I_{Ba}.

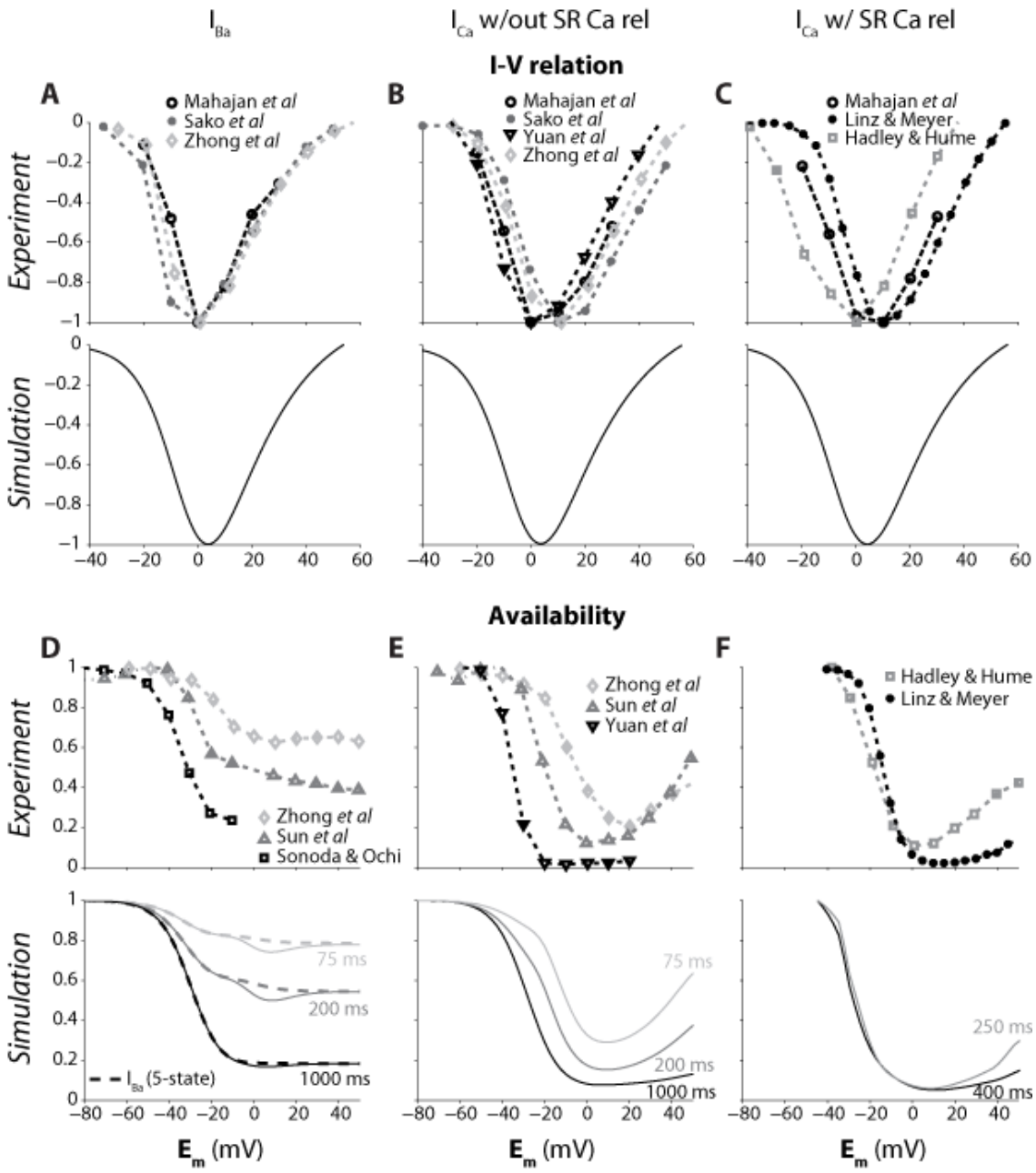

Figure 7. I_{Ca} model identification. Experimental (top) and simulated (bottom) I-V relationships and quasi-SSI for I_{Ba} (A, D), I_{Ca} without SR Ca release (B, E), and I_{Ca} with CaT (C, F). I-V curves were obtained by stimulating the cell with voltage steps from a resting potential of -80 mV to various test potentials. Quasi-SSI curves were obtained by measuring the available current after inactivation pre-pulses of various (indicated) durations. Results for simulated I_{Ba} with a reduced 5-state model (only VDI) are also shown (dashed lines).

I_{Ca} model identification

We integrated the LTCC Markov model (Mahajan *et al.*, 2008b) into the framework of the Shannon-Bers rabbit AP model (Shannon *et al.*, 2004), and the I_{Ca} model was reparameterized using voltage-clamp data from previous studies in isolated ventricular myocytes from rabbit (Yuan *et al.*, 1996; Linz & Meyer, 2000; Mahajan *et al.*, 2008b), guinea pig (Hadley & Hume, 1987; Zhong *et al.*, 1997; Sonoda & Ochi, 2001), rat (Sun *et al.*, 2000), and mouse (Sako *et al.*, 1998). When available, we favored experiments obtained in rabbit at physiological temperature and solutions *vs*. other species and less physiological conditions. Results are shown for Ba current, and for Ca currents with and without SR Ca release.

Dependence of (normalized) current on E_m is depicted in Fig. 7A-C. Simulated I_{Ba} and I_{Ca} (lower panels) peak at +5 mV, independent of charge carrier and SR function. At 5 mV, peak I_{Ba} equals -2.00 nA, peak I_{Ca} equals -2.14 nA and -2.17 nA with and without SR Ca release, respectively (*vs*. -2.06 nA at 0 mV, -1.98 nA at 0 mV, and -2.14 nA at +10 mV, in experiments (Mahajan *et al.*, 2008b)). Normalized experimental current-voltage (I-V) curves are shown for comparison (upper panels) and exhibit some variability, possibly due to differences in species, intra- and extracellular solution compositions, and experimental protocols.

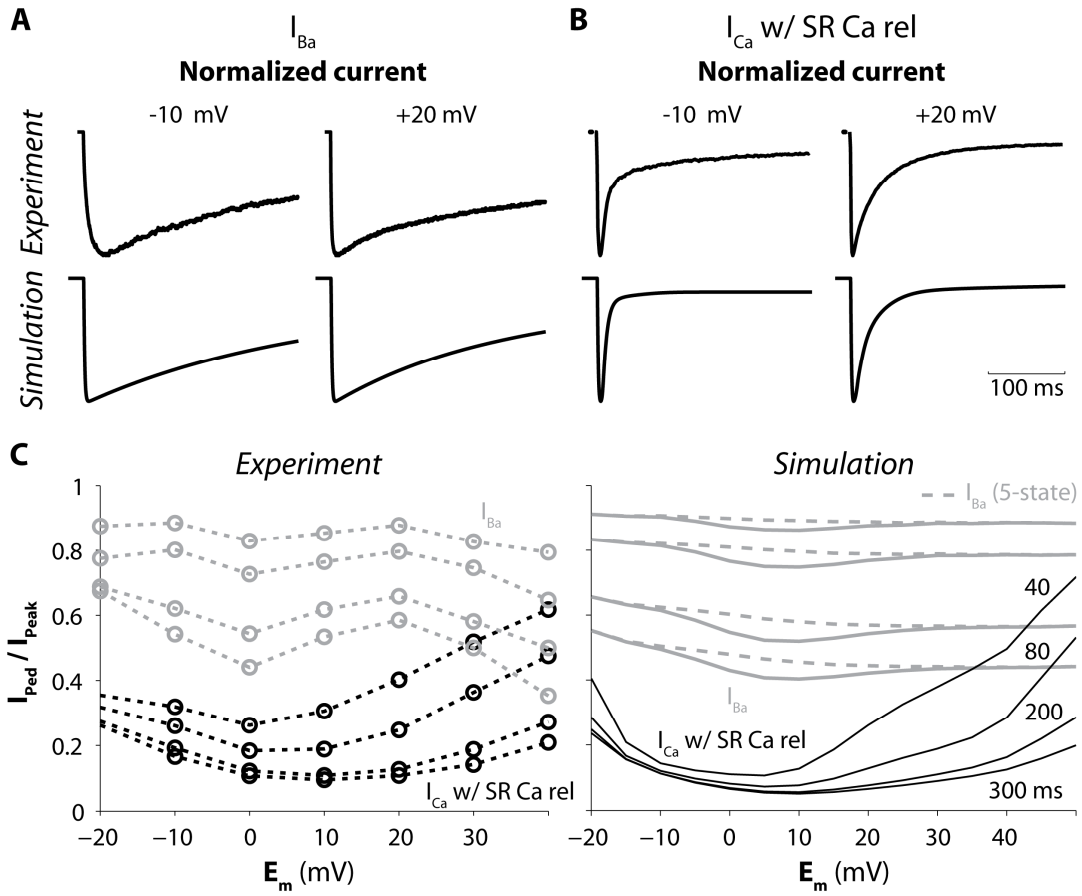

Figure 8. Kinetics of LTCC current inactivation. Experimental (top) (Mahajan *et al.*, 2008b) and simulated (bottom) I_{Ba} (A) and I_{Ca} (B) traces evoked by voltage pulses from -80 mV to -10 mV (left) and +20 mV (right). C) Experimental (left) (Mahajan *et al.*, 2008b) and simulated (right) ratios of pedestal to peak current (I_{Ped}/I_{Peak}) at varying times (indicated) during voltage pulses from -80 mV to various test potentials for I_{Ca} and I_{Ba}. Results for simulated I_{Ba} with a reduced 5-state model (only VDI) are also shown.

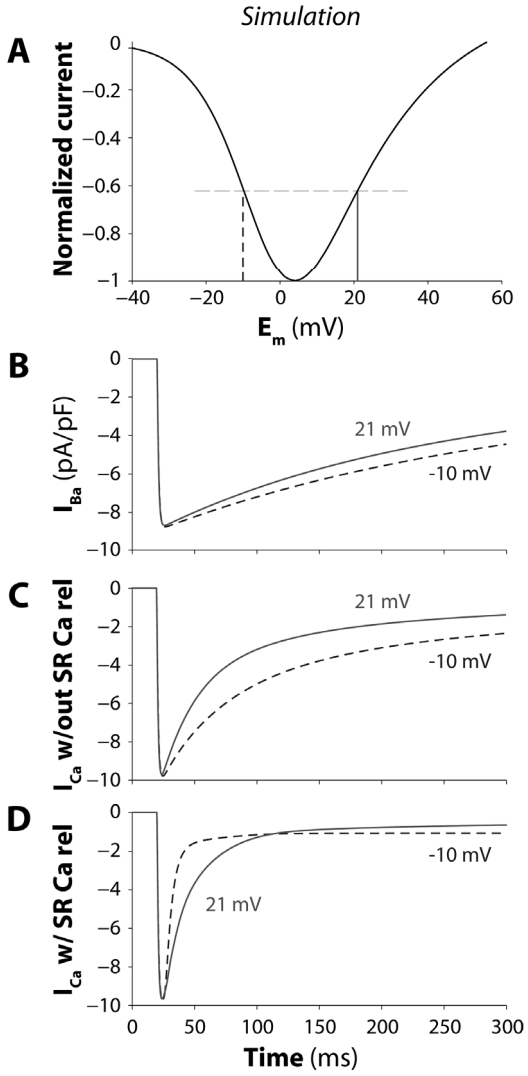

Figure 9. Kinetics of LTCC current inactivation. I_{Ba} (B), I_{Ca} without (C) and with (D) SR Ca release evoked by voltage steps from -80 mV to -10 mV (dashed lines) and +21 mV (solid). Step voltages were chosen symmetrically on the I-V curve (A).

Simulated current availability curves (Fig. 7D-F) indicate that inactivation is more complete the longer the inactivating pre-pulse, in agreement with experimental data (upper panels). A slightly U-shaped curve is obtained for I_{Ba} (Fig. 7D), with the largest inactivation corresponding to the largest Ba influx, near +5 mV, consistent with modest Ba-dependent inactivation (Brunet *et al.*, 2009). Moreover, this U-shaped region is not seen with the reduced 5-state model lacking IDI (dashed lines). Inactivation is more markedly U-shaped when simulating I_{Ca} (Fig. 7E-F), and is especially pronounced with SR function intact (Fig. 7E *vs*. F) as seen experimentally.

The kinetics of I_{Ba} and I_{Ca} inactivation can be assessed by the ratio of pedestal to peak current (I_{Ped}/I_{Peak}) at different times after depolarization to different E_m for experimental (Mahajan *et al.*, 2008b) and simulated traces (Fig. 8C). Pedestal currents (and I_{Ped}/I_{Peak}) decrease with longer pulses and inactivation is faster and deeper for I_{Ca} *vs*. I_{Ba}, and with larger ion influx and/or Ca release, in agreement with experiments (left panel). Again, the dependence of I_{Ped}/I_{Peak} on E_m is U-shaped (Fig. 8C) around the peak potential of 0~+10 mV (Fig. 7A and C) for both I_{Ba} and I_{Ca}. In contrast simulated I_{Ba} curves with the 5-state model (VDI) are relatively flat (dashed lines at right). Previous results have shown that I_{Ba} inactivation depends on Ba influx (Brunet *et al.*, 2009). For a given peak current at different

E_m, the kinetics of I_{Ba} inactivation are comparable. For example, experimental (Mahajan *et al.*, 2008b) and simulated I_{Ba} at -10 and +20 mV reach similar peak values (simulated: -8.75 and -9.12 A/F) and inactivate similarly (Fig. 8A). On the other hand, when SR Ca release occurs, for a given peak I_{Ca}, inactivation is faster at negative E_m, where ECC gain and release are larger. For example, experimental (Mahajan *et al.*, 2008b) and simulated I_{Ca} at -10 and +20 mV reach similar peak values (simulated: -9.58 and -10.1 A/F) but inactivation is much faster at -10 mV (Fig. 8B). This is further illustrated in Fig. 9, where E_m values are chosen symmetrically with respect to peak current, such that the currents reach the same peak value and inactivation kinetics are easily compared.

Time constants of recovery from inactivation were assessed for I_{Ba} and I_{Ca} at various holding potentials, and are depicted in Fig. 10 with experimental results (Mahajan *et al.*, 2008b). Recovery is faster at more negative E_m, with no differences between I_{Ca} and I_{Ba}.

AP model validation

We assessed the robustness of the model by validating it in more physiological settings against experimental AP-clamp data from isolated ventricular myocytes from rabbit (Yuan *et al.*, 1996; Puglisi *et al.*, 1999; Linz & Meyer, 2000) and guinea pig (Linz & Meyer, 1998). Ca influx via LTCC during an AP differs notably from that evoked by a square voltage pulse (Yuan *et al.*, 1996), and our simulations confirm this (Fig. 11, left *vs*. right). I_{Ca} peaks and inactivates more slowly during an AP (Fig. 11B), but the current integral is larger at the end of the AP command pulse (Fig. 11C). Fig. 12B shows comparable simulated and experimental I_{Ca} (Linz & Meyer, 1998) elicited by APs with different amplitudes (Fig. 12A). I_{Ca} peak decreases as AP amplitude (and upstroke potential) increases. The reduced influx also causes slower inactivation in each case.

The time courses of I_{Ba} and I_{Ca} during an AP are depicted in Fig. 13B. When SR Ca release is prevented, I_{Ca} inactivates more slowly, and the integral of Ca influx through the channel is augmented (Fig. 13C). Furthermore, when addition of BAPTA is simulated, CDI is nearly absent, and I_{Ca} exhibits a prominent plateau and causes a much larger Ca influx. Model predictions agree well with experimental results reported in Fig. 13A-C, right panels (Linz & Meyer, 1998). In Fig. 13B and C, left, I_{Ba} is simulated with either the 7-state or the non-IDI 5-state LTCC model.

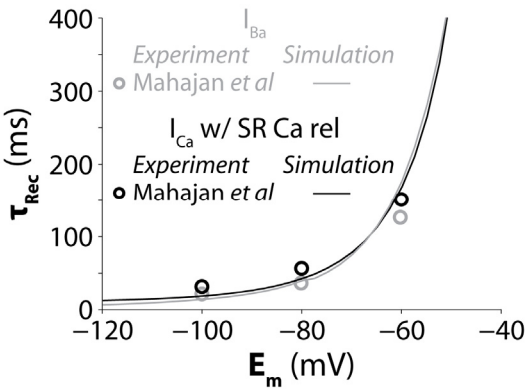

Figure 10. Recovery from inactivation. Experimental (symbols) and simulated (lines) time constants of I_{Ba} and I_{Ca} recovery from inactivation obtained at varying holding potentials. Recovery from inactivation assessed using a 250 ms long voltage-clamp pulse to +10 mV (P1) followed by repolarization to the various holding potentials for a variable time interval and a second pulse to 0 mV (P2). The time constant was estimated by fitting the recovery curve (ratio of the peak P2/P1 currents plotted as a function of recovery interval) to a monoexponential function.

We also validated the comprehensive cellular AP and CaT model. To allow a direct comparison with existing rabbit models, time courses of AP and CaT (Fig. 14A), APD restitution properties (Fig. 14B), APD rate-adaptation (Fig. 14C) after sudden changes in cycle length, and frequency-dependent increase of systolic $[Ca]_i$ and $[Na]_i$ (Fig. 14D) obtained with our model are superimposed to those obtained with the Shannon-Bers (Shannon *et al.*, 2004) and the Weiss group (Mahajan *et al.*, 2008b) AP models as compared in a recent study (Romero *et al.*, 2011). Our model performs well when comparing simulated values of cardiac biomarkers (APD_{90}, APD triangulation, slow time constant of the temporal APD_{90} adaptation to the accelerating rate, and maximal slopes of S1S2 and dynamic restitution curves) to the experimental (Table 3). Alternans were developed in our model at a pacing cycle length ≤180 ms (Fig 14E).

Analysis of inactivation mechanisms and sources of CDI

To estimate the contribution of VDI and CDI to total inactivation and further validate the model, we reproduced the experimental GD-P protocol designed by Linz and Meyer (Linz & Meyer, 1998) and illustrated in Figs. 12B and 13D. This protocol, by interrupting the AP at different times (see Methods), reveals the fraction of channels inactivated during an AP (1-availability; Fig. 12C-E). Fig. 13E-G show the progression of Ca channel inactivation during the AP and how VDI and CDI contribute to it (experiments at top and simulations at bottom).

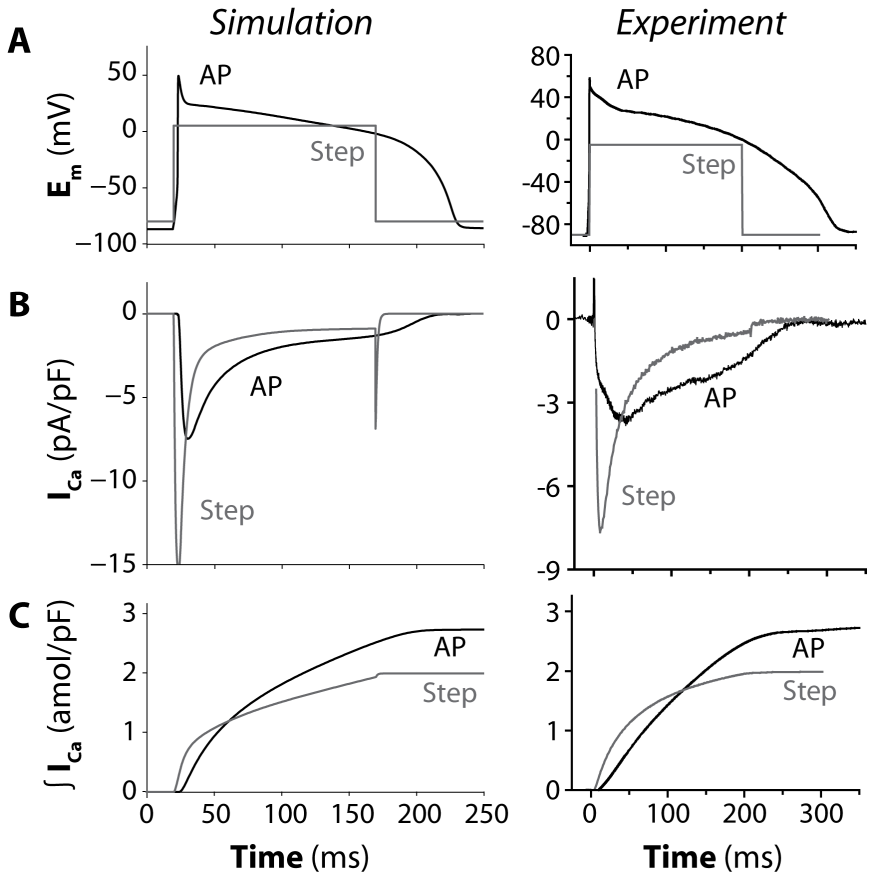

Figure 11. Differences between step and AP-clamp. Simulated (left) and experimental (right) (Yuan *et al.*, 1996) E_m (A), I_{Ca} (B), and running integral of Ca influx via LTCC (C). Simulated voltage step was from -80 mV to 5 mV, and AP waveform was obtained by pacing the virtual cell at 0.33 Hz to steady-state (with normal CaT).

The time course of inactivation (Fig. 13E, lower panel) was assessed using this protocol for simulated I_{Ca} with and without SR Ca release and I_{Ba}. Fig. 13F shows the accumulation of CDI and VDI, estimated assuming that LTCC availability is the product of Ca- and voltage-dependent availability, as in (Linz & Meyer, 1998). The contribution of Ca released from the SR to I_{Ca} inactivation (CDI_{SR}) was calculated as the difference between

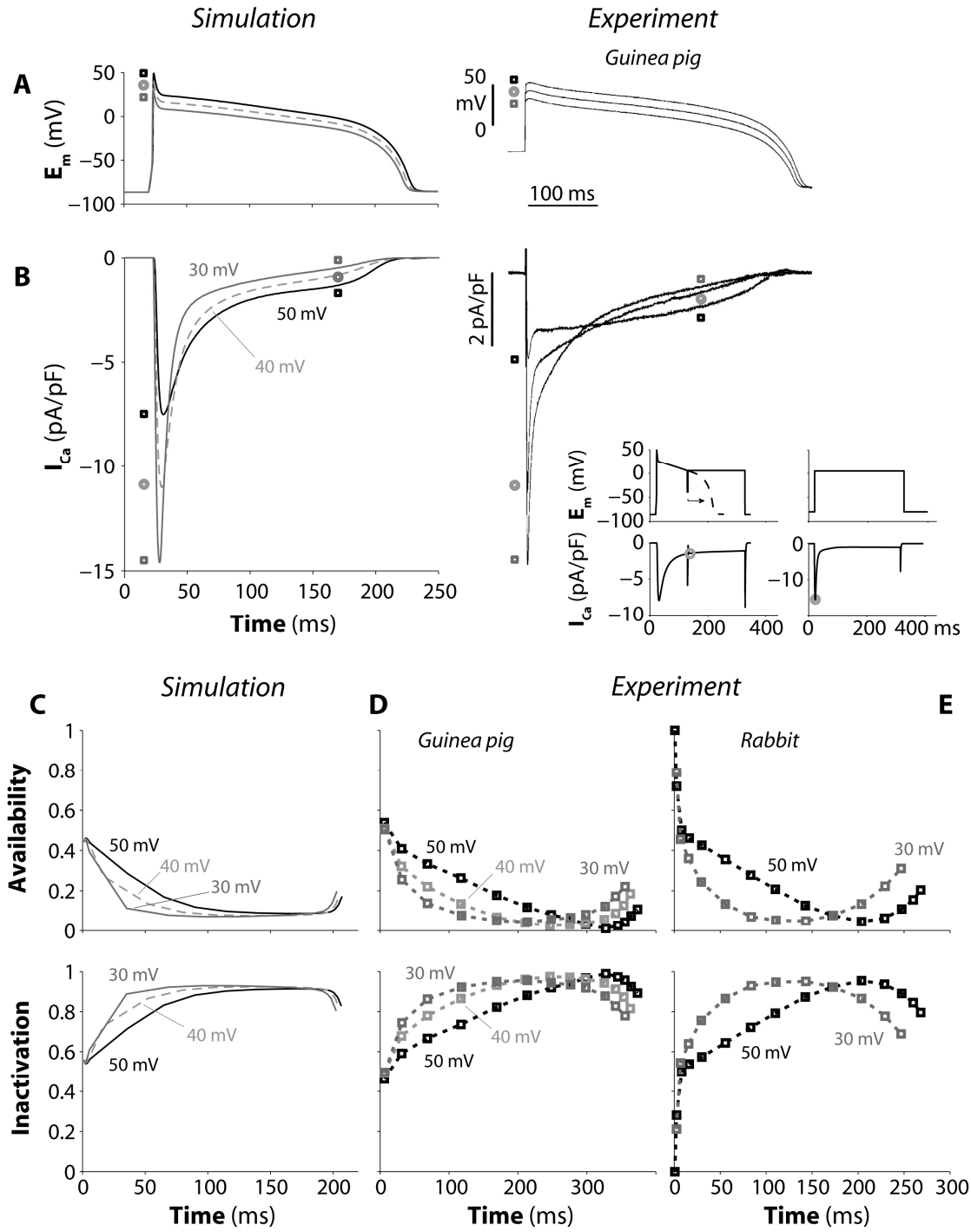

Figure 12. Influence of AP amplitude on I_{Ca} inactivation. Simulated (left) and experimental (right) (Linz & Meyer, 1998) command APs with the same holding value and different amplitude (A) were used to evoke I_{Ca} (B). Simulated (C) and experimental (in guinea pig (Linz & Meyer, 1998) and rabbit (Linz & Meyer, 2000), D and E respectively) time course of current availability (top) and inactivation (bottom) during APs with different amplitudes were obtained with the GD-P protocol depicted in B, inset.

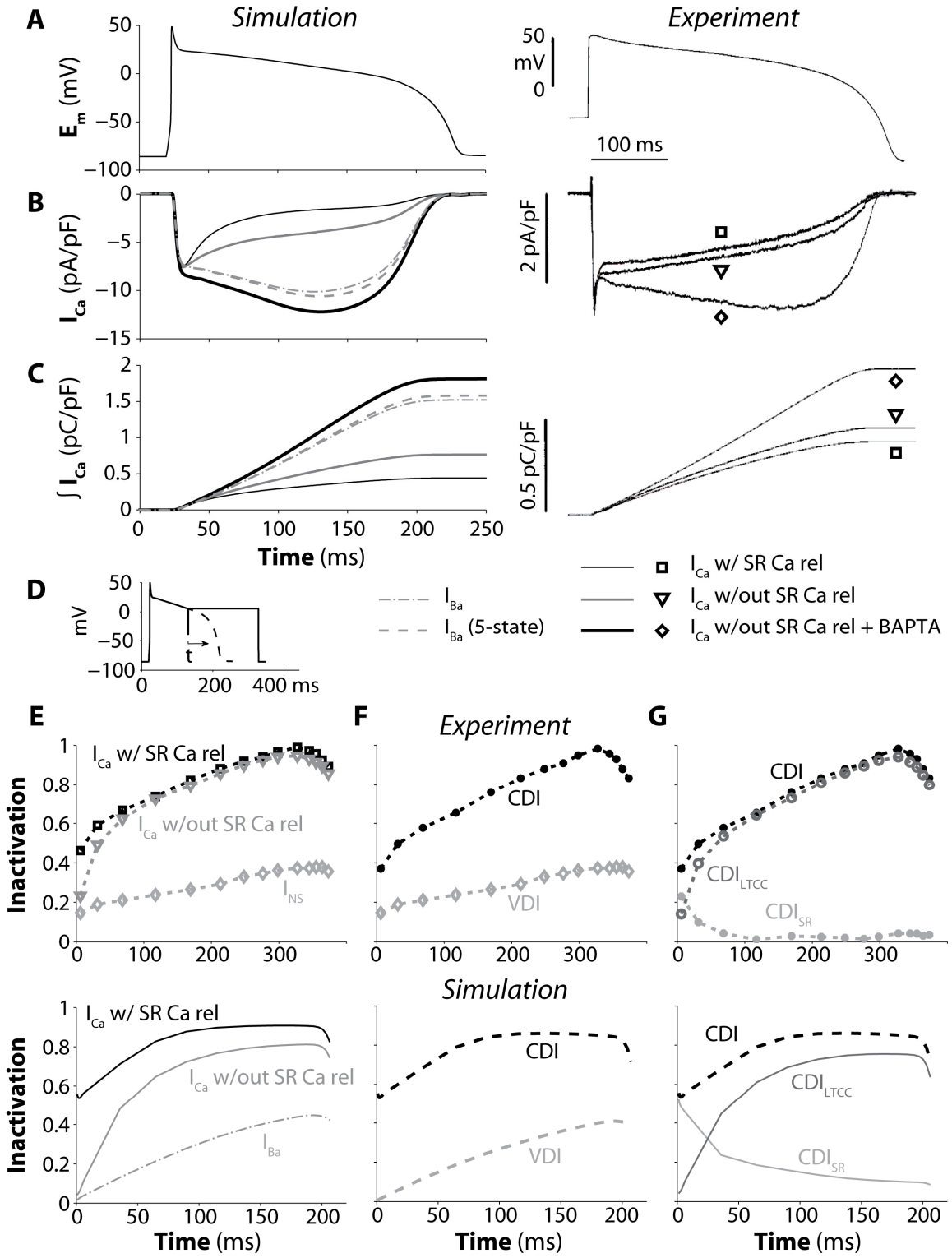

Figure 13. Influence of Ca homeostasis on I_{Ca} during AP-clamp. AP waveform was obtained by pacing the virtual cell at 0.33 Hz to steady-state (with normal CaT). Simulated (left) and experimental (right) (Linz & Meyer, 1998) command AP (A), evoked current (B), and running flux integral (C) with normal CaT, without SR Ca release, and BAPTA. I_{Ba} was also simulated with the baseline model and a reduced 5-state (VDI only) model. Experimental (top) (Linz & Meyer, 1998) and simulated (bottom) time course of current inactivation (E-G) during an AP was obtained with the GD-P protocol depicted in D. E) Inactivation of I_{Ca} with CaT, I_{Ca} without SR Ca release, I_{NS}, and I_{Ba}. F) Experimental and simulated VDI, and CDI. G) Experimental and simulated CDI_{SR} and CDI_{LTCC}.

availabilities measured with and without SR Ca release (Fig. 13G). Finally, the contribution of Ca entry via I_{Ca} to inactivation (CDI_{LTCC}) was calculated by subtracting CDI_{SR} from CDI (Fig. 13G). We infer that SR Ca release accounts for most of CDI during the initial AP phase, whereas Ca through LTCC controls CDI later during the AP. Experimental results (Linz & Meyer, 1998) are shown in the upper panels of Fig. 13E-G. I_{NS} via LTCC was used experimentally to assess VDI, rather than using our 5-state VDI model (Fig. 2B).

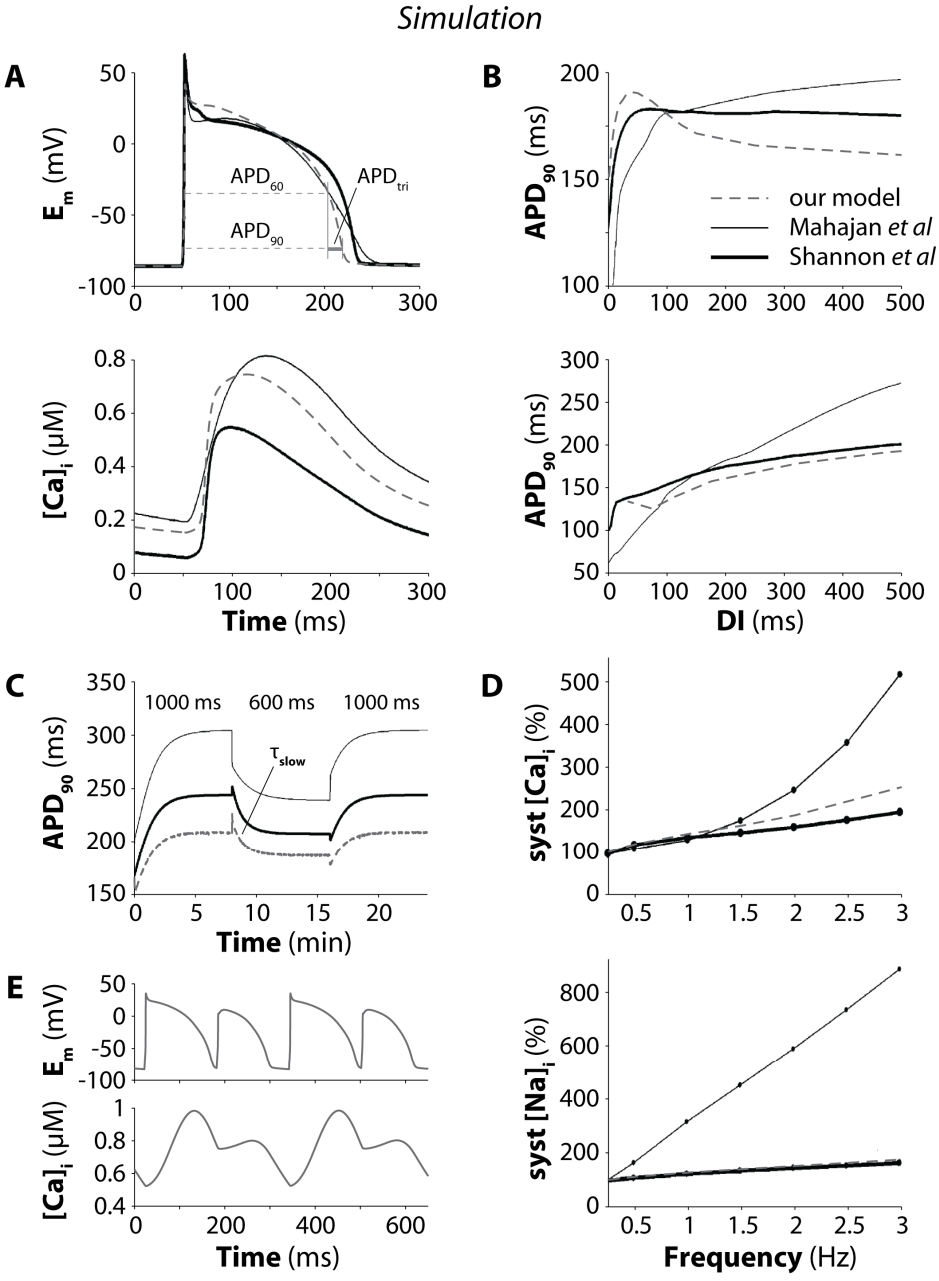

Figure 14. Dynamic properties of AP models. Electrophysiological activity simulated as in (Romero *et al.*, 2011) for Shannon-Bers (thick black line), Mahajan *et al*. (thin black line), and our model (dashed grey): time course of steady-state AP (A, top panel) and CaT (A, bottom) at 2.5 Hz; S1S2 (B, top) and dynamic (B, bottom) APD (to 90% repolarization, APD_{90}) restitution curves; APD rate adaptation (C) after sudden changes in cycle length (indicated), starting from steady-state conditions at 2.5 Hz; steady-state normalized systolic [Ca] (D, top) and [Na] (D, bottom) relative to value at 0.25 Hz as a function of the pacing frequency. E) Steady-state E_m (top) and CaT (bottom) obtained by stimulating our model at 6.25 Hz.

Table 3. Comparison of simulated and experimental biomarkers. APD_{90} is the APD at the 90% of repolarization; APD_{tri} (APD triangulation) is the difference between APD_{90} and APD_{60} (Fig. 14A); τ_{slow} is the slow time constant of the temporal APD_{90} adaptation to the accelerating rate (Fig. 14C); $slope_{max, S1S2}$ and $slope_{max, Dyn}$ are the maximal slopes of S1S2 and dynamic restitution curves (Fig. 14B, respectively top and bottom panels). Experimental range from (Romero *et al.*, 2011).

Biomarker	Simulation			Experimental range
	Shannon *et al.*	Mahajan *et al.*	Our model	
APD_{90} (ms)	177	185	167	120-190
APD_{tri} (ms)	18	37	15	26-32
τ_{slow} (ms)	52	84	41	12-42
$slope_{max, S1S2}$ (-)	3.8	4.3	3.42	3.3-6
$slope_{max, Dyn}$ (-)	4.1	0.96	0.36	1.5-2.5

The importance of SR Ca release for CDI was also highlighted in AP-clamp experiments in rabbit ventricular myocytes at 35°C (Puglisi *et al.*, 1999). Analogous to experiments, I_{Ca} traces evoked by APs subsequent to an initial SR depletion show increasingly faster inactivation (Fig. 15A-B) as the SR is replenished and SR Ca release increases (Fig. 15C). Normalized integrals of I_{Ca} during each pulse reveal that inactivation due to SR Ca release decreases net Ca influx by about 40%, similar to experimental data (Fig. 15D).

Effects of reduced VDI

Changes in the VDI transitions caused a striking reduction in the SSI curve (Fig. 16A), and led to AP prolongation (Fig. 16B). Notably, this reduced VDI did not modify I_{Ca} during the early repolarization and initial plateau phase, but rather during late AP phases 2 and 3 (Fig. 16C). Indeed, VDI monotonically increases during the AP and makes a larger contribution during repolarization (Fig. 13F *vs*. 16E). The time courses of CDI_{SR} and CDI_{LTCC} do not appear appreciably modified by removal of VDI (Fig. 16F).

Effects of reduced CDI

We assessed the effects of impaired CDI on the cardiac AP by simulating the expression of CaM_{1234}, which eliminates CDI of native LTCCs by displacing WT CaM that is otherwise normally prebound to the channels. LTCC inactivation slowed with increasing expression of CaM_{1234} (Fig. 17A-B) (Alseikhan *et al.*, 2002; Mahajan *et al.*, 2008a), which caused significant AP prolongation (Fig. 17C), as reported experimentally (Alseikhan *et al.*, 2002), *e.g.*, larger than that produced by comparable reduction of VDI in Fig. 16.

When 20% of the channels have Ca-insensitive CaM prebound, the model predicts the occurrence of EADs, as shown in Fig. 17D and 18A. We monitored the time courses of LTCC open probability, the opening rate (dO/dt), and contributions to dO/dt of transitions between open and closed states (activation/deactivation) or open and inactivated states (inactivation/recovery) during a control AP (Fig. 19) and during the CaM_{1234}-induced EAD (Fig. 20, left). Insets show enlargement of AP plateau near the EAD takeoff (*i.e.* when dE_m/dt became positive during AP plateau). This phenomenon does not depend on I_{Ca} reactivation

(Figs. 18A-B and 20B-D, left). In fact, LTCC open probability progressively declines (dO/dt is always negative) during the entire AP plateau and EAD (Fig. 20D, left, inset); channels are leaving the open state. Instead, these EADs are likely to be due to enhanced Ca extrusion via inward Na-Ca exchanger (NCX) current (I_{NaCa}, Fig. 17F). This I_{NaCa} is due to enhanced SR Ca loading and spontaneous SR Ca release (Fig. 17J) and elevated sub-sarcolemmal [Ca] ($[Ca]_{SL}$, Fig. 17H). We tested the role of I_{NaCa} by reducing NCX density instantaneously during the arrhythmogenic AP just before EAD takeoff. When I_{NaCa} was reduced by 10%, EAD amplitude was reduced (Fig. 17D and F, inset), whereas a 30% NCX reduction completely eliminated the EAD (Fig. 17D and F, inset).

As CDI reduction increased to 40% APD was further prolonged, but no EADs occurred (Fig.17C). Our explanation for the disappearance of EADs is that as CDI decreases the AP plateau potential becomes more depolarized, thus opposing inward I_{NaCa} (the more depolarized E_m the less inward I_{NaCa}), which is not large enough to cause membrane afterdepolarization.

When the fraction of Ca-CaM insensitive channels was increased to 50%, the AP prolonged further (Fig. 17L) due to the increased depolarizing I_{Ca} (Fig. 17M), which also further loaded the SR with Ca (Fig. 17R). The high $[Ca]_{SR}$ causes a large spontaneous Ca release (Fig. 17R-S) which activates a large inward I_{NaCa} (Fig. 17N), sufficient to cause a

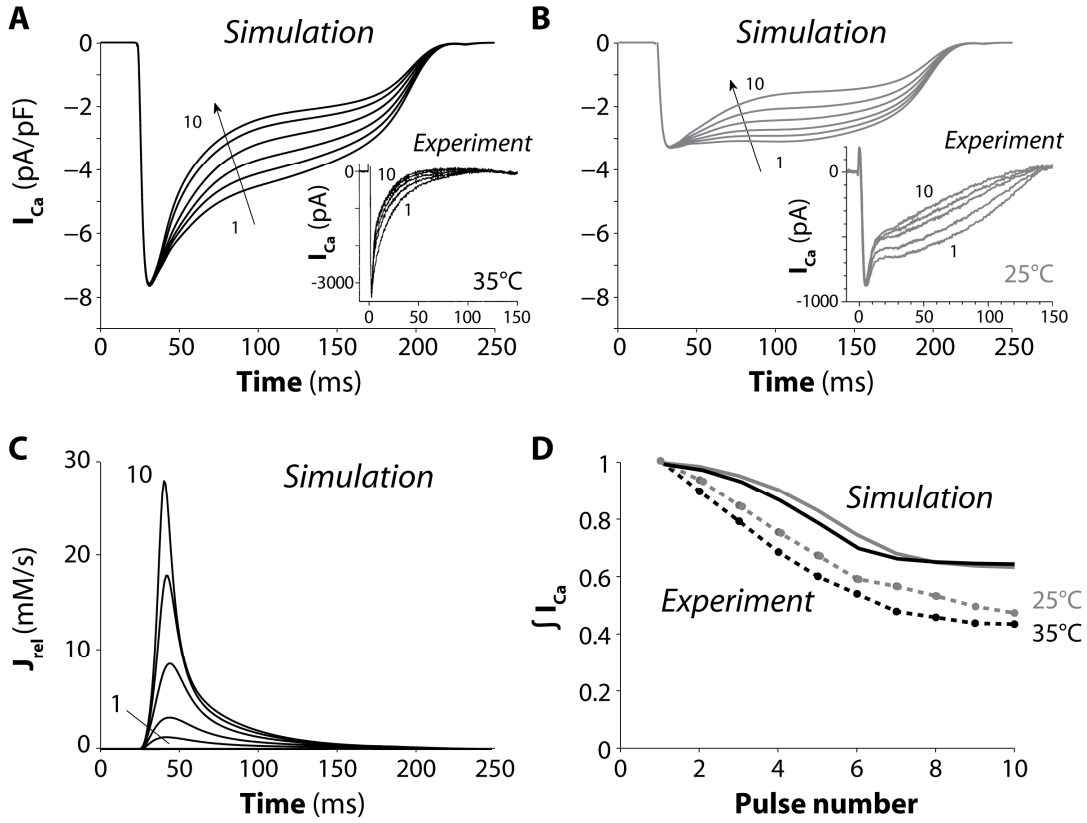

Figure 15. Influence of SR Ca release on I_{Ca} inactivation. I_{Ca} traces (A) and SR Ca release fluxes (C) elicited by a train of 10 APs (as in Fig. 11A) after SR depletion at physiological temperature. B) Data at 25°C were simulated by simply decreasing LTCC permeability by 50% (to show the effect of reduced Ca influx) rather than reparameterizing the whole AP model at room temperature. Insets show experimental data from (Puglisi *et al.*, 1999). D) Normalized simulated (solid lines) and experimental (symbols) (Puglisi *et al.*, 1999) Ca influx integrals at every pulse (black 35°C, grey 25°C).

delayed afterdepolarization (DAD) and triggered AP (Fig. 17L). A second DAD occurs after the first triggered AP, but the spontaneous SR Ca release is slightly smaller, and fails to trigger an AP.

Effects of I_{Kr} and I_{Ks} block

We also examined AP prolongation due to complete block of both rapid and slow components of delayed-rectifier K current (I_{Kr} and I_{Ks}, Fig. 18E). As with the CaM_{1234}-modified AP, we monitored the time courses of LTCC open probability and state transitions (Fig. 20B-D, right). In contrast with CaM_{1234} expression, under I_{Kr} and I_{Ks} block we clearly detected LTCC reactivation during EAD takeoff. In this case dO/dt turned positive (Fig. 20D, right, inset), indicating that more channels entered the open state (unlike the CaM_{1234} case). This I_{Ca} reactivation during the EAD was due to reopening from the closed state C_1: while the transition between inactivated and open states (Fig. 20D, right, inset) moved negative (indicating inactivation did increase, *i.e.* negative dO/dt), that between closed and open states moved more strongly positive (indicating a more than compensatory reactivation, resulting in dO/dt>0). We looked also at the time courses of occupancy of the other states before EAD takeoff (Fig 21). While the occupancies of VDI states monotonically increased

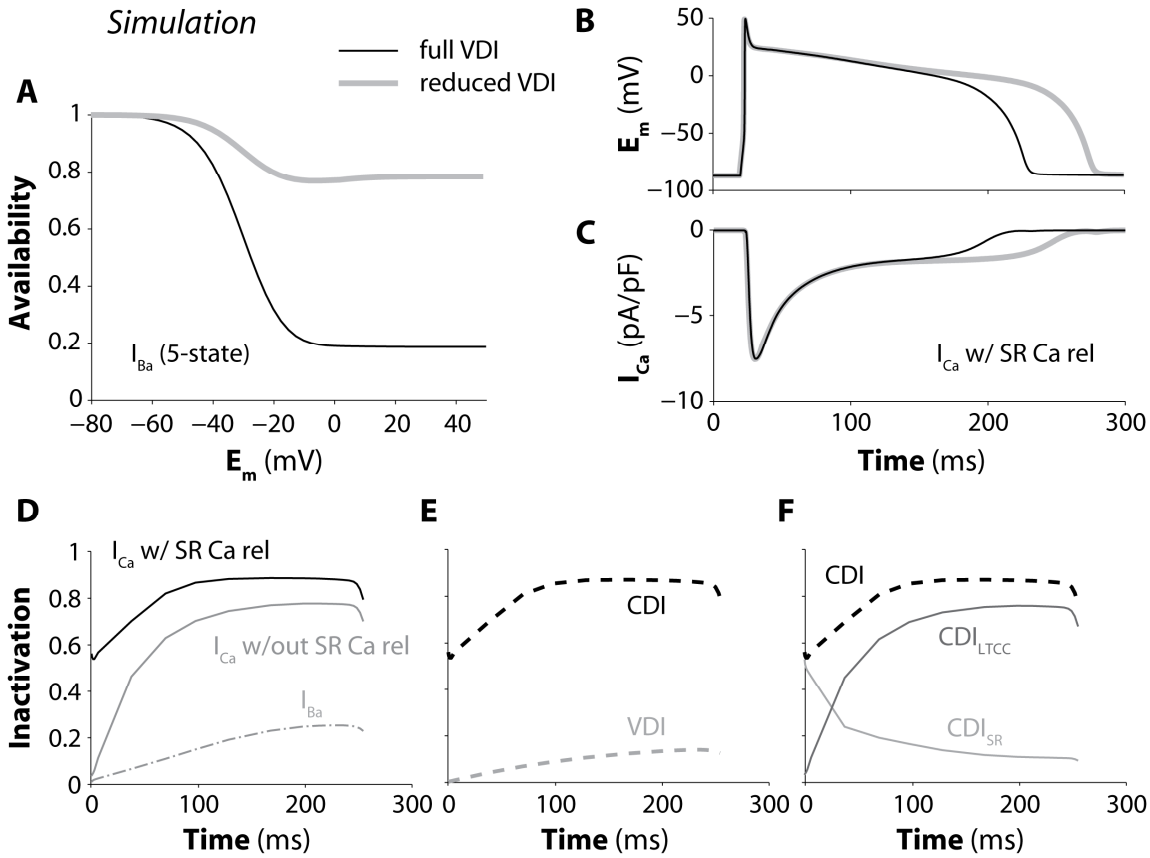

Figure 16. Effects of reduced VDI. A) Quasi-SSI curves depict the available I_{Ba} (5-state model) after 1000 ms-long inactivation pre-pulses to the indicated voltages in control and reduced VDI conditions. Action potentials (B) and I_{Ca} (C) with normal CaT in control and reduced VDI conditions. D) Simulated time course of current inactivation during an AP with reduced VDI for I_{Ca} with CaT, I_{Ca} without SR Ca release, and I_{Ba}. E) Simulated VDI and CDI. F) Simulated CDI, CDI_{SR} and CDI_{LTCC}.

(Fig. 21F), we found a decrease in CDI states occupancies (Fig. 21E). This recovery of LTCCs from CDI caused the enhancement of C_1 occupancy (Fig. 21C and G).

I_{Ca} inactivation kinetics during EADs

We next evaluated I_{Ca} inactivation during APs that showed EADs. We used GD-P protocols based on the two types of exemplar APs described above, obtained at 0.33 Hz, one with 20% expression of CaM_{1234} (Fig. 18A) and the other with complete block of I_{Kr} and I_{Ks} (Fig. 18E).

As experimentally observed (January & Riddle, 1989), in our simulations EAD amplitude inversely correlated with takeoff potential (the more negative the takeoff potential the larger the EAD amplitude, as indicated in Fig. 18A and E). I_{Ca} decayed smoothly throughout the CaM_{1234}-induced EAD (Fig. 18B), whereas it exhibited a notch upon EAD initiation (Fig. 18F) with inhibition of K currents. Notably, a similar hump in I_{Ca} was detected experimentally (Yamada *et al.*, 2008) during the same type of protocol in guinea pig ventricular myocytes (Fig. 18I and J). I_{Ca} inactivation increased monotonically during the CaM_{1234}-induced EAD (Fig. 18C), and so did its E_m- and Ca-dependent components (Fig. 18C and D respectively). On the other hand, with the EAD induced by K current block, I_{Ca} inactivation increased during the AP plateau, decreased slightly just before EAD takeoff, and increased again thereafter (Fig. 18G), as observed experimentally (Fig. 18K). In both simulations and experiments (Yamada *et al.*, 2008), VDI did not display any clear notch (Fig. 18G and K), whereas CDI showed a notch before EAD takeoff (Fig. 18H and L). Both CDI_{LTCC} and CDI_{SR} exhibited a hump prior to EAD initiation (Fig. 18H). This confirmed the recovery of LTCCs from CDI before EAD takeoff previously described.

DISCUSSION

In the present study we developed improved LTCC and SR Ca release models within the framework of the rabbit ventricular ECC model. Our main goal was to dissect the relative importance of VDI and CDI to total I_{Ca} inactivation during normal and abnormally prolonged APs. To differentiate VDI from CDI of macroscopic I_{Ca}, substitution of Ca with other charge carriers (*e.g.*, Ba, (Zhong *et al.*, 1997; Sako *et al.*, 1998; Sun *et al.*, 2000; Sonoda & Ochi, 2001; Mahajan *et al.*, 2008b) or Na and Cs (Hadley & Hume, 1987; Hryshko & Bers, 1992; Yuan *et al.*, 1996)) has been widely used. In these studies, inactivation of I_{Ba} or I_{NS} has been assumed to reflect purely VDI. We sought to whether I_{NS} or I_{Ba} inactivation are a true measure of VDI for I_{Ca} and we found that I_{NS} inactivation at physiological temperature is faster (*vs*. I_{Ca}) and complete, perhaps reflecting some intrinsic difference *vs*. VDI occurring during I_{Ca} or I_{Ba}. Moreover, the main limitation to the use of I_{Ba} as a measure of VDI is its ability to modestly mimic CDI. Thus, we concluded that both approaches lead to an overestimation of VDI, and we constrained our LTCC model parameters by accounting for reduced, but not eliminated, IDI when Ba is the charge carrier.

Inactivation of I_{NS} and I_{Ba} through the LTCC

I_{NS} inactivates incompletely at room temperature (Hadley & Hume, 1987; Sun *et al.*, 1997; Sun *et al.*, 2000), but when the temperature was raised to 30°C the extent of inactivation was greater (Hryshko & Bers, 1992). Inactivation was even more complete at physiological

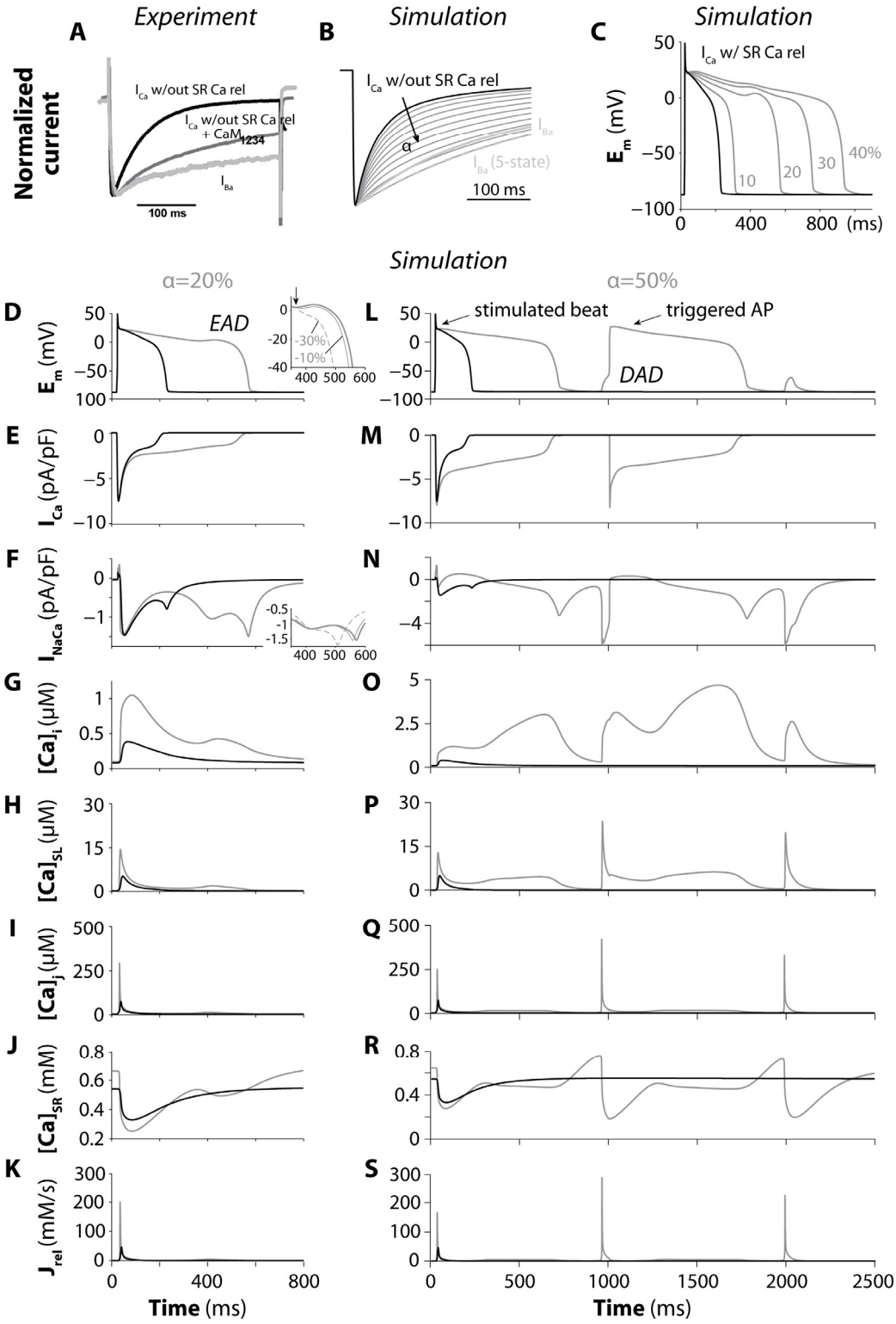

Figure 17. Effects of Ca-insensitive CaM overexpression. A) Experimental (Mahajan *et al.*, 2008a) normalized currents evoked by a voltage step from -80 mV to +10 mV for I_{Ca} without SR Ca release (WT and CaM_{1234}) and I_{Ba}. B) Simulated normalized I_{Ca} without SR Ca release (baseline, and with various degrees of impaired CDI). I_{Ba} traces are shown with the baseline model and a reduced 5-state model. C) Simulated AP obtained when pacing the digital myocyte at a basic cycle length of 3 s in baseline conditions and with various degrees (indicated) of impaired CDI. D-S) Simulated AP, I_{Ca}, I_{NaCa}, CaT, [Ca] in sub-sarcolemmal and cleft compartments, free SR Ca content and SR Ca release obtained when pacing the digital myocyte at a basic cycle length of 3 s in baseline conditions and with reduced CDI (20% reduction in D-K, and 50% in L-S). Insets in panels D and F show results obtained for the mutant condition by reducing instantaneously NCX density by 10% and 30%.

temperature (Fig. 4C *vs*. 4D). Mitarai and colleagues (Mitarai *et al.*, 2000) also showed strong VDI of INS at physiological temperature (Fig. 5), and rescaling available experimental data to 37°C gave comparable results. They explained some previous work reporting slower I_{NS} decay by suggesting that β-adrenergic stimulation could slow LTCC inactivation (as shown previously in (Yuan & Bers, 1995)). Indeed, when measuring I_{NS} in the presence of extracellular divalent cations (which partially block I_{NS}), isoproterenol was added to compensate for I_{NS} reduction (Matsuda, 1986; Linz & Meyer, 1998). However, since divalent cations can strongly block I_{NS}, it is debatable whether intrinsic I_{NS} gating can be measured in the presence of divalent cations in the bathing solution.

There are two tacit assumptions usually made when using I_{NS} as an experimental model to study I_{Ca} VDI: 1) the absence of IDI, which seems appropriate, and was recently confirmed (Brunet *et al.*, 2009); 2) VDI of I_{NS}, I_{Ba} and I_{Ca} are the same process, which we now think may not be the case.

The substitution of Ba ions for Ca has been widely used to separate VDI from CDI of the macroscopic LTCC currents, and this is pragmatic because Ba produces only modest IDI (Ferreira *et al.*, 1997; Brunet *et al.*, 2009) and probably has similar (but not identical) binding properties to Ca in the pore. However, I_{Ba} inactivation depends on Ba flux, and it seems clear now that Ba can recapitulate a weak version of CDI. Ba is known to complex with CaM and activate interaction with CaM targets (Yamazaki *et al.*, 1996; Ozawa *et al.*, 1999), but its apparent affinity in other systems has typically been ≥100-fold lower than for Ca. While our change in rate constants that produces appropriate I_{Ba} IDI could be construed to represent only a ~10-fold reduction in affinity, this lower value should not be taken to imply an actual affinity difference in the classical biochemical sense.

To account for the moderate Ba-dependent inactivation, we have extended a previously published LTCC mathematical model of VDI and CDI into an ECC model (Mahajan *et al.*, 2008b), and assessed whether and how experimental I_{Ba} inactivation results could be recapitulated by modifying CDI to account for Ba-dependent inactivation. We found that making 10-fold reductions in the Ca-dependent transition rates (in Fig 2) resulted in appropriate Ba-dependent I_{Ba} inactivation. Sun and colleagues (Sun *et al.*, 2000) similarly fit their data of I_{Ba} by decreasing the Ba association constant to 10% of that of Ca. Thus their model suggested a smaller reduction of Ba affinity *vs*. Ca compared to another study (Ferreira *et al.*, 1997), where the affinity for the inactivation site was reckoned to be ~100 times lower for Ba than Ca for $Ca_V1.2$ using a heterologous expression system. Reasons that the relatively modest 10-fold reduction in Ba- *vs*. Ca-dependent inactivation (*vs*. ≥100-fold expected for CaM binding) could have to do with: 1) the way CaM is prebound to the LTCC, 2) potentially weaker local Ba *vs*. Ca buffering, 3) higher single channel conductance for Ba, 4) dynamic considerations during current flow (Ba may equilibrate faster than Ca). In any event, given the Ba-dependent inactivation implemented here, one could derive a slower VDI model, which should be a more faithful representation of purely VDI during I_{Ca}. This may be an important distinction when one seeks to dissect the relative roles of Ca and E_m in mediating normal function and pathophysiology (*e.g.*, arrhythmogenesis).

Some studies in guinea pig ventricular myocytes showed similar inactivation of Ba, Sr, and Na currents (Findlay, 2002b), at least at room temperature. Analogously, Sun and colleagues (Sun *et al.*, 2000) also reported similar inactivation τ for I_{NS} and I_{Ba} in rat cardiomyocytes (at room temperature), whereas I_{NS} (and I_{Sr}) inactivated more slowly than I_{Ba}

in human atrial cells at 23°C (Sun *et al.*, 1997). Mahajan *et al*. measured I_{Ba} (and I_{Ca}) in rabbit cardiomyocytes at physiological temperature and reported that I_{Ba} inactivates incompletely with a monoexponential decay with τ ~150 ms (with little E_m-dependence) in the absence of β-adrenergic stimulation (Mahajan *et al.*, 2008b). Here, we found that I_{NS} inactivation is accelerated as temperature increases (especially at negative E_m, where I_{NS} inactivation is slowest). Thus, we find that I_{NS} can inactivate more rapidly and completely than I_{Ba}, especially at physiological temperature (Fig. 5), suggesting that VDI that occurs during I_{Ba} (or

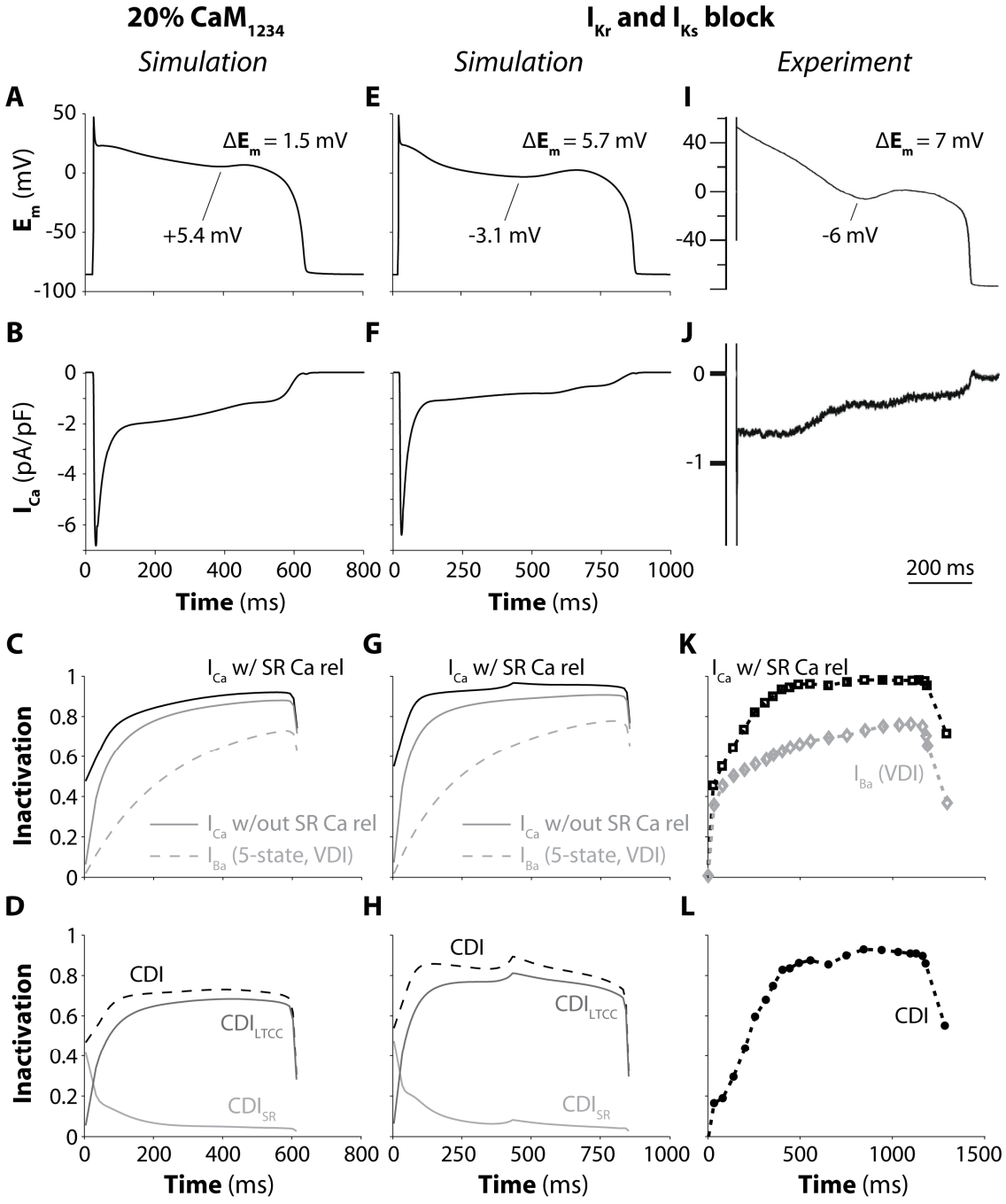

Figure 18. I_{Ca} inactivation kinetics during phase 2 EADs. Kinetics of I_{Ca} (B, F and J) during AP-clamp with EAD-like stimuli (A, E and I) were assessed with the GD-P protocol. Total I_{Ca} (with and without release) inactivation (C, G and K), VDI, CDI (D, H and L), and CDI_{SR} and CDI_{LTCC} were computed with 20% expression of CaM_{1234} (A-D), and block of I_{Kr} and I_{Ks} (E-H, simulations *vs*. experiments (Yamada *et al.*, 2008), I-L).

I_{Ca}) must differ intrinsically from VDI during I_{NS}. During I_{Ca} and I_{Ba} flow, it is thought that the channel is essentially always occupied by at least one divalent cation occupying the pore (Yang *et al.*, 1993), and this binding prevents monovalent permeation. We suggest that in the absence of divalent cation occupancy (during I_{NS}), VDI of the LTCC is fundamentally different, exhibiting steeper E_m-dependence, which is faster than when divalent cations occupy the channel pore. This raises new questions of whether fast inactivation of I_{NS} is due to the absence of divalent cations that bind in the channel pore, or whether inactivation of inward I_{NS} differs from outward I_{NS} (*e.g.*, due to the intracellular milieu).

Inactivation of I_{Ca} during normal and abnormal AP repolarization

In the first part of the study we found that neither I_{Ba} nor I_{NS} reflect pure VDI for I_{Ca}. Our modeling results predicted a detectable Ba-dependent inactivation (*i.e.* bell-shaped dependence on E_m) when apparent Ba affinity for CaM is about one tenth than that of Ca. Nevertheless, if intracellular Ba accumulation is avoided (and if I_{Ba} amplitude is kept small), I_{Ba} is probably a better VDI model for I_{Ca} than is I_{NS}. Thus, we integrated the Markov model studied (Mahajan *et al.*, 2008b) into the framework of the Shannon-Bers model of rabbit AP

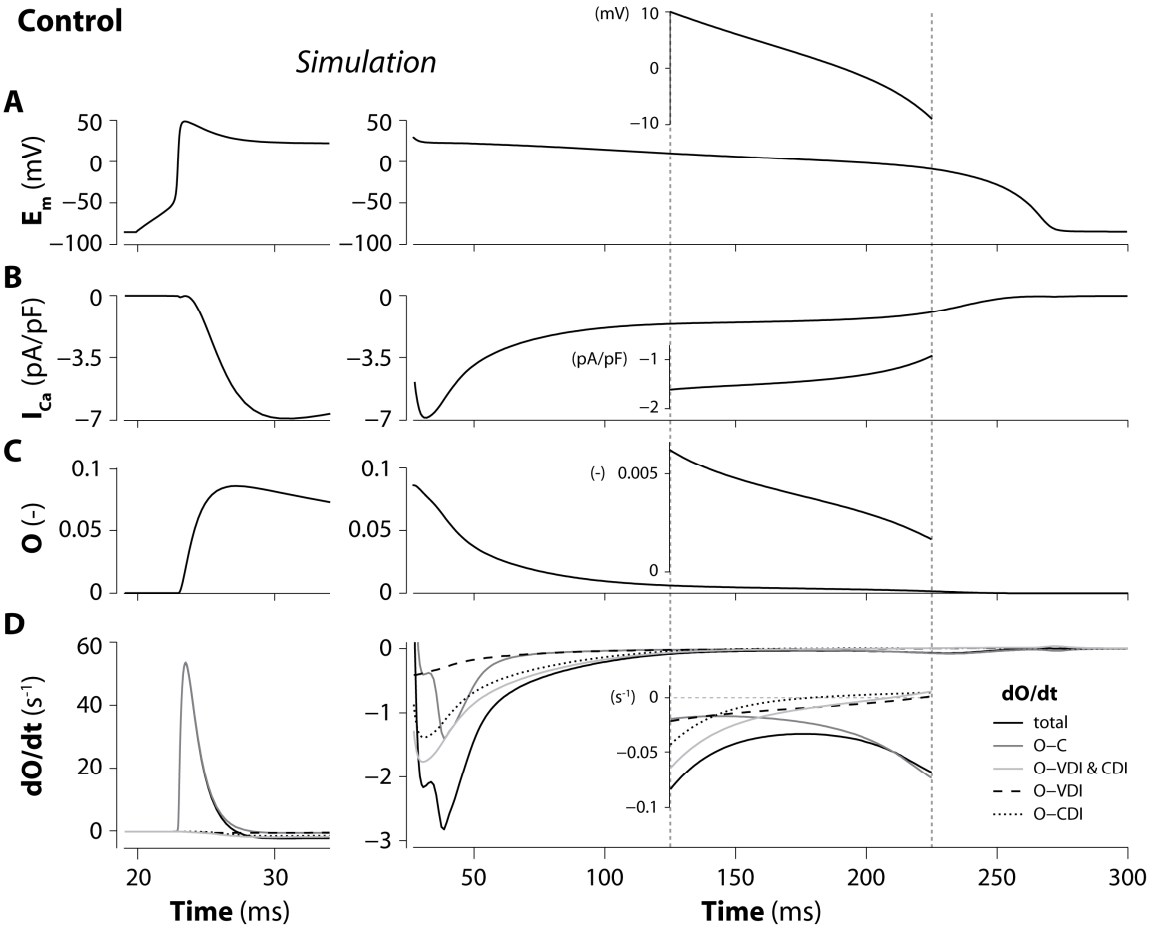

Figure 19. Insights into LTCC dynamics during normal repolarization. Time course of E_m (A), I_{Ca} (B), LTCC open probability (C) and its rate of changes (D), and contributions to dO/dt of channel transitions between Open and Closed (O-C), Open and CD-Inactivated (O-CDI), Open and VD-Inactivated (O-VDI), and Open and Inactivated (O-VDI & CDI) during a control AP. Insets show the final portion of AP plateau (*x* axis limits are indicated with dotted lines in the main panels).

(Shannon *et al.*, 2004) and we constrained LTCC model parameters by accounting for reduced, but not eliminated, IDI when Ba is the charge carrier, and adopted the reduced I_{Ba} model (5 lower states in Fig. 2B) to represent pure VDI. Moreover, the formulation of SR Ca release was modified to reproduce high ECC gain at negative E_m.

The AP model developed reproduces faithfully experimental properties of ventricular myocytes, including: 1) the higher ECC gain at negative E_m; 2) the kinetics of LTCC inactivation (measured with both voltage steps and AP-clamp) under different Ca homeostasis conditions and during EADs; 3) the SR Ca release contribution to I_{Ca} inactivation during an AP; 4) the effects of Ca-insensitive CaM expression; 5) the effects of delayed-rectifier K current inhibition. We used this improved model: 1) to predict the effects of removal of VDI, 2) to study arrhythmogenic mechanisms in the presence of impaired CDI, and 3) to assess the involvement of I_{Ca} in EADs.

A recent study (Romero *et al.*, 2011) investigated the differences between the Shannon-Bers and the Mahajan *et al*. models of the rabbit ventricular AP, and showed that the

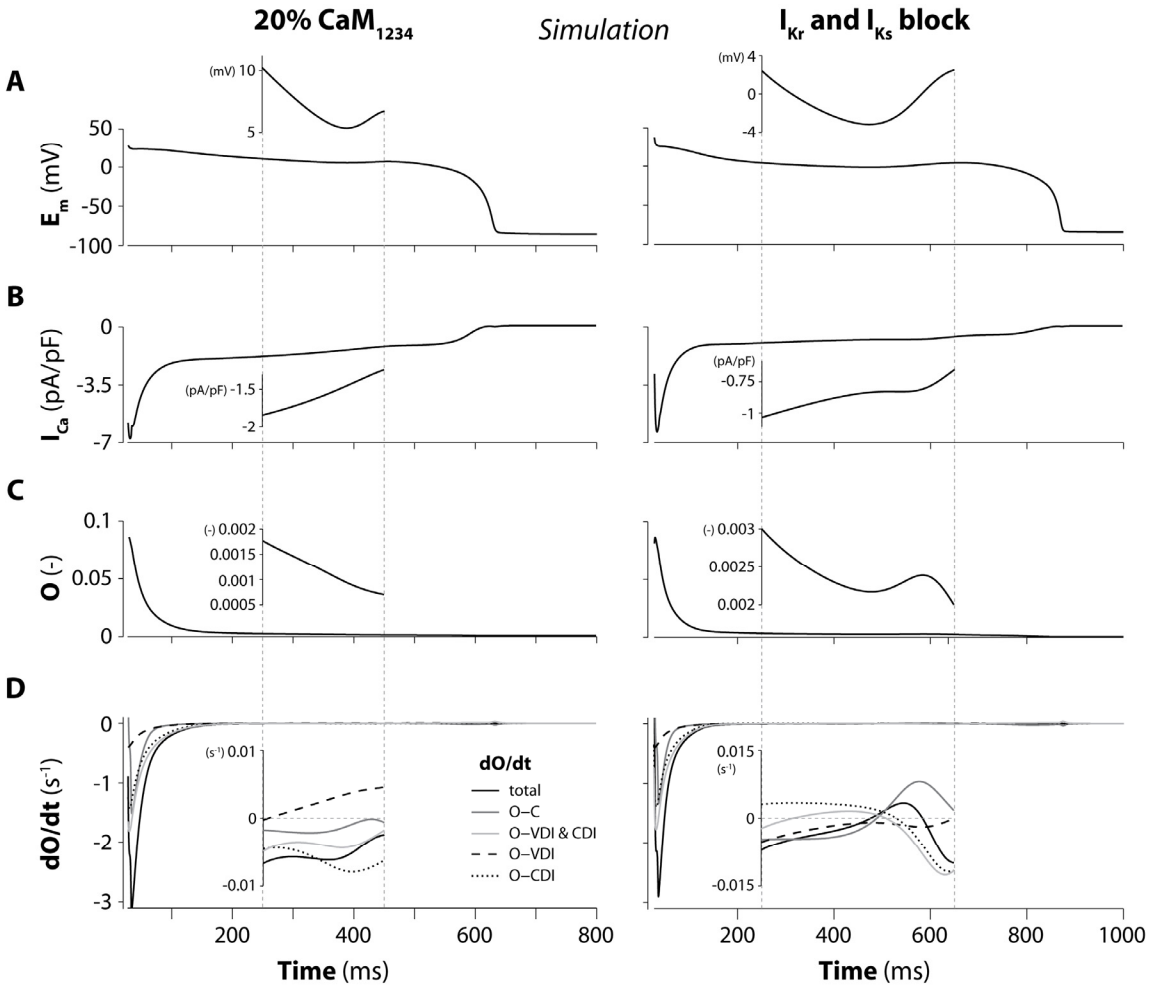

Figure 20. Insights into LTCC dynamics during abnormal repolarization. Time course of E_m (A), I_{Ca} (B), LTCC open probability (C) and its rate of changes (D), and contributions to dO/dt of channel transitions between Open and Closed (O-C), Open and CD-Inactivated (O-CDI), Open and VD-Inactivated (O-VDI), and Open and Inactivated (O-VDI & CDI) during an EAD caused by either CaM_{1234} overexpression (left) or K current blockade (right). Insets show the time window corresponding to EAD takeoff (*x* axis limits are indicated with dotted lines in the main panels).

former performs better at slow rates, the latter at fast rates. We conducted a model evaluation taking into consideration frequency-dependency mechanisms, and showed that steady-state APD and Ca rate dependence (Fig. 14) are similar to those predicted by the parent Shannon-Bers model, in good agreement with experimental data. Although we did not perform a systematic sensitivity analysis, we also expect the ionic mechanisms modulating electrophysiological properties to be similar.

We simulated the GD-P protocol to quantify the contributions of CDI and VDI to total inactivation, and to study the importance of different Ca sources involved in this process (Fig. 13D-G), as in (Linz & Meyer, 1998). We found that I_{Ca} inactivation during an AP is predominantly CDI, which is mostly controlled by SR Ca release during the initial AP phase, but mainly by Ca entering through LTCCs for the remaining part. Linz and Meyer showed similar results in guinea pig cells, although they estimated a smaller contribution of the SR to CDI. Discrepancies between simulated and experimental results may be explained by the authors' choice of measuring I_{NS} to assess pure VDI, since we have shown this assumption leads to overestimation of VDI. Furthermore, there may be differences in LTCC control by Ca in guinea pig *vs*. rabbit myocytes. In fact, we found that I_{Ca} inactivation due to SR Ca release decreases net Ca influx by about 40%, which is just a little less than that which Puglisi and colleagues (Puglisi *et al.*, 1999) showed in rabbit myocytes (Fig. 15).

We based our analysis of CDI and VDI on the classic Hodgkin and Huxley formulation, where the activation and inactivation gating parameters do not represent specific kinetic states of ion channels, are independent, and their product modulates the current (as I_{Ca} in the original Shannon-Bers model, inherited from the Luo-Rudy model (Luo & Rudy, 1994a)). However, the structure of the Markov model here adopted (Mahajan *et al.*, 2008b) allowed us to discriminate the contributions of CDI and VDI by monitoring transitions from the open state to closed and inactivated states (Figs. 19 and 20), as further discussed below.

Several computational studies have acknowledged the importance of developing a detailed kinetic model of LTCC (Imredy & Yue, 1994; Jafri *et al.*, 1998; Sun *et al.*, 2000; Findlay, 2002b; Findlay, 2002a; Faber *et al.*, 2007; Mahajan *et al.*, 2008b; Hashambhoy *et al.*, 2009), due to its fundamental role in ECC in cardiac myocytes (Bers, 2001). Imredy and Yue first introduced a Ca-dependent mode ("Ca mode") to separate CDI and VDI in a rat LTCC model (Imredy & Yue, 1994), which was extended by Jafri and colleagues with two mirroring "normal" and a "Ca" gating mode structures (Jafri *et al.*, 1998). Faber *et al*. conserved the 2-mode "mirror" structure with a more complex description of the inactivation pathways (Faber *et al.*, 2007), whereas the Weiss group proposed the minimal Markov LTCC formulation that is extended in the present paper (Mahajan *et al.*, 2008b). The latter models were accompanied by improved formulations of SR Ca release and integrated into existing AP models (respectively, guinea pig (Luo & Rudy, 1994a) and rabbit (Shannon *et al.*, 2004)). In both models I_{Ba} was used for fitting of VDI. Faber *et al*. and Mahajan *et al*. found that CDI plays a greater role at negative E_m during voltage pulses, due to higher ECC gain. In fact, the Weiss group indicated that CDI_{SR} is more important at negative voltages, while Ca entering the cell dominates CDI at positive E_m (Mahajan *et al.*, 2008b). As for the time course of inactivation, the Rudy group reported an early dominance of SR Ca release in controlling CDI, and a late dominance of sarcolemmal Ca influx, in agreement with our findings with AP-clamp (Faber *et al.*, 2007).

The need for a faithful characterization of the roles of VDI and CDI has been underlined by experimental studies showing the deleterious effects of inhibiting one of the two mechanisms. The Yue group showed the effects of CaM_{1234} expression, which inhibits CDI and produces dramatic AP prolongation (Alseikhan *et al.*, 2002), whereas the Keating group showed the effects of the G406R mutation that removes VDI and is linked to the Timothy syndrome (Splawski *et al.*, 2004). The effects of Timothy syndrome have been investigated in simulation studies (Faber *et al.*, 2007; Zhu & Clancy, 2007; Thiel *et al.*, 2008; Sung *et al.*, 2010). The notion that gene mutations linked to disease may interfere both with VDI and CDI is intriguing (Yarotskyy *et al.*, 2009), although not yet fully understood. Also, shifts in VDI could alter intracellular Ca handling and signaling, which could in turn contribute to the Timothy syndrome phenotype (Thiel *et al.*, 2008). In this study, removing VDI, while retaining CDI, caused AP prolongation (Fig 16). Notably, when simulating the expression of CaM_{1234}, which removes CDI without affecting VDI (Alseikhan *et al.*, 2002), we predicted a much more marked APD prolongation (Fig. 17), confirming previously observed experimental (Alseikhan *et al.*, 2002) and simulation (Mahajan *et al.*, 2008a) results.

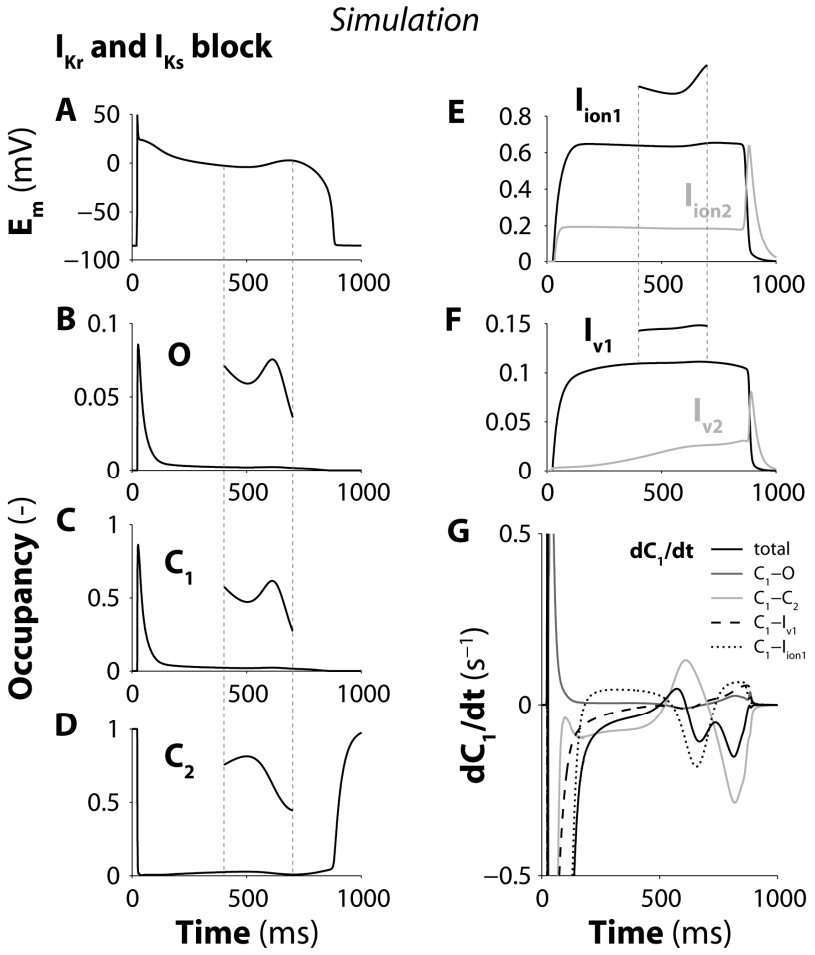

Figure 21. Insights into LTCC dynamics during EAD induced by K currents block. Time course of E_m (A) and occupancy of the LTCC Markov model states (B-F) during an EAD caused by K current blockade. Insets show the time window corresponding to EAD takeoff (*x* axis limits are indicated in the main panels). Panel G shows the rate of change of C_1 occupancy (dC_1/dt), and contributions to dC_1/dt of channel transitions between C_1 and Open (C_1-O), C_1 and C_2 (C_1-C_2), C_1 and VD-Inactivated (C_1-I_{v1}), and C_1 and CD-Inactivated (C_1-I_{ion1}).

We predicted the occurrence of EADs when CDI was reduced, or with further CDI reduction, DADs. The latter occurred when residual CDI was small enough so that added Ca influx caused SR Ca overload and spontaneous release, with consequent activation of enough transient inward NCX current to depolarize the membrane beyond threshold (Priori & Corr, 1990). With a smaller reduction in CDI, not sufficient to harmfully overload the cell, EADs occurred during the AP plateau (phase 2). Depolarization during phase 2 EADs has been attributed to reactivation of I_{Ca} (January & Riddle, 1989; Luo & Rudy, 1994b; Zeng & Rudy, 1995; Yamada *et al.*, 2008). However, in our simulation of CaM_{1234} overexpression, I_{Ca} did not reactivate, but rather continued to inactivate (Fig. 20B-D, left). NCX is typically considered responsible for EADs occurring in AP phase 3 (Luo & Rudy, 1994b; Milberg *et al.*, 2008), where the more negative E_m and increased $[Ca]_i$ due to spontaneous Ca release both favor inward exchange current. Here, we predicted that changes in Ca cycling due to reduced CDI caused greater Ca extrusion, spontaneous SR Ca release (relying on the modified description of RyR gating), and sufficient inward NCX current to cause frank depolarization (Fig. 17). In support of this, when reduced NCX activity was imposed in the simulation, the EAD disappeared (Fig. 17D and F, insets). Indeed, Priori and Corr proposed that EADs and DADs might share the same mechanism (Priori & Corr, 1990), with NCX-mediated inward current being involved also in the genesis of EADs, as proposed for example in cardiac hypertrophy (Sipido *et al.*, 2000).

Phase 2 EADs most typically occur when repolarization is prolonged due to alterations in K or Na currents. We obtained a phase 2 EAD due to I_{Ca} reactivation by blocking I_{Kr} and I_{Ks} (Fig. 18), and used this AP waveform to analyze the kinetics of I_{Ca} during abnormal repolarization, as done experimentally by (Yamada *et al.*, 2008). They have suggested that EADs occur because I_{Ca} fails to completely deactivate, as opposed to significantly recovering from CDI, but our simulations highlighted the importance of recovery from CDI. EADs we obtained with I_{Kr} and I_{Ks} blocked were driven by LTCCs reactivating from the closed state C_1 (E_m-independent transition, Fig. 2B) and not by a direct reopening from either inactivated state (Fig. 20D, right). However, our study showed that the enhancement of C_1 occupancy before the EAD takeoff was mainly due to a decrease in CDI states occupancy (Fig. 21). Moreover, in our simulations with the GD-P protocol we found that I_{Ca} inactivation exhibited a notch before EAD takeoff, whereas VDI did not (Fig. 18G), as was also found experimentally (Yamada *et al.*, 2008). We found that also CDI (including both CDI_{SR} and CDI_{LTCC} components) had a notch, confirming the occurrence of recovery from CDI.

Conclusion

An improved LTCC Markov model has been developed by taking into account a small contribution of IDI (in addition to pure VDI) when Ba is the charge carrier, in order to describe more faithfully contributions of CDI and VDI to total I_{Ca} inactivation. This model allowed us to investigate realistically the effects of CDI changes in normal and prolonged APs. We predicted that CDI is crucial for AP repolarization (while VDI is less so), and showed that impairment of I_{Ca} CDI may be arrhythmogenic by affecting intracellular Ca cycling, through its effect on the time course of LTCC Ca fluxes and thus NCX. We conclude that our improved model is a useful tool to study the role of I_{Ca} kinetics during normal and altered repolarization at the single cell level, and given its computational tractability it could

be incorporated in tissue-scale/whole heart models to test how these cellular instabilities can induce arrhythmias.

Further work will be required to incorporate modulation of I_{Ca} gating by other molecules involved in its regulation, such as protein kinase A and Ca-CaM dependent protein kinase, as has been described in previous studies (Findlay, 2002a; Saucerman *et al.*, 2003; Saucerman & Bers, 2008; Hashambhoy *et al.*, 2009; Hashambhoy *et al.*, 2010; Soltis & Saucerman, 2010; Yang & Saucerman, 2012).

Acknowledgements

We wish to thank Drs. J. N. Weiss, A. Mahajan and D. Sato for providing mean data and individual current traces for I_{Ba} and I_{Ca}.

References

Alseikhan BA, DeMaria CD, Colecraft HM & Yue DT. (2002). Engineered calmodulins reveal the unexpected eminence of Ca2+ channel inactivation in controlling heart excitation. *Proc Natl Acad Sci U S A* **99,** 17185-17190.

Altamirano J & Bers DM. (2007). Voltage dependence of cardiac excitation-contraction coupling: unitary Ca2+ current amplitude and open channel probability. *Circ Res* **101,** 590-597.

Bassani JW, Bassani RA & Bers DM. (1994). Relaxation in rabbit and rat cardiac cells: species-dependent differences in cellular mechanisms. *J Physiol* **476,** 279-293.

Benitah JP, Alvarez JL & Gomez AM. (2010). L-type Ca(2+) current in ventricular cardiomyocytes. *J Mol Cell Cardiol* **48,** 26-36.

Bers DM. (2001). *Excitation-Contraction Coupling and Cardiac Contractile Force*. Kluwer Academic Press Dordrecht, The Netherlands.

Beuckelmann DJ & Wier WG. (1988). Mechanism of release of calcium from sarcoplasmic reticulum of guinea-pig cardiac cells. *J Physiol* **405,** 233-255.

Brunet S, Scheuer T & Catterall WA. (2009). Cooperative regulation of Cav1.2 channels by intracellular Mg^{2+}, the proximal C-terminal EF-hand, and the distal C-terminal domain. *J Gen Physiol* **134,** 81-94.

Catterall WA. (2000). Structure and regulation of voltage-gated Ca^{2+} channels. *Annu Rev Cell Dev Biol* **16,** 521-555.

Cens T, Rousset M, Leyris JP, Fesquet P & Charnet P. (2006). Voltage- and calcium-dependent inactivation in high voltage-gated Ca^{2+} channels. *Prog Biophys Mol Biol* **90,** 104-117.

Corrias A, Giles W & Rodriguez B. (2011). Ionic mechanisms of electrophysiological properties and repolarization abnormalities in rabbit Purkinje fibers. *Am J Physiol Heart Circ Physiol* **300,** H1806-1813.

Faber GM, Silva J, Livshitz L & Rudy Y. (2007). Kinetic properties of the cardiac L-type Ca2+ channel and its role in myocyte electrophysiology: a theoretical investigation. *Biophys J* **92,** 1522-1543.

Ferreira G, Yi J, Rios E & Shirokov R. (1997). Ion-dependent Inactivation of Barium Current through L-type Calcium Channels. *J Gen Physiol* **109,** 449-461.

Findlay I. (2002a). beta-Adrenergic stimulation modulates Ca2+- and voltage-dependent inactivation of L-type Ca2+ channel currents in guinea-pig ventricular myocytes. *J Physiol* **541,** 741-751.

Findlay I. (2002b). Voltage- and cation-dependent inactivation of L-type Ca^{2+} channel currents in guinea-pig ventricular myocytes. *J Physiol* **541,** 731-740.

Findlay I. (2002c). Voltage-dependent inactivation of L-type Ca2+ currents in guinea-pig

ventricular myocytes. *J Physiol* **545,** 389-397.

Grandi E, Pasqualini FS, Pes C, Corsi C, Zaza A & Severi S. (2009). Theoretical investigation of action potential duration dependence on extracellular Ca2+ in human cardiomyocytes. *J Mol Cell Cardiol* **46,** 332-342.

Hadley RW & Hume JR. (1987). An intrinsic potential-dependent inactivation mechanism associated with calcium channels in guinea-pig myocytes. *J Physiol* **389,** 205-222.

Hashambhoy YL, Greenstein JL & Winslow RL. (2010). Role of CaMKII in RyR leak, EC coupling and action potential duration: a computational model. *J Mol Cell Cardiol* **49,** 617-624.

Hashambhoy YL, Winslow RL & Greenstein JL. (2009). CaMKII-induced shift in modal gating explains L-type Ca(2+) current facilitation: a modeling study. *Biophys J* **96,** 1770-1785.

Hryshko LV & Bers DM. (1992). Citrate alters Ca channel gating and selectivity in rabbit ventricular myocytes. *Am J Physiol* **262,** C191-198.

Imredy JP & Yue DT. (1994). Mechanism of Ca(2+)-sensitive inactivation of L-type Ca2+ channels. *Neuron* **12,** 1301-1318.

Jafri MS, Rice JJ & Winslow RL. (1998). Cardiac Ca2+ dynamics: the roles of ryanodine receptor adaptation and sarcoplasmic reticulum load. *Biophys J* **74,** 1149-1168.

January CT & Riddle JM. (1989). Early afterdepolarizations: mechanism of induction and block. A role for L-type Ca2+ current. *Circ Res* **64,** 977-990.

January CT, Riddle JM & Salata JJ. (1988). A model for early afterdepolarizations: induction with the Ca2+ channel agonist Bay K 8644. *Circ Res* **62,** 563-571.

Katzka DA & Morad M. (1989). Properties of calcium channels in guinea-pig gastric myocytes. *J Physiol* **413,** 175-197.

Lee KS, Marban E & Tsien RW. (1985). Inactivation of calcium channels in mammalian heart cells: joint dependence on membrane potential and intracellular calcium. *J Physiol* **364,** 395-411.

Lee YS, Dun W, Boyden PA & Sobie EA. (2011). Complex and rate-dependent beat-to-beat variations in Ca^{2+} transients of canine Purkinje cells. *J Mol Cell Cardiol* **50,** 662-669.

Linz KW & Meyer R. (1998). Control of L-type calcium current during the action potential of guinea-pig ventricular myocytes. *J Physiol* **513 (Pt 2),** 425-442.

Linz KW & Meyer R. (2000). Profile and kinetics of L-type calcium current during the cardiac ventricular action potential compared in guinea-pigs, rats and rabbits. *Pflugers Arch* **439,** 588-599.

Luo CH & Rudy Y. (1994a). A dynamic model of the cardiac ventricular action potential. I. Simulations of ionic currents and concentration changes. *Circ Res* **74,** 1071-1096.

Luo CH & Rudy Y. (1994b). A dynamic model of the cardiac ventricular action potential. II. Afterdepolarizations, triggered activity, and potentiation. *Circ Res* **74,** 1097-1113.

Mahajan A, Sato D, Shiferaw Y, Baher A, Xie LH, Peralta R, Olcese R, Garfinkel A, Qu Z & Weiss JN. (2008a). Modifying L-type calcium current kinetics: consequences for cardiac excitation and arrhythmia dynamics. *Biophys J* **94,** 411-423.

Mahajan A, Shiferaw Y, Sato D, Baher A, Olcese R, Xie L-H, Yang M-J, Chen P-S, Restrepo JG, Karma A, Garfinkel A, Qu Z & Weiss JN. (2008b). A Rabbit Ventricular Action Potential Model Replicating Cardiac Dynamics at Rapid Heart Rates. *Biophys J* **94,** 392.

Matsuda H. (1986). Sodium conductance in calcium channels of guinea-pig ventricular cells induced by removal of external calcium ions. *Pflugers Arch* **407,** 465-475.

Milberg P, Pott C, Fink M, Frommeyer G, Matsuda T, Baba A, Osada N, Breithardt G, Noble D & Eckardt L. (2008). Inhibition of the Na+/Ca2+ exchanger suppresses torsades de pointes in an intact heart model of long QT syndrome-2 and long QT syndrome-3. *Heart Rhythm* **5,** 1444-1452.

Mitarai S, Kaibara M, Yano K & Taniyama K. (2000). Two distinct inactivation processes related to phosphorylation in cardiac L-type Ca(2+) channel currents. *Am J Physiol Cell Physiol* **279,** C603-610.

Ozawa T, Sasaki K & Umezawa Y. (1999). Metal ion selectivity for formation of the calmodulin-metal-target peptide ternary complex studied by surface plasmon resonance spectroscopy. *Biochim Biophys Acta* **1434,** 211-220.

Peterson BZ, DeMaria CD, Adelman JP & Yue DT. (1999). Calmodulin is the Ca2+ sensor for Ca2+ -dependent inactivation of L-type calcium channels. *Neuron* **22,** 549-558.

Peterson BZ, Lee JS, Mulle JG, Wang Y, de Leon M & Yue DT. (2000). Critical determinants of Ca(2+)-dependent inactivation within an EF-hand motif of L-type Ca(2+) channels. *Biophys J* **78,** 1906-1920.

Priori SG & Corr PB. (1990). Mechanisms underlying early and delayed afterdepolarizations induced by catecholamines. *Am J Physiol* **258,** H1796-1805.

Puglisi JL, Yuan W, Bassani JW & Bers DM. (1999). Ca^{2+} influx through Ca^{2+} channels in rabbit ventricular myocytes during action potential clamp: influence of temperature. *Circ Res* **85,** e7-e16.

Restrepo JG, Weiss JN & Karma A. (2008). Calsequestrin-mediated mechanism for cellular calcium transient alternans. *Biophys J* **95,** 3767-3789.

Romero L, Carbonell B, Trenor B, Rodriguez B, Saiz J & Ferrero JM. (2011). Systematic characterization of the ionic basis of rabbit cellular electrophysiology using two ventricular models. *Prog Biophys Mol Biol* **107,** 60-73.

Sako H, Sperelakis N & Yatani A. (1998). Ca2+ entry through cardiac L-type Ca2+ channels modulates beta-adrenergic stimulation in mouse ventricular myocytes. *Pflugers Arch* **435,** 749-752.

Saucerman JJ & Bers DM. (2008). Calmodulin mediates differential sensitivity of CaMKII and calcineurin to local Ca2+ in cardiac myocytes. *Biophys J* **95,** 4597-4612.

Saucerman JJ, Brunton LL, Michailova AP & McCulloch AD. (2003). Modeling beta-adrenergic control of cardiac myocyte contractility in silico. *J Biol Chem* **278,** 47997-48003.

Shannon TR, Wang F, Puglisi J, Weber C & Bers DM. (2004). A mathematical treatment of integrated Ca dynamics within the ventricular myocyte. *Biophys J* **87,** 3351-3371.

Sipido KR, Volders PG, de Groot SH, Verdonck F, Van de Werf F, Wellens HJ & Vos MA. (2000). Enhanced Ca(2+) release and Na/Ca exchange activity in hypertrophied canine ventricular myocytes: potential link between contractile adaptation and arrhythmogenesis. *Circulation* **102,** 2137-2144.

Soltis AR & Saucerman JJ. (2010). Synergy between CaMKII substrates and beta-adrenergic signaling in regulation of cardiac myocyte Ca(2+) handling. *Biophys J* **99,** 2038-2047.

Sonoda S & Ochi R. (2001). Independent modulation of L-type Ca2+ channel in guinea pig ventricular cells by nitrendipine and isoproterenol. *Jpn Heart J* **42,** 771-780.

Splawski I, Timothy KW, Decher N, Kumar P, Sachse FB, Beggs AH, Sanguinetti MC & Keating MT. (2005). Severe arrhythmia disorder caused by cardiac L-type calcium channel mutations. *Proc Natl Acad Sci U S A* **102,** 8089-8096.

Splawski I, Timothy KW, Sharpe LM, Decher N, Kumar P, Bloise R, Napolitano C, Schwartz PJ, Joseph RM, Condouris K, Tager-Flusberg H, Priori SG, Sanguinetti MC & Keating MT. (2004). CaV1.2 Calcium Channel Dysfunction Causes a Multisystem Disorder Including Arrhythmia and Autism. *Cell* **119,** 19.

Sun H, Leblanc N & Nattel S. (1997). Mechanisms of inactivation of L-type calcium channels in human atrial myocytes. *Am J Physiol* **272,** H1625-1635.

Sun L, Fan J, Clark J & Palade P. (2000). A model of the L-type Ca2+ channel in rat ventricular myocytes: ion selectivity and inactivation mechanisms. *J Physiol* **529,** 139-158.

Sung RJ, Wu YH, Lai NH, Teng CH, Luo CH, Tien HC, Lo CP & Wu SN. (2010). Beta-adrenergic modulation of arrhythmogenesis and identification of targeted sites of antiarrhythmic therapy in Timothy (LQT8) syndrome: a theoretical study. *Am J Physiol Heart Circ Physiol* **298,** H33-44.

Tanskanen AJ, Greenstein JL, O'Rourke B & Winslow RL. (2005). The role of stochastic and modal gating of cardiac L-type Ca2+ channels on early after-depolarizations. *Biophys J* **88,** 85-95.

Thiel WH, Chen B, Hund TJ, Koval OM, Purohit A, Song LS, Mohler PJ & Anderson ME. (2008). Proarrhythmic defects in Timothy syndrome require calmodulin kinase II. *Circulation* **118,** 2225-2234.

Yamada M, Ohta K, Niwa A, Tsujino N, Nakada T & Hirose M. (2008). Contribution of L-type Ca2+ channels to early afterdepolarizations induced by I Kr and I Ks channel suppression in guinea pig ventricular myocytes. *J Membr Biol* **222,** 151-166.

Yamazaki J, Urushidani T & Nagao T. (1996). Barium activates rat cerebellar nitric oxide synthase. *Jpn J Pharmacol* **70,** 351-354.

Yang J, Ellinor PT, Sather WA, Zhang JF & Tsien RW. (1993). Molecular determinants of Ca2+ selectivity and ion permeation in L-type Ca2+ channels. *Nature* **366,** 158-161.

Yang JH & Saucerman JJ. (2012). Phospholemman is a negative feed-forward regulator of Ca2+ in beta-adrenergic signaling, accelerating beta-adrenergic inotropy. *J Mol Cell Cardiol* **52,** 1048-1055.

Yarotskyy V, Gao G, Peterson BZ & Elmslie KS. (2009). The Timothy syndrome mutation of cardiac CaV1.2 (L-type) channels: multiple altered gating mechanisms and pharmacological restoration of inactivation. *J Physiol* **587,** 551-565.

Yuan W & Bers DM. (1995). Protein kinase inhibitor H-89 reverses forskolin stimulation of cardiac L-type calcium current. *Am J Physiol* **268,** C651-659.

Yuan W, Ginsburg KS & Bers DM. (1996). Comparison of sarcolemmal calcium channel current in rabbit and rat ventricular myocytes. *J Physiol* **493,** 733-746

Zeng J & Rudy Y. (1995). Early afterdepolarizations in cardiac myocytes: mechanism and rate dependence. *Biophys J* **68,** 949-964.

Zhong J, Hwang TC, Adams HR & Rubin LJ. (1997). Reduced L-type calcium current in ventricular myocytes from endotoxemic guinea pigs. *Am J Physiol* **273,** H2312-2324.

Zhu ZI & Clancy CE. (2007). L-type Ca2+ channel mutations and T-wave alternans: a model study. *Am J Physiol Heart Circ Physiol* **293,** H3480-3489.

Zuhlke RD, Pitt GS, Deisseroth K, Tsien RW & Reuter H. (1999). Calmodulin supports both inactivation and facilitation of L-type calcium channels. *Nature* **399,** 159-162.

CHAPTER 3

Arrhythmogenic Consequences of the Crosstalk between β-Adrenergic and CaMKII Signaling in a Murine Model of Heart Failure

Short title: Crosstalk between βAR and CaMKII Signaling in HF.

The following authors have contributed to the study presented in this chapter:

Grandi E [1], Edwards AG [2], McCulloch AD [2] & Bers DM [1].

[1] University of California in Davis, CA, USA
[2] University of California in San Diego, CA, USA

Abstract

Alterations in myocyte neurohumoral regulation, ion currents, Ca handling, and contractility, accompanied by ventricular hypertrophy and structural remodeling, all contribute to heart failure (HF). Ca-calmodulin dependent protein kinase (CaMKII) is upregulated and more active in HF, and is a key regulator of cellular subsystems contributing to acute mechanical and electrical dysfunction as well as chronic cardiac remodeling in HF. CaMKII overexpression (CaMKII-OE) leads to HF in mice, while CaMKII knockout or inhibition can protect against failure. In HF β-adrenergic tone is upregulated as well, and can activate CaMKII via protein kinase A (PKA) dependent or independent signaling pathways. We developed a new mathematical model of excitation-contraction coupling (ECC) in the murine ventricular myocyte, based on a previously validated rabbit action potential (AP) model that integrates the effects of CaMKII and PKA phosphorylation. We modified the description of cell geometry, ion channel, Ca and Na transporter expression and function, and CaMKII and PKA phosporylation effects to account for the experimentally observed differences of mouse *vs*. rabbit cardiomyocytes, and the most recent experimental data from murine ventricular myocytes recorded at physiological temperature. The model was validated in control condition against the experimentally observed frequency response of Ca dynamics, [Na], AP shape and duration. Then we validated the effects of CaMKII-OE and of PKA activation in control condition. When simulating PKA activation in CaMKII-OE condition, the model predicts arrhythmogenic activity, due to spontaneous Ca release from the sarcoplasmic reticulum that triggers the inward flux of the Na-Ca exchanger. Our model provides a useful quantitative framework to examine how CaMKII and PKA signaling pathways interact to coordinate ECC and arrhythmia in the context of HF. For example, it can be used to test which CaMKII targets are most arrhythmogenic or to assess the effects of acute *vs*. chronic CaMKII hyperactivity. Moreover, a systematic framework accounting for electrophysiological differences among species could be developed to extrapolate findings in the genetically engineered mice to the clinical setting.

INTRODUCTION

Heart failure (HF) is a pathology characterized by the inability of the heart to provide sufficient pump action to meet circulatory demand, usually associated to many symptoms including shortness of breath, leg swelling, and exercise intolerance. HF is a rapidly growing health problem, now approaching important proportions in industrialized societies (Lloyd-Jones *et al.*, 2009), where around 2% of adults is affected (McMurray & Pfeffer, 2005), and the fraction increases until 6 to 10% among over-65 people. Moreover, the estimated cost of HF is high (currently about 2% of the total healthcare spend in developed societies) and it is expected to rise (McMurray & Stewart, 2000). HF phenotype presents alterations in electrical conduction, energy metabolism, myocyte ion currents, Ca handling, contractile function and their neurohormonal regulation, accompanied by ventricular hypertrophy and structural remodeling (Jessup & Brozena, 2003; Stanley *et al.*, 2005). About half of HF deaths are due to pump failure and half to arrhythmias, especially tachyarrhythmia. To treat these phenomena, the use of implantable devices has been often preferred to pharmacologic therapy, and this is mainly due to an inadequate understanding of fundamental mechanisms of

arrhythmogenesis in the large number of disease states which culminate in HF (Wang & Hill, 2010).

The last decades have seen rapid advances in the understanding of the genetic and physiological processes, mainly as a result of the diffusion of animal modeling. The aim of this kind of research is to create a simplified framework (if compared to the human pathologic phenotype) where to study only one of the features characterizing an extremely complex syndrome like HF. At the same time, working with animal models, as opposed to isolated organs or cells, allows to analyze the physiological effects of cardiac dysfunction on a wider scale. Depending on the feature to investigate, different techniques have been adopted to create animal model of HF: surgical intervention (like banding an aorta or clipping a coronary artery), administration of a single toxin or drug, or genetic manipulation of the animal genome. In particular, this last approach has been developed and applied to individually investigate the changes in gene expression associated with HF by targeted mutagenesis/transgenesis or pharmacology (Breckenridge, 2010). Another key decision is the choice of animal species. Mouse models have been generally preferred to other bigger mammalian models (often presenting more similarities with the human physio-anatomy) due to the relatively complete annotation and simple manipulation of the murine genome (Breckenridge, 2010), and their relative inexpensiveness and practicality. Despite the differences between mouse and human (Bers, 2001; Kaese & Verheule, 2012), mouse models are now indispensable tools in many areas of medical research and the common features of murine and human hearts have allowed for many important observations regarding embryology, physiology, cell signaling, energetics and stem cell function (Breckenridge, 2010). Indeed, mouse models are able to recapitulate major clinical features of HF with specifically defined molecular triggers and, up to now, over 5000 cardiac transgenic/knockout studies have been published (Breckenridge, 2010). The wealth of data on alterations in cell

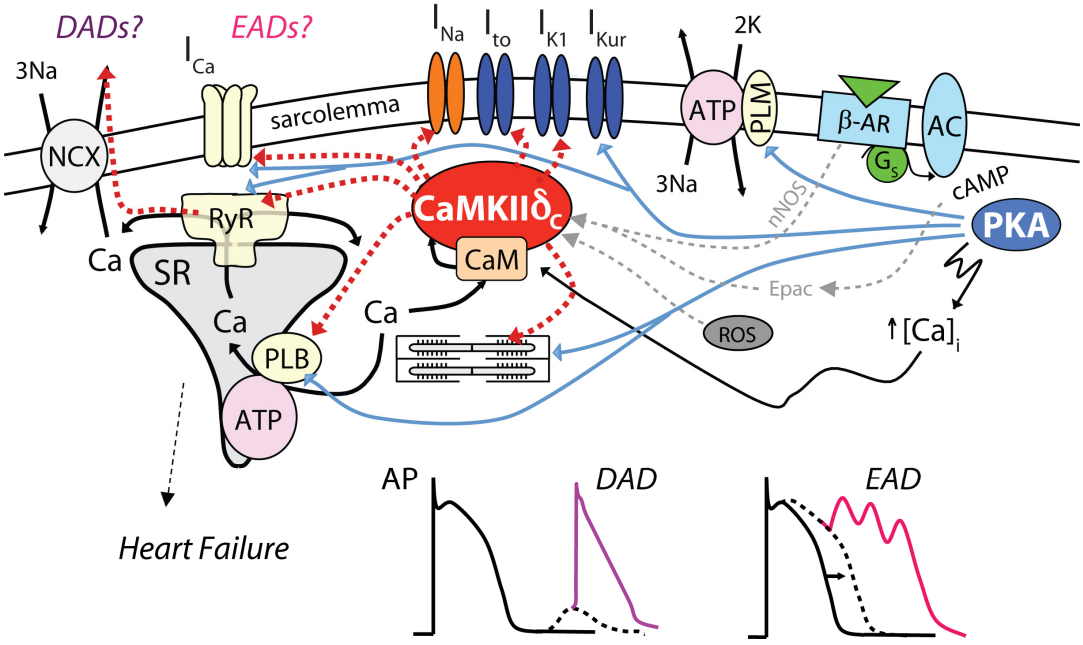

Figure 1. Schematic representation of CaMKII and PKA targets in mouse ventricular myocytes. Modified from (Bers & Grandi, 2009).

signaling, electrophysiology, Ca handling, myofilament function and tissue structure that can be measured in these mice cannot be obtained in humans, but integrative models provide a systematic framework to extrapolate findings in the genetically engineered mouse to the clinical setting.

The use of mouse models has proven useful in the study of the signaling network of Ca-calmodulin dependent protein kinase (CaMKII), that is believed to contribute significantly to acute mechanical and electrical dysfunction as well as chronic cardiac remodeling in HF (Bers & Grandi, 2009). CaMKII, a key nodal point in modulating the excitation-contraction coupling (ECC), is upregulated and more active in HF, as experimentally observed in human (Hoch *et al.*, 1999; Ai *et al.*, 2005). Moreover, cardiac myocyte-specific overexpression (OE) of CaMKII leads to a severe HF and arrhythmias in mice (Zhang *et al.*, 2003), while CaMKII knockout or inhibition can protect against decompensation in HF in mice. In fact, CaMKII influences ECC by affecting several electrical and Ca-handling proteins (Maier & Bers, 2007; Bers & Grandi, 2009), and, by exerting multiple effects on numerous targets, can simultaneously favor HF and arrhythmias (Fig.1), as observed in transgenic CaMKII mice (Wagner & Maier, 2006; Sag *et al.*, 2009). It has been shown that CaMKII alters the gating of L-type Ca current (I_{Ca}) (Yuan & Bers, 1994), ryanodine receptors (RyRs) (Guo *et al.*, 2006), Na and K currents (Wagner *et al.*, 2006; Wagner *et al.*, 2009). Moreover, CaMKII phosphorylation of phospholamban (PLB) releases its inhibition on Ca-sensitivity of SR Ca pump (SERCA) (Odermatt *et al.*, 1996), thus causing an increase in the pump affinity for Ca.

Elevated levels of circulating catecholamines is a hallmark of human congestive HF, resulting in chronic activation of the β-adrenergic (βAR) pathway and consequent loss of βAR sensitivity (Wehrens *et al.*, 2004). βAR regulation of ECC is initiated by the coupling between βAR receptor and the stimulatory G protein, and the subsequent stimulation of adenylyl cyclase (AC), which synthesizes the cyclic adenosine monophosphate (cAMP). cAMP activates protein kinase A (PKA), that phosphorylates a wide spectrum of target proteins (Fig. 1) including L-type Ca channels (LTCCs), RyRs, and PLB (Grandi & Bers, in press). Thus βAR stimulation can influence CaMKII (whose activity responds to the frequency and magnitude of Ca signals) via the PKA-dependent enhancement of I_{Ca} and sarcoplasmic reticulum (SR) Ca uptake and consequent increase in SR Ca release and Ca transient (CaT) amplitude. More recently, other PKA-independent mechanisms have been postulated (see Discussion and Fig. 1).

The use of mathematical models has been notably successful in contributing to understand the mechanisms regulating the ECC and the underlying arrhythmogenic activities, but none of the different mouse models available in literature (Bondarenko *et al.*, 2004; Demir, 2005; Shin *et al.*, 2008; Wang & Sobie, 2008; Koivumaki *et al.*, 2009; Li *et al.*, 2010; Li *et al.*, 2011; Li *et al.*, 2012; Yang & Saucerman, 2012) presents a satisfactory description of both CaMKII and PKA signaling pathways. In the area of CaMKII signaling pathway description, some groups recently published models linking CaMKII to ECC in different mammalian models (Hund & Rudy, 2004; Iribe *et al.*, 2006; Grandi *et al.*, 2007; Livshitz & Rudy, 2007), though in all cases the focus was on consequences to ECC, with only limited representation of CaMKII activation mechanisms. The first model with an explicit inclusion of calmodulin (CaM) in the CaMKII pathway has been recently developed (Saucerman & Bers, 2008); it incorporates compartmental Ca, CaM, CaMKII and phosphatases, including calcineurin (CaN), based on measured concentrations, binding kinetics and target

phosphorylation, into the framework of a strongly validated rabbit ventricular AP model (Shannon *et al.*, 2004). As far the βAR stimulation is concerned, the McCulloch group was arguably the first to develop a detailed mechanistic biochemical model of PKA signaling and its regulation of rabbit ECC (Saucerman *et al.*, 2004), which was initially developed for the rat ventricular myocyte (Saucerman *et al.*, 2003; Saucerman & McCulloch, 2004). The Saucerman group (Soltis & Saucerman, 2010) integrated the model of PKA signaling (Saucerman *et al.*, 2004) with the model of CaMKII signaling (Saucerman & Bers, 2008) into the Shannon-Bers model of rabbit AP (Shannon *et al.*, 2004). Recently the same group developed a murine AP model (Yang & Saucerman, 2012) updating the description of the PKA activation.

METHODS

In order to study how βAR stimulation and CaMKII signaling interact in ECC regulation in context of HF in mouse ventricular myocytes, we integrated the most recent descriptions of CaMKII (Saucerman & Bers, 2008) and PKA (Yang & Saucerman, 2012) signaling pathways into a newly parameterized murine ECC model. In particular we started from the Soltis-Saucerman rabbit AP model (Soltis & Saucerman, 2010), built upon the Shannon-Bers model framework (Shannon *et al.*, 2004). We took into account all the differences observed in mouse *vs*. rabbit cardiomyocytes (Bers, 2001), and the most recent experimental data from murine ventricular myocytes, regarding cell geometry, ion currents, Ca and Na handling and CaMKII phosphorylation effect. Parameters were manually fitted to experimental measurements recorded at physiological temperature. Data obtained at room temperature have been scaled at

Table 1. Summary of geometric differences between rabbit and mouse ECC models.

Geometry			Rabbit	Mouse
Volume	V_{tot}	(pL)	33	
	V_{cyt}	(pL)	65% V_{tot}	
	V_{SL}	(pL)	0.2% V_{tot}	
	V_j	(pL)	0.0539% V_{tot}	
	V_{SR}	(pL)	3.5% V_{tot}	
Surface	A_{tot}	(cm^2)	$1.46e^{-4}$	$2e^{-4}$
	F_{SL}	(-)	89%	81%
	A_{SL}	(cm^2)	F_{SL} A_{tot}	
	F_j	(-)	11%	19%
	A_j	(cm^2)	F_j A_{tot}	
Junctions		(#)	20150	46627
Spacing		(μm)	1.2	0.93
Diffusion	d_{xj-SL}	(μm)	0.5	0.3
	A_{j-SL}	(μm^2)	303	703
	d_{SL-cyt}	(μm)	0.45	
	A_{SL-cyt}	(μm^2)	A_{SL}	
Surface/Volume		(pF/pL)	4.1848	6.0606
Capacitance		(pF)	138.1	200
Dishomogeneous distribution	$F_{j,\ LTCC}$	(-)	90%	
	$F_{j,\ NKA}$	(-)	11%	23%

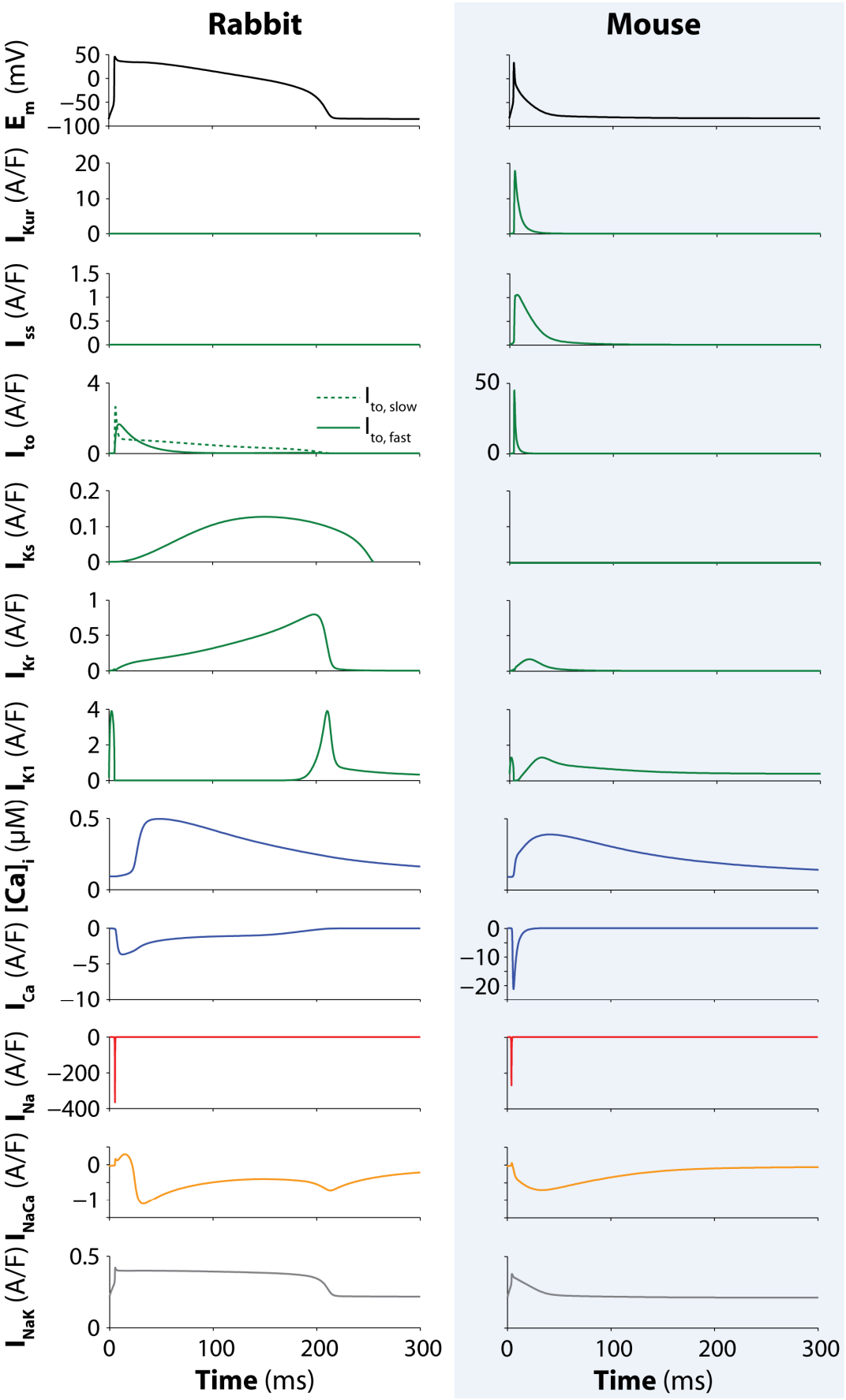

Figure 2. Rabbit *vs.* mouse electrophysiology. AP, CaT and underlying ionic currents in the rabbit (left column) and mouse (right) ventricular myocyte models paced at 1 Hz in control condition.

37°C using different Q_{10} factors derived from literature (Xu *et al.*, 1999; Brouillette *et al.*, 2004). The model has been validated in control condition against the experimentally measured frequency response of Ca dynamics, [Na], AP shape and duration. The effects of 6-fold CaMKII-OE have been evaluated, as well as the effects of βAR activation. To this end, we substituted the original description of PKA activation (Saucerman *et al.*, 2004; Soltis & Saucerman, 2010) with the updated fully ordinary differential equations (ODEs) implementation of the βAR stimulation developed in the Yang-Saucerman model of murine ventricular AP (Yang & Saucerman, 2012), with appropriate adaptations to the Shannon-Bers model framework. We studied the consequences of PKA activation in both control and CaMKII-OE conditions by simulating the application of the agonist isoproterenol (ISO) at a concentration of 100 nM. The fully integrated model is a system of ODEs implemented in MATLAB (Mathworks, Natick, MA, USA) and solved numerically using a variable order solver (ode15s).

RESULTS

Cell geometry

Compared to rabbit, murine ventricular cell presents an increased surface area (Satoh *et al.*, 1996), while the volume is unchanged; consequently the membrane capacitance increases (Knollmann *et al.*, 2000). Mouse presents a bigger fraction of transverse-tubules (t-tubules) in junctions (Page & Surdyk-Droske, 1979). This change, together with the increase in total surface area, leads to an increase in the junctional surface, hence to an increase of the number of junctions and a decrease of the distance among them (Li *et al.*, 2012). We assumed homogeneous distribution of channels and transporters, except LTCCs (90% in junctions as in rabbit) and Na-K pump (NKA, 23% in junctions). In fact, it has been shown that in murine ventricle the total pump density is about 60% higher in t-tubules *vs*. external sarcolemma (Berry *et al.*, 2007). Table 1 offers a more detailed overview of the geometric differences between rabbit and mouse models.

K currents

Mouse and rabbit ventricular APs differ significantly (Nerbonne, 2004), in that the former is characterized by triangular shape (absence of plateau) and brief duration (~35 ms), whereas the latter lasts hundreds of ms and exhibits a prominent plateau phase (Fig. 2). These differences are mainly explained by different expression of repolarizing K currents (Fig. 2).

In mouse ventricular myocyte the transient outward K current (I_{to}) is composed mainly by the fast component ($I_{to,fast}$), which is highly expressed, whereas the slow component ($I_{to,slow}$) has been shown to be expressed only in the septum (Guo *et al.*, 1999). We modified I_{to} density and kinetics to fit a set of voltage-clamp data (scaled at physiological temperature) that includes the peak current-membrane potential (E_m) relationship (I-V, Fig. 3A), steady-state activation and inactivation (SSA and SSI, Fig. 3C), time constants of activation (τ_{act}, Fig. 3AB), inactivation and recovery from inactivation (τ_{inact}, Fig. 3D). When the murine I_{to} is included in the Soltis-Saucerman model, the plateau level decreases and the AP shortens (Fig. 3L).

Also the slow delayed rectifier current (I_{Ks}) is absent in mouse ventricular cell (Nerbonne, 2004), where two others K currents (both absent in rabbit ventricular cell) are expressed: a rapidly activating and slowly inactivating current (I_{Kur}) and a non-inactivating

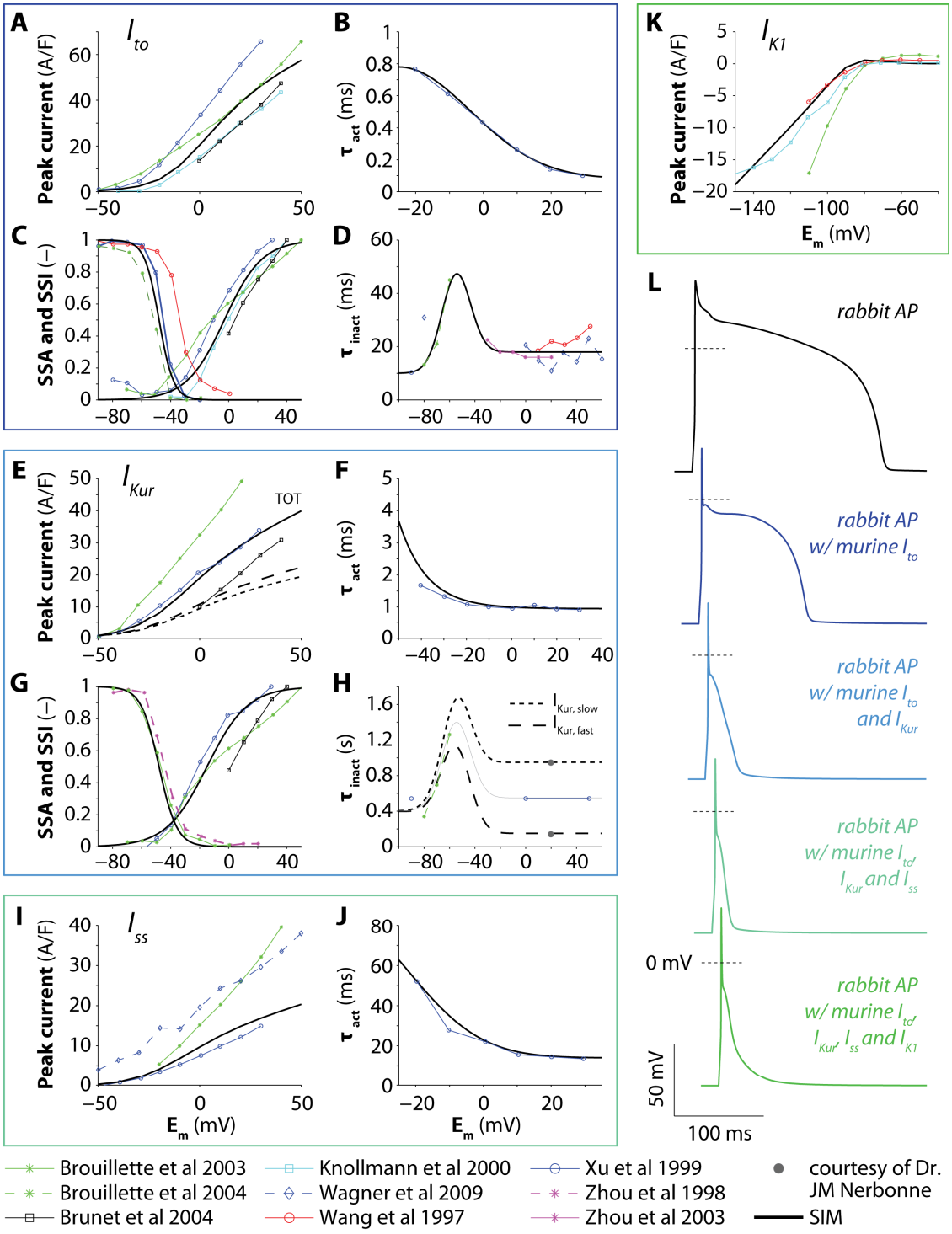

Figure 3. Characterization of murine K currents: I_{to}, I_{Kur}, I_{ss} and I_{K1}. Experimental (symbols) and simulated (solid lines) I-V relationship (I_{to} in panel A, I_{Kur} in E, I_{ss} in I, I_{K1} in K), time constant of activation (I_{to} in B, I_{Kur} in F, I_{ss} in J), SSA and SSI (I_{to} in C, I_{Kur} in G), time constant of inactivation and recovery from inactivation (I_{to} in D, I_{Kur} in H). Simulated rabbit AP changes as more mouse-like features are progressively included (L). Experimental data from (Wang & Duff, 1997; Zhou *et al.*, 1998; Xu *et al.*, 1999; Knollmann *et al.*, 2000; Brouillette *et al.*, 2003; Zhou *et al.*, 2003; Brouillette *et al.*, 2004; Brunet *et al.*, 2004; Wagner *et al.*, 2009) or provided by the Nerbonne group.

steady-state current (I_{ss}). These two currents share the same SSA function (Fig 3G), with markedly different time constants of activation (Fig. 3F and J). We integrated their descriptions as formulated by the Smith group (Li *et al.*, 2010), and modified the parameters to fit the experimental observed I-V, SSA, SSI, τ_{act} and τ_{inact} (Fig. 3E-J). Recent findings by the Nerbonne group showed that I_{Kur} has two different components ($I_{Kur,fast}$ and $I_{Kur,slow}$), characterized by different time constants of inactivation and with almost the same densities

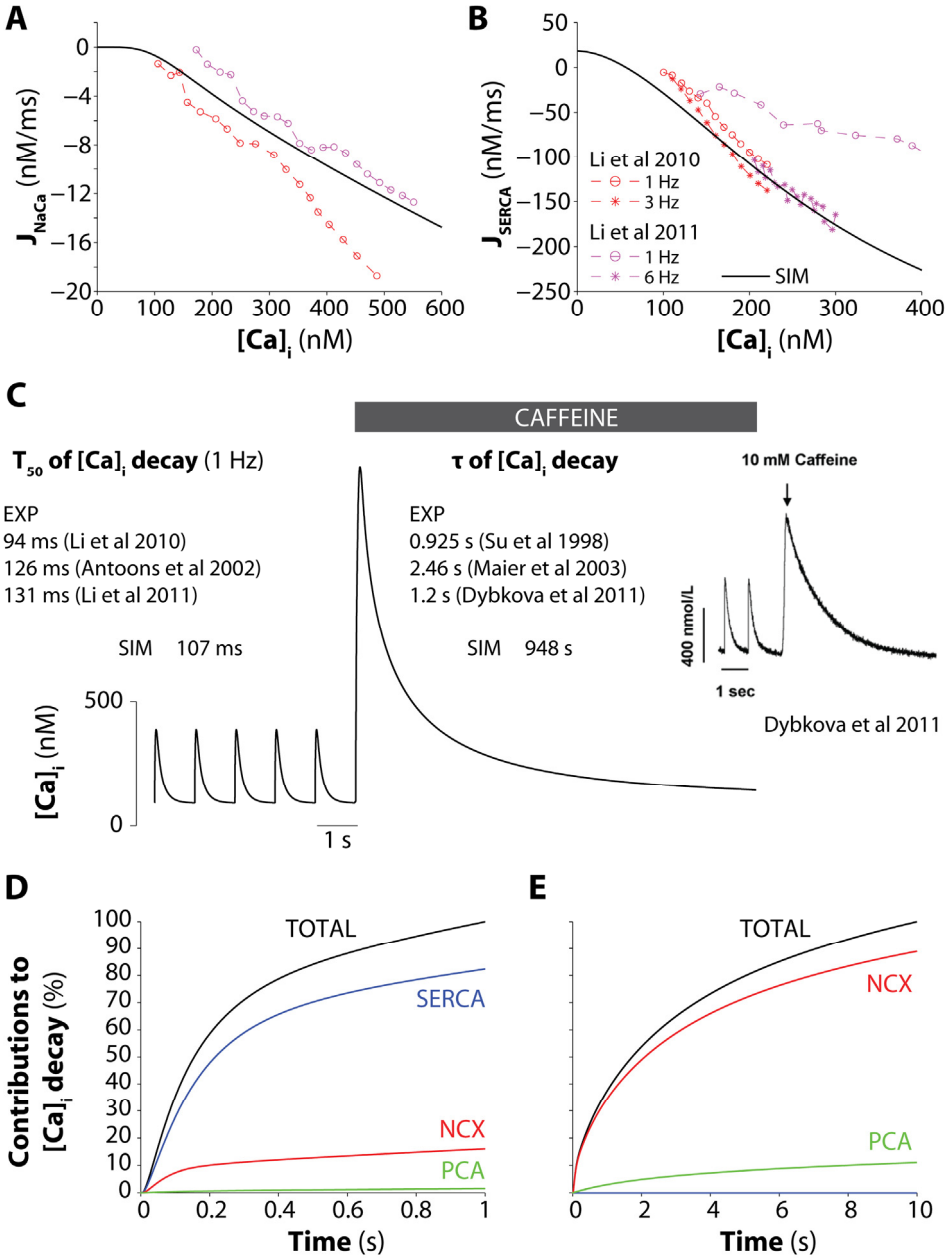

Figure 4. Characterization of NCX and SERCA functions. Experimental (symbols) and simulated (solid lines) Ca-dependence of NCX (panel A) and SERCA (B) fluxes. Simulated caffeine-induced CaT after steady-state stimulation at 1 Hz (C); inset shows the experimental recording. Caffeine application was simulated in absence of external stimulation, forcing the SR Ca release by enhancing the RyR open probability and inhibiting the SERCA function. Relative contributions of SERCA, NCX and plasma membrane Ca pump (PCA) to $[Ca]_i$ decay during a normal twitch (D) and during a caffeine-induced CaT (E). Experimental data from (Su *et al.*, 1998; Antoons *et al.*, 2002; Maier *et al.*, 2003; Li *et al.*, 2010; Dybkova *et al.*, 2011; Li *et al.*, 2011).

(respectively 53.3 and 46.7% of the total I_{Kur}). Thus, we modified the original formulation introducing the differentiation in the two components (Fig. 3H). The inclusion of I_{Kur} and I_{ss} eliminates the AP plateau and further shortens the AP (Fig. 3L).

Magnitude of the inward rectifier K current (I_{K1}) was reduced (Fig. 3K) compared to rabbit, causing a prolongation of the AP phase 3 (Fig. 3L).

Ca and Na handling

Despite the shorter duration of the AP and the reduced extracellular [Ca] (1 *vs*. 1.8 mM), the Ca influx in mouse is comparable with the one seen in rabbit. In agreement with experimental data (Li *et al.*, 2011; Li *et al.*, 2012), the density of I_{Ca} has been increased to reproduce the peak current (Fig. 2) and the Ca influx during an AP (0.1 pC/pF).

SERCA and Na-Ca exchanger (NCX) have been tuned to reproduce the Ca-dependence of their fluxes (Fig. 4A and B) and their relative contributions to the Ca efflux. We simulated caffeine application after steady-state stimulation at 1 Hz (Fig. 4C), to analyze the intracellular [Ca] ($[Ca]_i$) decay during both a physiological twitch and a caffeine-induced CaT. The model was set to reproduce the time to half $[Ca]_i$ decay experimentally observed in both cases. In agreement with experimental data (Li *et al.*, 1998), SERCA is the major contributor to cytosolic Ca removal in normal condition, whereby NCX extrudes most of the released Ca (about 90%) after caffeine application.

Na current (I_{Na}) has been modified to fit the AP upstroke velocity (Edwards *et al.*, unpub.) and inactivation data (Wagner *et al.*, 2006). We modified SR leak current, Ca and Na background currents to obtain the proper Na and Ca concentrations at rest. We increased Na affinity for NKA and pump density in agreement with functional experimental data (Berry *et al.*, 2007). Moreover, the resting Na influx has been increased, since it has been experimentally shown that the resting Na influx in rat is about 3 times bigger than in rabbit (Despa *et al.*, 2002). Simulating strophanthidin application (resulting in a complete inhibition of NKA function) at rest, we obtained a diastolic Na influx of 2.27 mM/min (not shown).

CaMKII and PKA effects

Table 2 summarizes the regulatory effects of CaMKII and PKA phosphorylation included in the model. Both pathways dynamically regulate key Ca handling targets including LTCC, PLB and RyR, and thus influence Ca signaling by increasing I_{Ca} magnitude, SR Ca uptake and release. Phosphorylation of LTCC is thought to cause channel facilitation, which is manifested as a slight increase in peak current and slower inactivation (Kohlhaas *et al.*, 2006). RyR are hypersensitive upon CaMKII phosphorylation, which causes increased diastolic Ca leak (via Ca sparks). PLB is more expressed in mouse *vs*. rabbit (Yang & Saucerman, 2012), and its phosphorylation releases the inhibition of SERCA, increasing the affinity of this pump for intracellular [Ca].

Although CaMKII is present in all cytosolic compartments, its activation can occur only in the dyadic space, where $[Ca]_i$ reaches much higher levels than in the bulk cytosol. When increasing the pacing rate, dyadic CaMKII activity (Fig. 5A) and consequent target phosphorylation increase (Fig. 5B and C). Each target is characterized by different phosphorylation kinetics (Fig. 5B): LTCCs get phosphorylated very rapidly, RyRs more slowly, and PLB very slowly. Time-averaged steady-state phosphorylation levels are also

Table 2. Summary of included functional ECC regulation modules. All regulatory effects - except those ones indicated by *(*)* - are described using a mathematical formulation that differentiates the phosphorylation dynamics of each target. Modified from (Soltis & Saucerman, 2010).

Target	CaMKII	PKA
LTCC	Enhanced channel opening probability (both), facilitation (CaMKII), and recovery from inactivation (CaMKII); increased fraction of available channels (PKA).	
RyR	Enhanced channel opening probability (both) and leak (CaMKII).	
PLB	Enhanced Ca-sensitivity of SERCA (both kinases).	
I_{Na}	Shifted current availability towards hyperpolarized potentials, delayed recovery from inactivation, and enhanced late current magnitude *(*)*.	
I_{K1}	Decreased current magnitude *(*)*.	
I_{to}	Decreased current magnitude and faster recovery from inactivation *(*)*.	
I_{Kur}		Enhanced current magnitude.
I_{NaK}		Increased affinity for internal Na, with no effect on the maximum pump rate.
TnI		Decreased TnC affinity for Ca.

sensitive to the amount of CaMKII expression level (Fig. 5C). While CaMKII-mediated effects on I_{Ca}, RyR and PLB were not changed in mouse *vs*. rabbit, we adapted the phosphorylation effects on other targets, which dynamics are not considered, to murine physiology (according to experimental data). In mouse, CaMKII phosphorylation affects $I_{to,fast}$ by decreasing the magnitude by about one third, and by decreasing (-38%) the time constant of recovery from inactivation (Wagner *et al.*, 2009). In the same study, I_{K1} was found reduced by 50% in CaMKII-OE condition. We incorporated these changes in the model. Moreover, we increased the diastolic Na influx (simulated strophanthidin application results in a diastolic Na influx of 3.4 mM/min *vs*. 2.27 mM/min in WT) and the effect of CaMKII phosphorylation on peak and late I_{Na} in agreement with experimental data (Wagner *et al.*, 2006).

The description of PKA activation has been integrated as developed for mouse in the Yang-Saucerman model. Compared to rabbit, βAR receptors are less expressed in mouse ventricular myocytes, while the concentration of total AC is increased. PKA phosphorylation of troponin I (TnI) decreases myofilament Ca sensitivity in mouse as in rabbit. PKA phosphorylates also phospholamman (PLM), leading to an increase in the affinity of NKA for internal Na, with no effect on the maximum pump rate (Despa *et al.*, 2005). Moreover, we integrated into the Yang-Saucerman formulation the dynamic regulation of I_{Kur}, whose magnitude increases by 20% after 100 nM ISO application (Li *et al.*, 1996). Regulation of I_{Ks} and cystic fibrosis transmembrane conductance regulator current were not included here as mouse ventricular myocytes do not express these channels.

Model validation in WT and CaMKII-OE conditions

We validated the baseline mouse model against a wide set of experimental data measured at different stimulation frequencies and obtained good agreement as shown in Fig. 6. Fig. 6A

shows a little adaptation of AP duration (APD) as seen in experiments (Wagner *et al.*, 2009). The model also reproduces the measured increase of diastolic [Na] with the pacing rate (Fig. 6B). Analogous to experimental observations, CaT amplitude decreases with increasing frequency (Fig. 6C), as a result of increased diastolic and decreased systolic $[Ca]_i$ (Fig. 6D). Diastolic SR [Ca] is about 105 nmol/L cyt at rest and decreases with pacing until about 80 nmol/L cyt (at 3 Hz), then is basically unchanged until 8 Hz (not shown). The fractional release, measured as the ratio of the twitch to the caffeine-induced CaT, decreases as observed by the Sipido group (Antoons *et al.*, 2002). Fig. 6E shows the time to half $[Ca]_i$ decay (T_{50}), which decreases with the frequency, as experimentally observed, reflecting frequency-dependent acceleration of relaxation (FDAR).

When simulating 6-fold CaMKII-OE, we found a prolongation of the AP (Fig. 7A), in agreement with experimental results (Maier *et al.*, 2003; Wagner *et al.*, 2006; Wagner *et al.*, 2009; Dybkova *et al.*, 2011). This prolongation is mostly due the decrease in I_{to} expression, whereas gain of function in I_{Na} and I_{Ca} play a limited role (Wagner *et al.*, 2009). CaT

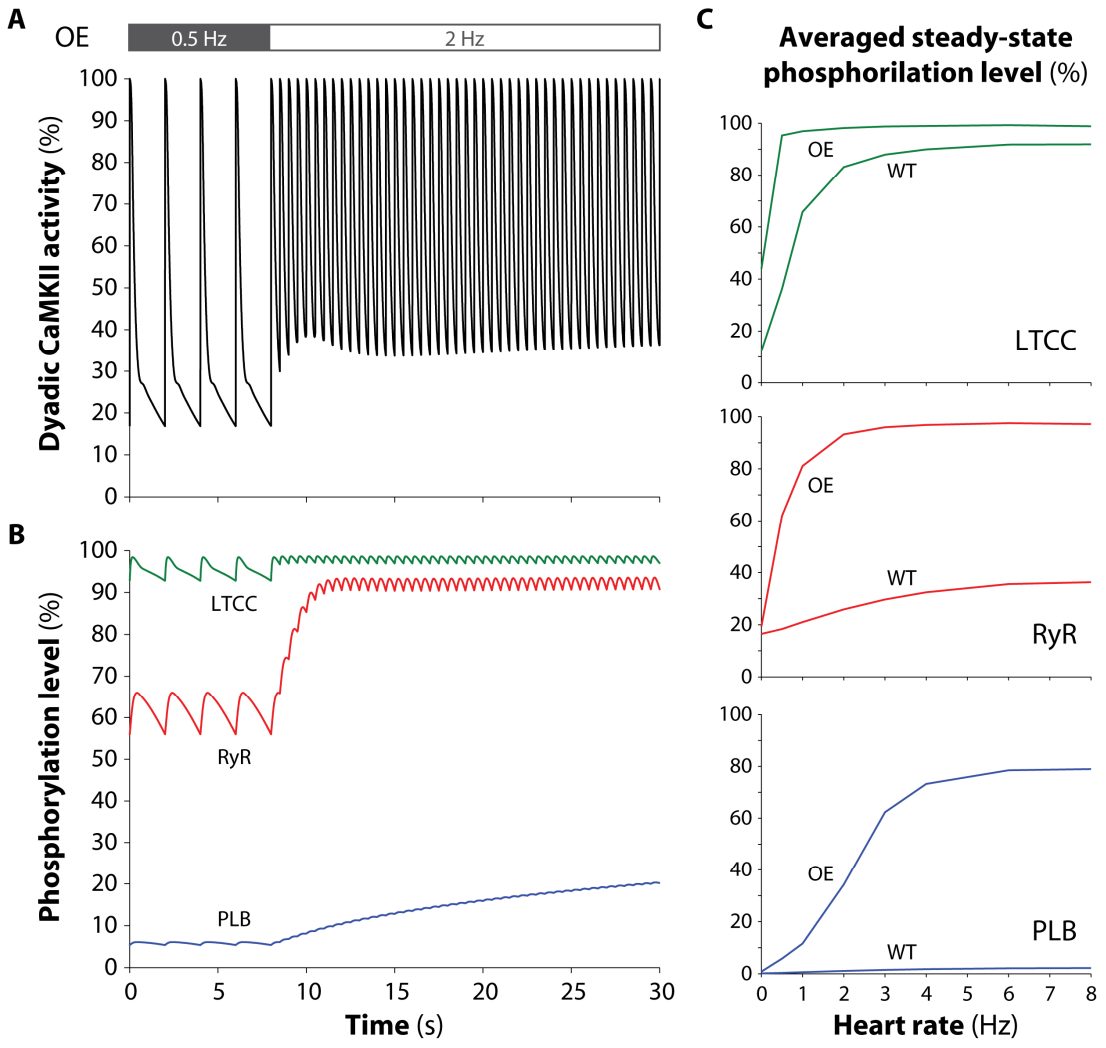

Figure 5. Time course and frequency-dependence of CaMKII phosphorylation. Dyadic CaMKII activity (panel A) and phosphorylation levels of LTCC, RyR and PLB (B) during a simulation in CaMKII-OE condition in which pacing rates is increased from 0.5 Hz to 2 Hz. Time-averaged steady-state phosphorylation levels (C) of LTCC (top) RyR (middle), and PLB (bottom) in control and CaMKII-OE conditions.

amplitude decreases (Fig. 7B) as a result of RyR phosphorylation that enhances the Ca leak thus decreasing the SR Ca content. The same relation has been experimentally observed (Maier *et al.*, 2003; Dybkova *et al.*, 2011). In agreement with experimental data (Dybkova *et al.*, 2011), $[Ca]_i$ decay is slower (Fig. 7C), but FDAR is enhanced by CaMKII-OE effect on

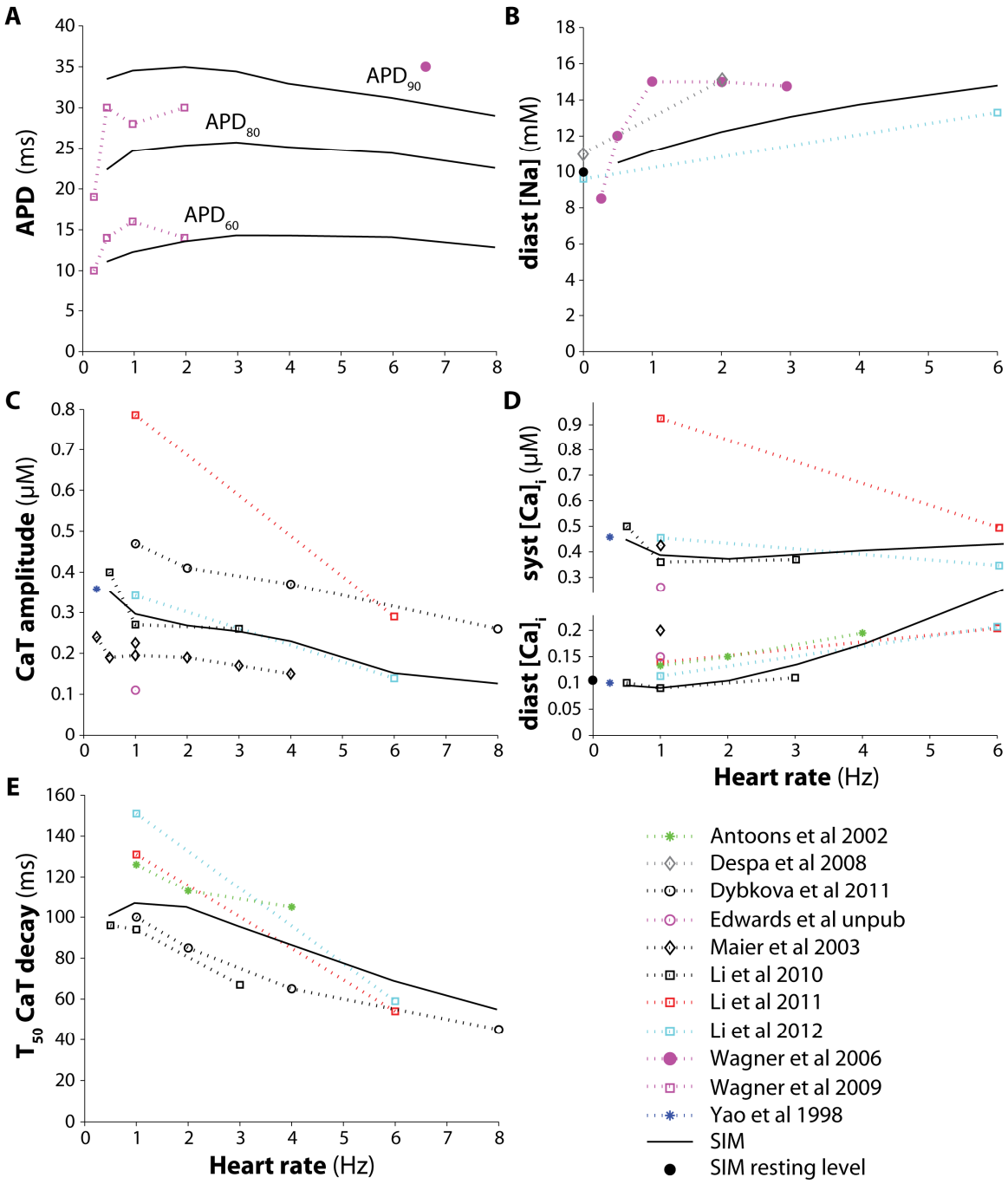

Figure 6. Validation of the model in control condition against a set of experimental data measured at different pacing rates. Experimental (symbols) and simulated (solid lines) APD (panel A), diastolic [Na] (B), CaT amplitude (C), diastolic and systolic $[Ca]_i$ (D), time to half $[Ca]_i$ decay (E). All the simulated results have been obtained after pacing the digital cell at indicated frequencies until steady-state condition. APD_X was measured as the interval between AP upstroke and X% repolarization level. Experimental data from (Yao *et al.*, 1998; Antoons *et al.*, 2002; Maier *et al.*, 2003; Wagner *et al.*, 2006; Despa *et al.*, 2008; Wagner *et al.*, 2009; Li *et al.*, 2010; Dybkova *et al.*, 2011; Li *et al.*, 2011; Li *et al.*, 2012; Edwards *et al.*, unpub.).

PLB. Fig. 7C shows that the model fails to reflect the increase in [Na] (Wagner *et al.*, 2006), revealing an aspect where our quantitative knowledge is complete.

Consequences of βAR stimulation

The effect of βAR stimulation has been investigated by simulating the application of 100 nM ISO. Fig. 8A shows the ISO-induced rise of cAMP, the second messenger that mediates the βAR-induced PKA activation. The model reproduces experimental data about Ca and Na handling (Despa *et al.*, 2008): CaT amplitude increases (Fig. 8B), due to phosphorylation at LTCC, RyR and PLB, and diastolic [Na] decreases (Fig. 8C) as consequence of PLM phosphorylation.

We compared the effect of PKA activation in WT and CaMKII-OE conditions, by simulating a 120 s long ISO application during 1 Hz stimulation. In agreement with the experimental findings (Edwards *et al.*, unpub.) reported in Fig. 9A, the model predicts AP prolongation (Fig. 9B), mainly due to the PKA-induced increase of I_{Ca}. Our simulations confirm the decrease in the diastolic $[Ca]_i$ and the increase in CaT amplitude (Fig. 9C). As

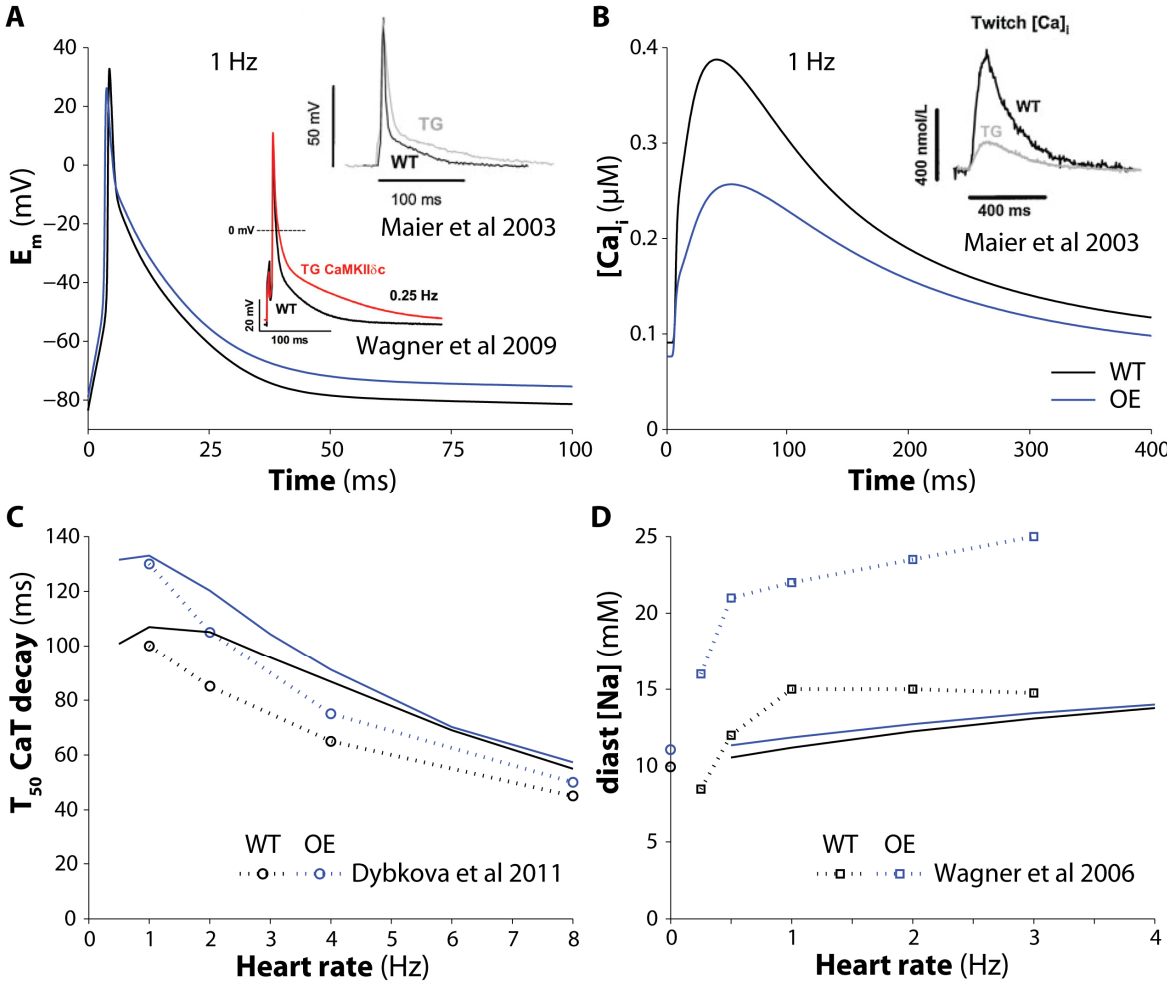

Figure 7. Effect of 6-fold CaMKII overexpression. Simulated AP (panel A) and CaT (B) obtained in control and CaMKII-OE conditions pacing the virtual cell at 1 Hz; insets show analogous experimental recordings. Experimental (symbols) and simulated (solid lines) time to half $[Ca]_i$ decay (C) and diastolic [Na] (D) at different pacing rates. Experimental data from (Maier *et al.*, 2003; Wagner *et al.*, 2006; Wagner *et al.*, 2009; Dybkova *et al.*, 2011).

observed in experiments, $[Ca]_i$ decay is faster during ISO application, due to phosphorylation of PLB.

When simulating the PKA activation in CaMKII-OE condition, the model predicts the development of delayed afterdepolarizations (DADs, Fig. 10A, black), due to spontaneous SR Ca release caused by PKA-induced RyR hyperactivity. This increases $[Ca]_i$ (Fig. 10B, black) and thus triggers NCX inward current (I_{NaCa}, Fig. 10C) that depolarizes the membrane. DADs are present both during stimulated beats and when the stimulation is interrupted (Fig. 10A, grey). The model does not predict this behavior when simulating the same protocol in WT condition (not shown).

DISCUSSION

In the present study we developed a novel model of murine ventricular ECC, which integrates a detailed Ca-CaM-CaMKII-CaN model (Saucerman & Bers, 2008) and the most recent model of PKA-dependent regulation of ECC (Yang & Saucerman, 2012) into a strongly validated AP model (Shannon *et al.*, 2004). This is the first model of mouse AP where the two pathways are integrated and are described by a fully ODEs system. Our model has been identified in the control condition using experimental data recorded (or scaled) at physiological temperature, and it faithfully reproduces the frequency response of the main features characterizing the mouse myocyte AP and Ca and Na dynamics (Fig. 6).

The models also well reproduces the effects of a 6-fold CaMKII-OE (Fig. 7), except the observed increase in [Na] in transgenic *vs*. WT mice (Fig. 7D). Although CaMKII-OE increases late I_{Na} and sarcolemmal Na leak, these effects are not sufficient to appreciably elevate [Na]. This issue has been previously discussed by the Maier and Bers groups (Wagner

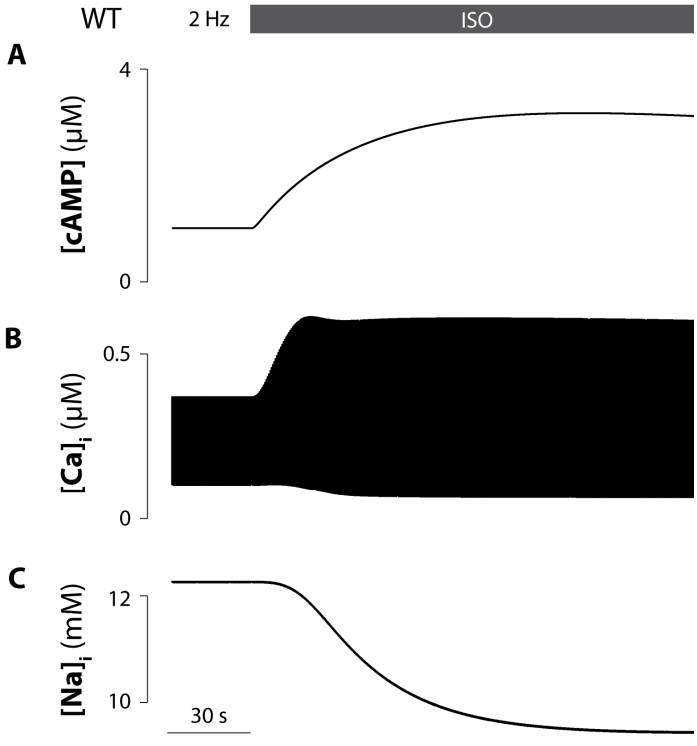

Figure 8. Time course of PKA activation. Time course of [cAMP] (panel A), $[Ca]_i$ (B) and [Na] (C) obtained by stimulating the virtual cell at 2 Hz in control condition and applying 100 nM ISO after 30 s.

et al., 2011). In their study the authors aimed to investigate the role of reactive oxygen species (ROS) in the contest of HF in mouse. They integrated into the Shannon-Bers model the ROS-induced increase in late I_{Na}, without obtaining a significant increase in [Na], as shown in their Online Fig. 1. This may indicate that other mechanisms/pathways are responsible for the increase in [Na].

The model well reproduces the effect of 100 nM ISO application (Fig. 8 and Fig. 9) on AP and CaT in both control and CaMKII-OE conditions. Moreover, arrhythmogenic activity is predicted with contemporary CaMKII and PKA activation: our model shows the development of DAD due to spontaneous Ca release from the SR (Fig. 10). In analogous experiments (Edwards *et al.*, unpub.), it has been observed the development of early afterdepolarizations (EADs, Fig. 11A and C), that are abolished when the SR Ca release is prevented by caffeine application (Fig. 11E). It's interesting to underline the important role of SR Ca release in both simulated DADs and experimentally observed EADs. Our results suggest that this phenomenon may be the trigger mechanism also in the latter case. In our

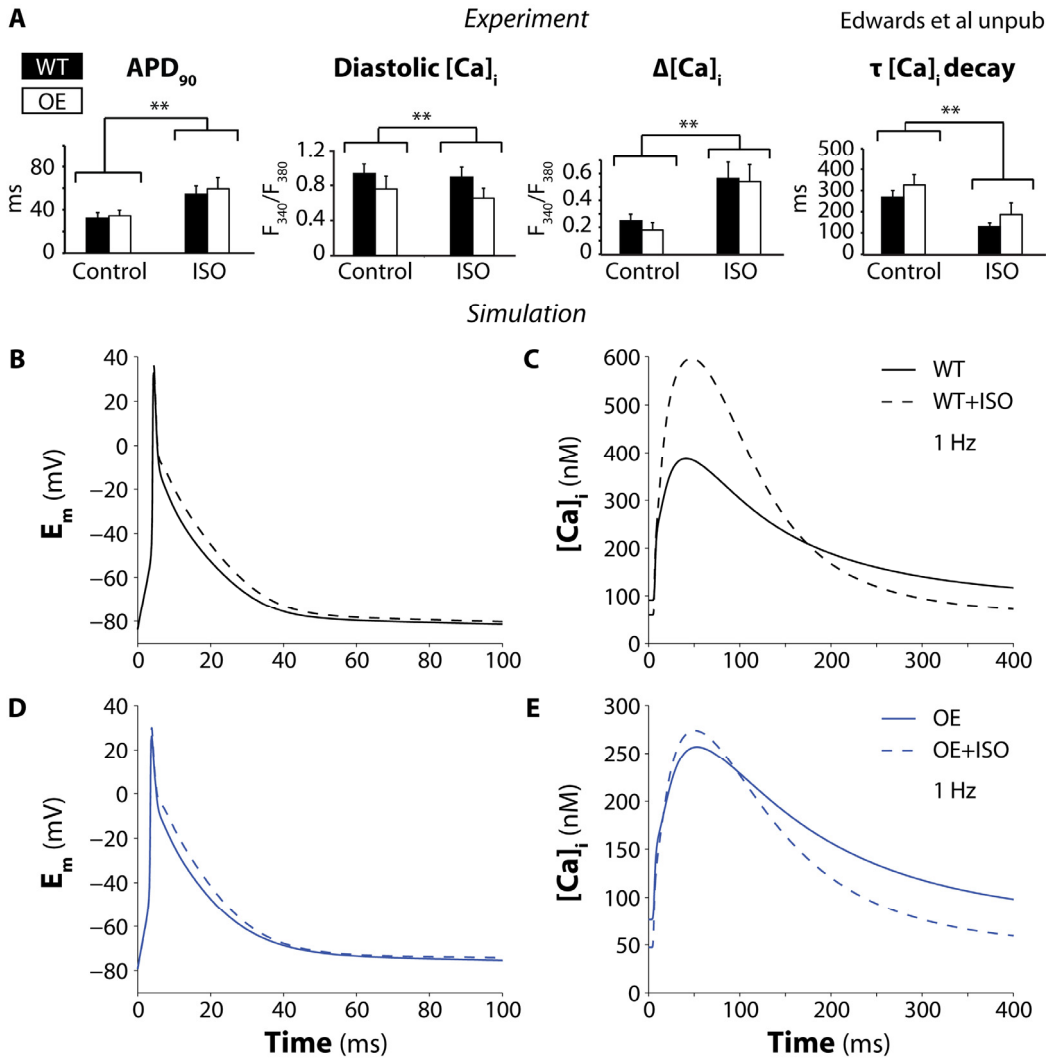

Figure 9. Effect of ISO application. Experimental data about ISO-induced changes in APD, diastolic $[Ca]_i$, CaT amplitude and time constant of $[Ca]_i$ decay from (Edwards *et al.*, unpub.) (panel A). Simulated AP (B, D) and CaT (C, E) obtained pacing the virtual cell at 1 Hz in absence of ISO (solid lines) and in presence of 100 nM ISO after a 120 s application (dashed) in WT and CaMKII-OE conditions.

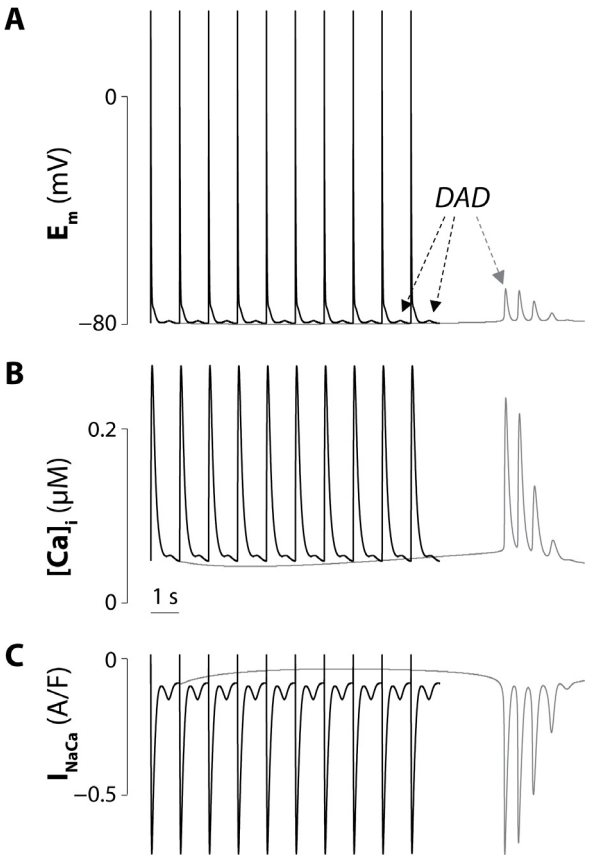

Figure 10. Simulated prediction of DADs occurrence as consequences of ISO application in CaMKII-OE condition. Simulated AP (panel A), CaT (B) and I_{NaCa} (C) obtained in presence of 100 nM ISO after a 120 s application (1 Hz). Black traces were obtained by continuing the stimulation with the same pacing rate, while grey traces were obtained by interrupting the stimulation after the first beat.

simulations SR Ca release (and consequent membrane depolarization) occurs only after the resting potential is reached, and this difference with experimental observations may be due to an overestimation of PKA effect on a repolarizing current or to an underestimation of the effect on a depolarizing current, which can delay the arrhythmogenic event occurrence.

Only by introducing drastic modifications (*e.g.*, block of repolarizing currents, increase in Ca influx and decrease of pacing frequency), our model reproduces EADs (Fig. 12A). EAD takeoff is due to spontaneous SR Ca release (Fig. 12B) that causes augmented Ca extrusion via NCX. If the depolarization is weak, both E_m and $[Ca]_i$ smoothly come back to the resting value (first beat). On the contrary, if the amplitude is wide enough, I_{Ca} reactivates (Fig 12C, from second to last beat), facilitating E_m depolarization and triggering Ca-induced Ca release (CICR); I_{Ca} reactivation can also occur more times (*e.g.*, twice in the last beat). Our model predicts two different kinds of EAD, with and without I_{Ca} reactivation, as experimentally seen (Edwards *et al.*, unpub.). The first kind of EAD observed in experiments (Fig. 11A) is characterized by a sequence of I_{Ca} reactivations. The CaT shows the occurrence of several CICR events that forms a kind of plateau (Fig. 11B). The second kind of EAD is characterized by more negative take-off potentials (Fig. 11C), any I_{Ca} reactivation and no CICR. The CaT decay is smooth (Fig. 11D).

EADs commonly occur during the plateau phase of the AP, where the balance of repolarizing and depolarizing currents keeps E_m almost unchanged. A little prolongation of the AP may be sufficient to lead to the I_{Ca} reactivation that can easily depolarize the membrane. The particular morphology of the murine AP does not facilitate the occurrence of EAD: the plateau is absent and the repolarization proceeds unhindered. While EADs have been often reproduced in many computational studies with AP models of other species, none

of the mouse AP models described in literature has been applied to study these arrhythmogenic events, proof of the difficulty of reproducing EADs with these models. In fact, mouse models have been used to study the differences between apex and septum (Bondarenko *et al.*, 2004), or between adult and neonatal cell (Wang & Sobie, 2008). Others studies investigated the effect of CaMKII phosphorylation (Koivumaki *et al.*, 2009), the implications of cardiac NCX overexpression (Li *et al.*, 2010) and of SERCA knockout (Li *et al.*, 2011; Li *et al.*, 2012), or studied the implications of PLM knockout (Yang & Saucerman, 2012). None of these studies showed the simulated development of EADs or DADs.

In the past two decades CaMKII has been recognized as being a potential proarrhythmic signaling molecule and it has been causally linked to the initiation of triggered arrhythmias via both EADs and DADs in mice and other mammals (Anderson, 2007). It is assumed that CaMKII-dependent EADs would be attributed to the CaMKII-induced increase in late I_{Na} or by reactivating I_{Ca}, but whether and how these effects quantitatively account for EADs is not known. CaMKII effects on RyR increase the propensity for Ca sparks and waves (Maier *et al.*, 2003) and these are fundamental events underlying arrhythmogenic DADs. In HF, where the NCX may be upregulated (Schillinger *et al.*, 2003) and I_{K1} downregulated

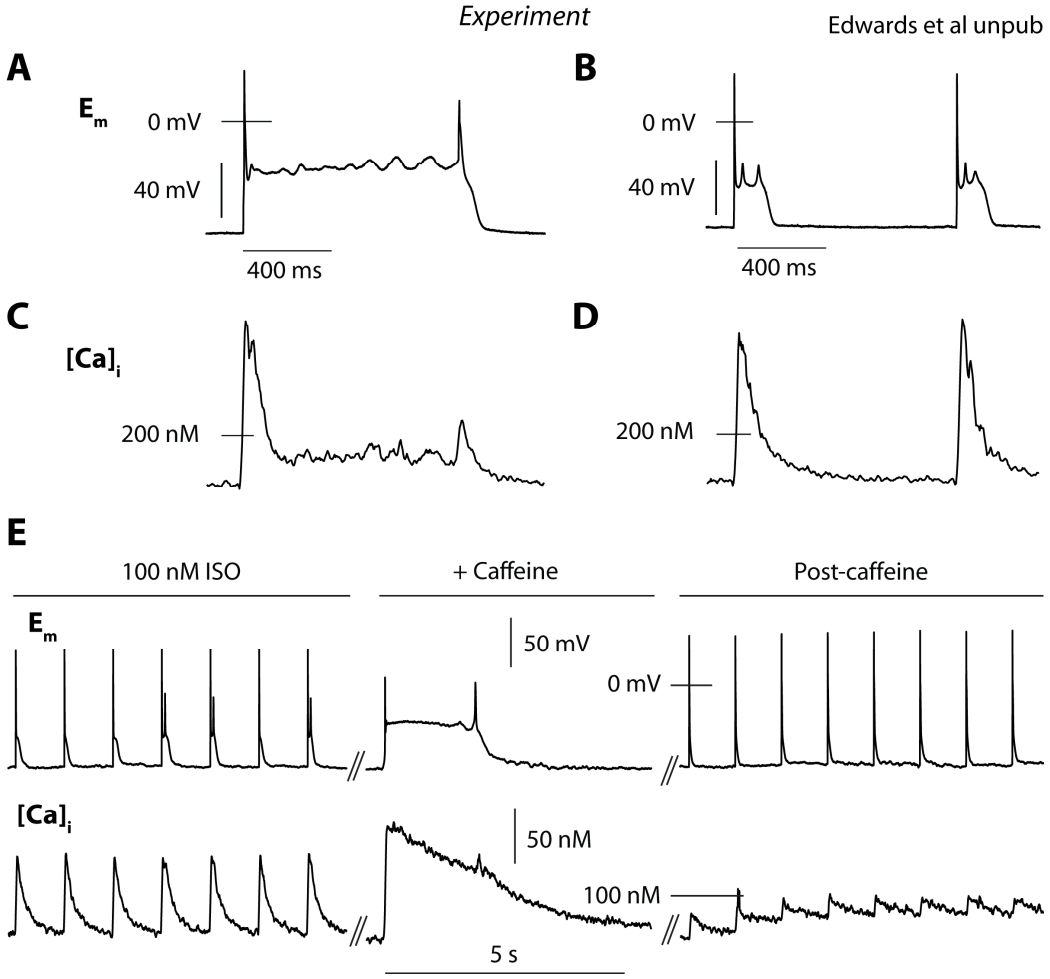

Figure 11. Experimental observation of EAD as consequences of ISO application in CaMKII-OE mice. Different kinds of EAD (panels A, C) and corresponding CaT (B, D) experimentally obtained after 100 nM ISO application (Edwards *et al.*, unpub.). EADs are abolished when the SR Ca release is prevented by caffeine application (E).

(possibly mediated by CaMKII), a given SR Ca release also produces a larger depolarizing current and DAD, and the threshold Ca release required to trigger an AP is greatly reduced (Pogwizd *et al.*, 2001). It is unknown which of these potential CaMKII effects is predominant in causing these arrhythmias, or how they interact with other alterations in failing myocytes to increase arrhythmia risk in HF (Pogwizd & Bers, 2004). In this intrigued context, the use of mathematical models may be helpful to discriminate the potential effect of the phosphorylation of each target, so our model can provide an useful tool to assess which CaMKII targets are most arrhythmogenic.

There is compelling evidence that CaMKII is a critical downstream target of βAR activation in the process of adrenergic-induced hypertrophy and HF (Zhang *et al.*, 2005): since CaMKII activity responds to the frequency and magnitude of Ca signals, CaMKII is influenced via PKA-dependent enhancement of I_{Ca} and SR Ca uptake and, consequently, release. However, the details of how the βAR stimulation and CaMKII network interact has not been systematically modeled, since there is evidence for a Ca- and PKA-independent pathway by which βAR stimulation causes CaMKII activation, RyR activation, inotropy and apoptosis (Grimm & Brown, 2010). βAR-induced PKA activation is mediated by cAMP, that can also activate the guanine nucleotide exchange factor Epac (independent of PKA) to activate CaMKII and RyR-dependent SR Ca leak (Pereira *et al.*, 2007), and this interaction has been reported to mediate βAR-induced cardiac hypertrophy (Metrich *et al.*, 2008). Moreover, it has been shown that the βAR activation of CaMKII, which is Ca- and PKA-independent, is also cAMP-independent (Curran *et al.*, 2007). It has also been shown that

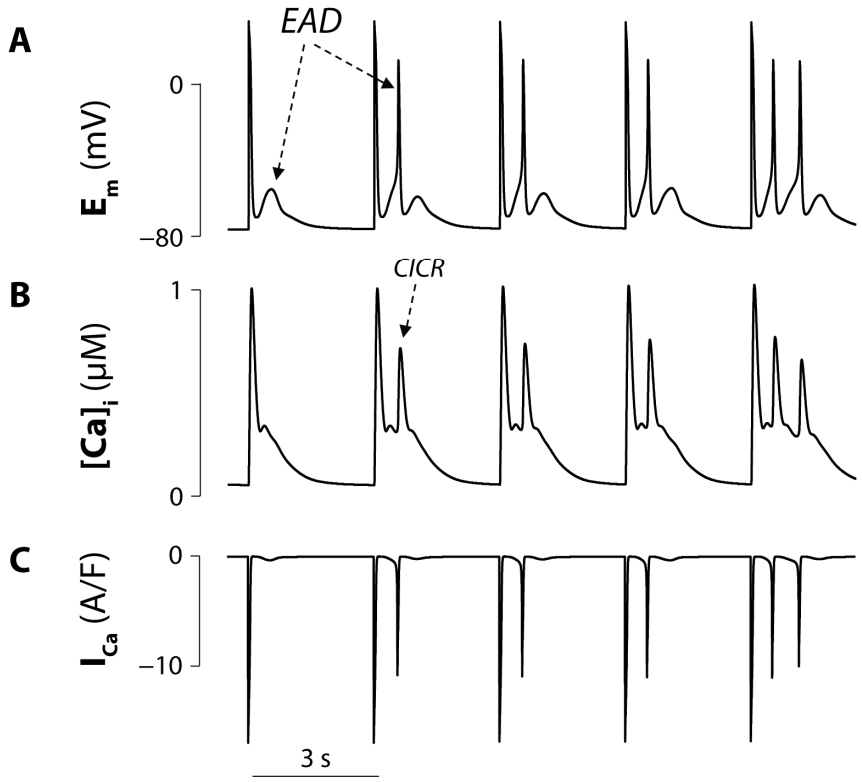

Figure 12. Simulation of EADs. Simulated E_m (panel A), CaT (B) and I_{Ca} (C) obtained during a 100 nM ISO application at a pacing rate of 0.33 Hz. Repolarizing currents were drastically reduced and conductance of I_{Ca} and background I_{Na} increased.

ROS, increased in HF, can contribute to increase late I_{Na} (leading to intracellular Na accumulation and arrhythmias), and, above all, can activate CaMKII via oxidation (Erickson *et al.*, 2008). Given the complexity of this system and of all the mechanisms involved, it is hard to imagine to integrate detailed descriptions of all these pathways in our model, that could be certainly extended and improved. Rather, our model could provide an useful tool for experiment planning, since preliminary results obtained by integrating simplified effect could give rise to hypotheses and address future experimental work.

Conclusion

A novel model of murine ECC has been identified at physiological temperature and validated at baseline. It improves existing murine AP models by including the most recent descriptions of CaMKII (Saucerman & Bers, 2008) and PKA (Yang & Saucerman, 2012) signaling pathways. This allowed investigating the effects of contemporary activation of the two pathways and showing how PKA activation results in triggered activity in the context of CaMKII-OE.

We conclude that our model is a useful quantitative tool to examine at the single cell level how CaMKII and PKA signaling pathways interact to coordinate ECC in the context of HF. For example, it can be used to test which CaMKII targets are most arrhythmogenic or to assess the effects of acute *vs*. chronic CaMKII hyperactivity. Given its computational tractability, it could be incorporated in tissue-scale/whole heart models to test how these cellular instabilities can induce arrhythmias. This model could also be an useful tool for the potential interaction with experiment planning. Moreover, a systematic framework accounting for electrophysiological differences among species could be developed to extrapolate findings in the genetically engineered mice to the clinical setting.

Further work will be required to incorporate modulation of CaMKII by other mechanisms involved in its regulation, such as ROS activation and βAR-induced Ca- and PKA-independent activation pathways.

Acknowledgements

We wish to thank Dr. J. M. Nerbonne for sharing unpublished data about I_{Kur} inactivation and for helpful discussion.

References

Ai X, Curran JW, Shannon TR, Bers DM & Pogwizd SM. (2005). Ca2+/calmodulin-dependent protein kinase modulates cardiac ryanodine receptor phosphorylation and sarcoplasmic reticulum Ca2+ leak in heart failure. *Circulation research* **97,** 1314-1322.

Anderson ME. (2007). Multiple downstream proarrhythmic targets for calmodulin kinase II: moving beyond an ion channel-centric focus. *Cardiovascular research* **73,** 657-666.

Antoons G, Mubagwa K, Nevelsteen I & Sipido KR. (2002). Mechanisms underlying the frequency dependence of contraction and [Ca(2+)](i) transients in mouse ventricular myocytes. *The Journal of physiology* **543,** 889-898.

Berry RG, Despa S, Fuller W, Bers DM & Shattock MJ. (2007). Differential distribution and regulation of mouse cardiac Na+/K+-ATPase alpha1 and alpha2 subunits in T-tubule and surface sarcolemmal membranes. *Cardiovascular research* **73,** 92-100.

Bers DM. (2001). *Excitation-contraction coupling and cardiac contractile force*. Kluwer Academic Publishers, Dordrecht ; Boston.

Bers DM & Grandi E. (2009). Calcium/calmodulin-dependent kinase II regulation of cardiac ion channels. *Journal of cardiovascular pharmacology* **54,** 180-187.

Bondarenko VE, Szigeti GP, Bett GC, Kim SJ & Rasmusson RL. (2004). Computer model of action potential of mouse ventricular myocytes. *American journal of physiology Heart and circulatory physiology* **287,** H1378-1403.

Breckenridge R. (2010). Heart failure and mouse models. *Disease models & mechanisms* **3,** 138-143.

Brouillette J, Clark RB, Giles WR & Fiset C. (2004). Functional properties of K+ currents in adult mouse ventricular myocytes. *The Journal of physiology* **559,** 777-798.

Brouillette J, Trepanier-Boulay V & Fiset C. (2003). Effect of androgen deficiency on mouse ventricular repolarization. *The Journal of physiology* **546,** 403-413.

Brunet S, Aimond F, Li H, Guo W, Eldstrom J, Fedida D, Yamada KA & Nerbonne JM. (2004). Heterogeneous expression of repolarizing, voltage-gated K+ currents in adult mouse ventricles. *The Journal of physiology* **559,** 103-120.

Curran J, Hinton MJ, Rios E, Bers DM & Shannon TR. (2007). Beta-adrenergic enhancement of sarcoplasmic reticulum calcium leak in cardiac myocytes is mediated by calcium/calmodulin-dependent protein kinase. *Circulation research* **100,** 391-398.

Demir S. (2005). Simulating cardiac ventricular action potentials in rat and mouse. *Conference proceedings : Annual International Conference of the IEEE Engineering in Medicine and Biology Society IEEE Engineering in Medicine and Biology Society Conference* **1,** 130-132.

Despa S, Bossuyt J, Han F, Ginsburg KS, Jia LG, Kutchai H, Tucker AL & Bers DM. (2005). Phospholemman-phosphorylation mediates the beta-adrenergic effects on Na/K pump function in cardiac myocytes. *Circulation research* **97,** 252-259.

Despa S, Islam MA, Pogwizd SM & Bers DM. (2002). Intracellular [Na+] and Na+ pump rate in rat and rabbit ventricular myocytes. *The Journal of physiology* **539,** 133-143.

Despa S, Tucker AL & Bers DM. (2008). Phospholemman-mediated activation of Na/K-ATPase limits [Na]i and inotropic state during beta-adrenergic stimulation in mouse ventricular myocytes. *Circulation* **117,** 1849-1855.

Dybkova N, Sedej S, Napolitano C, Neef S, Rokita AG, Hunlich M, Brown JH, Kockskamper J, Priori SG, Pieske B & Maier LS. (2011). Overexpression of CaMKIIdeltac in RyR2R4496C+/- knock-in mice leads to altered intracellular Ca2+ handling and increased mortality. *Journal of the American College of Cardiology* **57,** 469-479.

Edwards AG, Hake JE, Patel S, Li P, Westenbrink DB, Grandi E, Bers DM, Omens JH, Brown JH & McCulloch AD. (unpub.). Mechanisms of early afterdepolarizations prior to heart failure in the CaMKIIδc transgenic mouse. In preparation.

Erickson JR, Joiner ML, Guan X, Kutschke W, Yang J, Oddis CV, Bartlett RK, Lowe JS, O'Donnell SE, Aykin-Burns N, Zimmerman MC, Zimmerman K, Ham AJ, Weiss RM, Spitz DR, Shea MA, Colbran RJ, Mohler PJ & Anderson ME. (2008). A dynamic pathway for calcium-independent activation of CaMKII by methionine oxidation. *Cell* **133,** 462-474.

Grandi E & Bers DM. (in press). Models of the Ventricular Action Potential in Health and Disease. In *Cardiac Electrophysiology: From Cell to Bedside*, 6th edn, ed. Zipes DP & Jalife J. Expert Consult.

Grandi E, Puglisi JL, Wagner S, Maier LS, Severi S & Bers DM. (2007). Simulation of Ca-calmodulin-dependent protein kinase II on rabbit ventricular myocyte ion currents and action potentials. *Biophysical journal* **93,** 3835-3847.

Grimm M & Brown JH. (2010). Beta-adrenergic receptor signaling in the heart: role of CaMKII. *Journal of molecular and cellular cardiology* **48,** 322-330.

Guo T, Zhang T, Mestril R & Bers DM. (2006). Ca2+/Calmodulin-dependent protein kinase II phosphorylation of ryanodine receptor does affect calcium sparks in

mouse ventricular myocytes. *Circulation research* **99,** 398-406.

Guo W, Xu H, London B & Nerbonne JM. (1999). Molecular basis of transient outward K+ current diversity in mouse ventricular myocytes. *The Journal of physiology* **521 Pt 3,** 587-599.

Hoch B, Meyer R, Hetzer R, Krause EG & Karczewski P. (1999). Identification and expression of delta-isoforms of the multifunctional Ca2+/calmodulin-dependent protein kinase in failing and nonfailing human myocardium. *Circulation research* **84,** 713-721.

Hund TJ & Rudy Y. (2004). Rate dependence and regulation of action potential and calcium transient in a canine cardiac ventricular cell model. *Circulation* **110,** 3168-3174.

Iribe G, Kohl P & Noble D. (2006). Modulatory effect of calmodulin-dependent kinase II (CaMKII) on sarcoplasmic reticulum Ca2+ handling and interval-force relations: a modelling study. *Philosophical transactions Series A, Mathematical, physical, and engineering sciences* **364,** 1107-1133.

Jessup M & Brozena S. (2003). Heart failure. *The New England journal of medicine* **348,** 2007-2018.

Kaese S & Verheule S. (2012). Cardiac electrophysiology in mice: a matter of size. *Frontiers in physiology* **3,** 345.

Knollmann BC, Knollmann-Ritschel BE, Weissman NJ, Jones LR & Morad M. (2000). Remodelling of ionic currents in hypertrophied and failing hearts of transgenic mice overexpressing calsequestrin. *The Journal of physiology* **525 Pt 2,** 483-498.

Kohlhaas M, Zhang T, Seidler T, Zibrova D, Dybkova N, Steen A, Wagner S, Chen L, Brown JH, Bers DM & Maier LS. (2006). Increased sarcoplasmic reticulum calcium leak but unaltered contractility by acute CaMKII overexpression in isolated rabbit cardiac myocytes. *Circulation research* **98,** 235-244.

Koivumaki JT, Korhonen T, Takalo J, Weckstrom M & Tavi P. (2009). Regulation of excitation-contraction coupling in mouse cardiac myocytes: integrative analysis with mathematical modelling. *BMC physiology* **9,** 16.

Li GR, Feng J, Wang Z, Fermini B & Nattel S. (1996). Adrenergic modulation of ultrarapid delayed rectifier K+ current in human atrial myocytes. *Circulation research* **78,** 903-915.

Li L, Chu G, Kranias EG & Bers DM. (1998). Cardiac myocyte calcium transport in phospholamban knockout mouse: relaxation and endogenous CaMKII effects. *The American journal of physiology* **274,** H1335-1347.

Li L, Louch WE, Niederer SA, Andersson KB, Christensen G, Sejersted OM & Smith NP. (2011). Calcium dynamics in the ventricular myocytes of SERCA2 knockout mice: A modeling study. *Biophysical journal* **100,** 322-331.

Li L, Louch WE, Niederer SA, Aronsen JM, Christensen G, Sejersted OM & Smith NP. (2012). Sodium accumulation in SERCA knockout-induced heart failure. *Biophysical journal* **102,** 2039-2048.

Li L, Niederer SA, Idigo W, Zhang YH, Swietach P, Casadei B & Smith NP. (2010). A mathematical model of the murine ventricular myocyte: a data-driven biophysically based approach applied to mice overexpressing the canine NCX isoform. *American journal of physiology Heart and circulatory physiology* **299,** H1045-1063.

Livshitz LM & Rudy Y. (2007). Regulation of Ca2+ and electrical alternans in cardiac myocytes: role of CAMKII and repolarizing currents. *American journal of physiology Heart and circulatory physiology* **292,** H2854-2866.

Lloyd-Jones D, Adams R, Carnethon M, De Simone G, Ferguson TB, Flegal K, Ford E, Furie K, Go A, Greenlund K, Haase N, Hailpern S, Ho M, Howard V, Kissela B, Kittner S, Lackland D, Lisabeth L, Marelli A, McDermott M, Meigs J, Mozaffarian D, Nichol G, O'Donnell C, Roger V, Rosamond W, Sacco R, Sorlie P, Stafford R, Steinberger J, Thom T, Wasserthiel-Smoller S, Wong N, Wylie-Rosett J & Hong Y. (2009). Heart disease and stroke statistics--2009 update: a report from the American Heart Association Statistics Committee and Stroke Statistics Subcommittee. *Circulation* **119,** 480-486.

Maier LS & Bers DM. (2007). Role of Ca2+/calmodulin-dependent protein kinase

(CaMK) in excitation-contraction coupling in the heart. *Cardiovascular research* **73,** 631-640.

Maier LS, Zhang T, Chen L, DeSantiago J, Brown JH & Bers DM. (2003). Transgenic CaMKIIdeltaC overexpression uniquely alters cardiac myocyte Ca2+ handling: reduced SR Ca2+ load and activated SR Ca2+ release. *Circulation research* **92,** 904-911.

McMurray JJ & Pfeffer MA. (2005). Heart failure. *Lancet* **365,** 1877-1889.

McMurray JJ & Stewart S. (2000). Epidemiology, aetiology, and prognosis of heart failure. *Heart* **83,** 596-602.

Metrich M, Lucas A, Gastineau M, Samuel JL, Heymes C, Morel E & Lezoualc'h F. (2008). Epac mediates beta-adrenergic receptor-induced cardiomyocyte hypertrophy. *Circulation research* **102,** 959-965.

Nerbonne JM. (2004). Studying cardiac arrhythmias in the mouse--a reasonable model for probing mechanisms? *Trends in cardiovascular medicine* **14,** 83-93.

Odermatt A, Kurzydlowski K & MacLennan DH. (1996). The vmax of the Ca2+-ATPase of cardiac sarcoplasmic reticulum (SERCA2a) is not altered by Ca2+/calmodulin-dependent phosphorylation or by interaction with phospholamban. *The Journal of biological chemistry* **271,** 14206-14213.

Page E & Surdyk-Droske M. (1979). Distribution, surface density, and membrane area of diadic junctional contacts between plasma membrane and terminal cisterns in mammalian ventricle. *Circulation research* **45,** 260-267.

Pereira L, Metrich M, Fernandez-Velasco M, Lucas A, Leroy J, Perrier R, Morel E, Fischmeister R, Richard S, Benitah JP, Lezoualc'h F & Gomez AM. (2007). The cAMP binding protein Epac modulates Ca2+ sparks by a Ca2+/calmodulin kinase signalling pathway in rat cardiac myocytes. *The Journal of physiology* **583,** 685-694.

Pogwizd SM & Bers DM. (2004). Cellular basis of triggered arrhythmias in heart failure. *Trends in cardiovascular medicine* **14,** 61-66.

Pogwizd SM, Schlotthauer K, Li L, Yuan W & Bers DM. (2001). Arrhythmogenesis and contractile dysfunction in heart failure: Roles of sodium-calcium exchange, inward rectifier potassium current, and residual beta-adrenergic responsiveness. *Circulation research* **88,** 1159-1167.

Sag CM, Wadsack DP, Khabbazzadeh S, Abesser M, Grefe C, Neumann K, Opiela MK, Backs J, Olson EN, Brown JH, Neef S, Maier SK & Maier LS. (2009). Calcium/calmodulin-dependent protein kinase II contributes to cardiac arrhythmogenesis in heart failure. *Circulation Heart failure* **2,** 664-675.

Satoh H, Delbridge LM, Blatter LA & Bers DM. (1996). Surface:volume relationship in cardiac myocytes studied with confocal microscopy and membrane capacitance measurements: species-dependence and developmental effects. *Biophysical journal* **70,** 1494-1504.

Saucerman JJ & Bers DM. (2008). Calmodulin mediates differential sensitivity of CaMKII and calcineurin to local Ca2+ in cardiac myocytes. *Biophysical journal* **95,** 4597-4612.

Saucerman JJ, Brunton LL, Michailova AP & McCulloch AD. (2003). Modeling beta-adrenergic control of cardiac myocyte contractility in silico. *The Journal of biological chemistry* **278,** 47997-48003.

Saucerman JJ, Healy SN, Belik ME, Puglisi JL & McCulloch AD. (2004). Proarrhythmic consequences of a KCNQ1 AKAP-binding domain mutation: computational models of whole cells and heterogeneous tissue. *Circulation research* **95,** 1216-1224.

Saucerman JJ & McCulloch AD. (2004). Mechanistic systems models of cell signaling networks: a case study of myocyte adrenergic regulation. *Progress in biophysics and molecular biology* **85,** 261-278.

Schillinger W, Fiolet JW, Schlotthauer K & Hasenfuss G. (2003). Relevance of Na+-Ca2+ exchange in heart failure. *Cardiovascular research* **57,** 921-933.

Shannon TR, Wang F, Puglisi J, Weber C & Bers DM. (2004). A mathematical treatment of integrated Ca dynamics within the ventricular myocyte. *Biophysical journal* **87,** 3351-3371.

Shin SY, Choo SM, Woo SH & Cho KH. (2008). Cardiac systems biology and parameter sensitivity analysis: intracellular Ca2+ regulatory mechanisms in mouse ventricular myocytes. *Advances in biochemical engineering/biotechnology* **110,** 25-45.

Soltis AR & Saucerman JJ. (2010). Synergy between CaMKII substrates and beta-adrenergic signaling in regulation of cardiac myocyte Ca(2+) handling. *Biophysical journal* **99,** 2038-2047.

Stanley WC, Recchia FA & Lopaschuk GD. (2005). Myocardial substrate metabolism in the normal and failing heart. *Physiological reviews* **85,** 1093-1129.

Su Z, Zou A, Nonaka A, Zubair I, Sanguinetti MC & Barry WH. (1998). Influence of prior Na+ pump activity on pump and Na+/Ca2+ exchange currents in mouse ventricular myocytes. *The American journal of physiology* **275,** H1808-1817.

Wagner S, Dybkova N, Rasenack EC, Jacobshagen C, Fabritz L, Kirchhof P, Maier SK, Zhang T, Hasenfuss G, Brown JH, Bers DM & Maier LS. (2006). Ca2+/calmodulin-dependent protein kinase II regulates cardiac Na+ channels. *The Journal of clinical investigation* **116,** 3127-3138.

Wagner S, Hacker E, Grandi E, Weber SL, Dybkova N, Sossalla S, Sowa T, Fabritz L, Kirchhof P, Bers DM & Maier LS. (2009). Ca/calmodulin kinase II differentially modulates potassium currents. *Circulation Arrhythmia and electrophysiology* **2,** 285-294.

Wagner S & Maier LS. (2006). Modulation of cardiac Na(+) and Ca(2+) currents by CaM and CaMKII. *Journal of cardiovascular electrophysiology* **17 Suppl 1,** S26-S33.

Wagner S, Ruff HM, Weber SL, Bellmann S, Sowa T, Schulte T, Anderson ME, Grandi E, Bers DM, Backs J, Belardinelli L & Maier LS. (2011). Reactive oxygen species-activated Ca/calmodulin kinase IIdelta is required for late I(Na) augmentation leading to cellular Na and Ca overload. *Circulation research* **108,** 555-565.

Wang L & Duff HJ. (1997). Developmental changes in transient outward current in mouse ventricle. *Circulation research* **81,** 120-127.

Wang LJ & Sobie EA. (2008). Mathematical model of the neonatal mouse ventricular action potential. *American journal of physiology Heart and circulatory physiology* **294,** H2565-2575.

Wang Y & Hill JA. (2010). Electrophysiological remodeling in heart failure. *Journal of molecular and cellular cardiology* **48,** 619-632.

Wehrens XH, Lehnart SE, Reiken SR & Marks AR. (2004). Ca2+/calmodulin-dependent protein kinase II phosphorylation regulates the cardiac ryanodine receptor. *Circulation research* **94,** e61-70.

Xu H, Guo W & Nerbonne JM. (1999). Four kinetically distinct depolarization-activated K+ currents in adult mouse ventricular myocytes. *The Journal of general physiology* **113,** 661-678.

Yang JH & Saucerman JJ. (2012). Phospholemman is a negative feed-forward regulator of Ca2+ in beta-adrenergic signaling, accelerating beta-adrenergic inotropy. *Journal of molecular and cellular cardiology* **52,** 1048-1055.

Yao A, Su Z, Nonaka A, Zubair I, Lu L, Philipson KD, Bridge JH & Barry WH. (1998). Effects of overexpression of the Na+-Ca2+ exchanger on [Ca2+]i transients in murine ventricular myocytes. *Circulation research* **82,** 657-665.

Yuan W & Bers DM. (1994). Ca-dependent facilitation of cardiac Ca current is due to Ca-calmodulin-dependent protein kinase. *The American journal of physiology* **267,** H982-993.

Zhang R, Khoo MS, Wu Y, Yang Y, Grueter CE, Ni G, Price EE, Jr., Thiel W, Guatimosim S, Song LS, Madu EC, Shah AN, Vishnivetskaya TA, Atkinson JB, Gurevich VV, Salama G, Lederer WJ, Colbran RJ & Anderson ME. (2005). Calmodulin kinase II inhibition protects against structural heart disease. *Nature medicine* **11,** 409-417.

Zhang T, Maier LS, Dalton ND, Miyamoto S, Ross J, Jr., Bers DM & Brown JH. (2003). The deltaC isoform of CaMKII is activated in cardiac hypertrophy and induces dilated cardiomyopathy and heart failure. *Circulation research* **92,** 912-919.

Zhou J, Jeron A, London B, Han X & Koren G. (1998). Characterization of a slowly

inactivating outward current in adult mouse ventricular myocytes. *Circulation research* **83,** 806-814.

Zhou J, Kodirov S, Murata M, Buckett PD, Nerbonne JM & Koren G. (2003). Regional upregulation of Kv2.1-encoded current, IK,slow2, in Kv1DN mice is abolished by crossbreeding with Kv2DN mice. *American journal of physiology Heart and circulatory physiology* **284,** H491-500.

CONCLUSION

My research activity has been focusing on the development of mathematical tools for investigating the mechanisms underlying ventricular excitation-contraction coupling (ECC), that is the process linking the electrical behavior of the membrane to the mechanical contraction of the myofilaments in myocytes (Bers, 2001), via the intracellular Ca signal. Three research projects have been presented in this thesis, in which computational modeling (at the single cell level) is applied to the study of cardiac electrophysiology.

The first study was aimed at simulating the effect of the Na channel blocker mexiletine on mutant cardiac Na current (I_{Na}), which led to unpredicted QT interval prolongation in a long QT syndrome type 3 (LQT3) patient (Ruan *et al.*, 2010). A Markov model of I_{Na} (Clancy & Rudy, 2002) was tuned to reproduce the experimentally observed effect of the F1473S Na channel mutation, and the modulatory effect of mexiletine. In collaboration with the Priori group, we provided evidence that this drug facilitates trafficking of the mutant Na channel (but not the wild type), thus prolonging QT interval and worsening arrhythmias. Our findings suggest that caution should be used when recommending Na channel blockers (commonly considered a gene-specific therapy for LQT3 patients) to carriers of mutations with undefined electrophysiological properties. We propose that functional characterization of mutant currents may guide mutation-specific treatment, and *in silico* analysis may be used to personalize therapy for LQT3 patients.

In the second project we studied the inactivation kinetics of the cardiac L-type Ca current (I_{Ca}), in order to faithfully describe the relative contributions of the two mechanisms of Ca- and voltage-dependent inactivation (CDI and VDI) (Grandi *et al.*, 2010; Morotti *et al.*, 2012). Moreover, the formulation of sarcoplasmic reticulum (SR) Ca release was modified to ensure proper Ca-dependent modulation of I_{Ca} inactivation at negative membrane potentials, where ECC gain is high. From our analysis we concluded that the inactivation of the non specific monovalent current (carried by Na and Cs) through LTCCs does not resemble VDI in physiological conditions. Next, we identified Markov model of I_{Ca} (Mahajan *et al.*, 2008) based on a broad range of experimental data on channel permeability and gating, and validated it against functional data in various homeostasis conditions. By taking into account a small contribution of ion-dependent inactivation (in addition to pure VDI) when Ba is the charge carrier, our model faithfully reproduced the relative importance of VDI and CDI to total I_{Ca} inactivation. Ba-dependent inactivation was usually neglected by other modeling studies and led to overestimation of VDI. Thus, we provided a useful tool to study the role of I_{Ca} kinetics during normal and altered repolarization.

β-adrenergic (βAR) and Ca-calmodulin dependent protein kinase (CaMKII) activation was modeled to understand how the crosstalk between these signaling pathways influences ECC in the context of heart failure (HF). This required the reparameterization of an action potential (AP) model, whereby cell geometry, ion currents, Ca and Na handling were adapted to murine electrophysiology. Furthermore, the regulatory effects of CaMKII signaling pathway and βAR activation were integrated into the AP model, based on existing descriptions (Saucerman & Bers, 2008; Yang & Saucerman, 2012). This provides a useful quantitative framework to examine how CaMKII and βAR signaling pathways interact to coordinate ECC and arrhythmias in the context of HF (*e.g.*, to test which CaMKII targets are most arrhythmogenic), and could serve as the basis for a systematic framework to extrapolate findings in animals to humans and the clinical setting.

In fact, while this last project was based on the development of a novel murine ECC model, a human model (ten Tusscher & Panfilov, 2006) was used to study the effects on the AP of the mutant I_{Na}, and a rabbit model (Shannon *et al.*, 2004) served as the basis for the study of I_{Ca} inactivation. The main differences between rabbit and mouse APs (and the underlying mechanisms) are described in detail in the third chapter. Briefly, mouse AP lacks a plateau phase, but exhibits rapid repolarization and very short AP duration (APD), if compared with the prominent plateau phase and long AP seen in rabbit (and in human as well). These differences are mainly due to different expression of membrane proteins (in particular, K channels). The development of this kind of species-specific models highlights marked electrophysiological differences among various species, which may underlie different arrhythmia mechanisms, and are crucial when trying to extrapolate experimental results in animals to human (*e.g.*, effect of disease-induced remodeling or response to drugs).

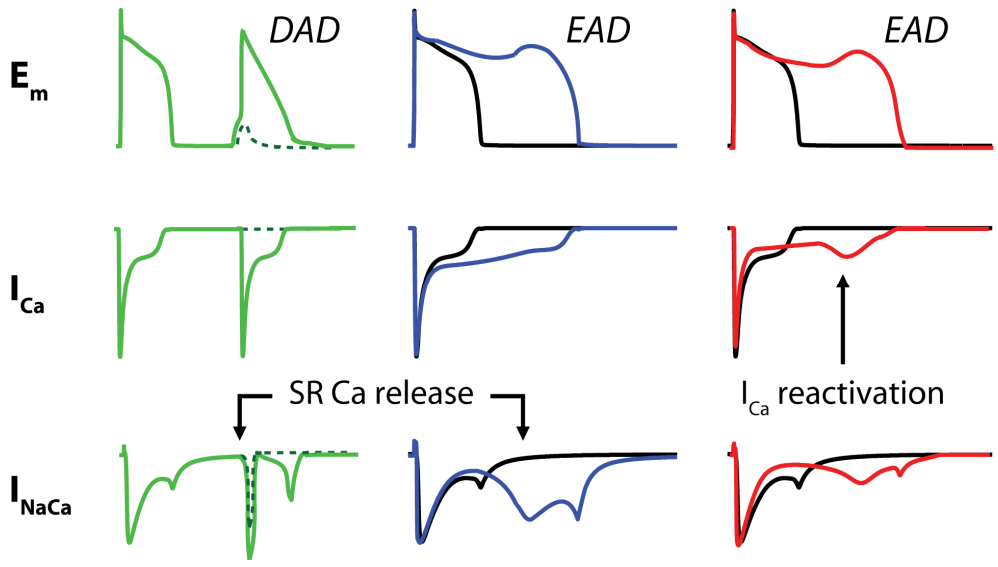

Figure 1. Mechanisms underlying afterdepolarizations. During the DAD (first column) SR Ca release activates I_{NaCa} that, in one case (solid line), is sufficient to bring the myocyte to the threshold and an AP can be triggered and, in the other case (dashed), is not. The second column shows a situation where the EAD is initiated by SR Ca release and NCX activity, while the EAD shown in the third column is initiated by I_{Ca} reactivation. Modified from (Bers, in press).

Ultimately, we aimed at using our computational methods to provide insights into the mechanisms underlying cardiac arrhythmias. When simulating the effects of the Na channel mutation F1473S, we predicted AP prolongation, which is associated with the prolongation of the QT interval seen on the patient's ECG (and characterizing the LQT3 phenotype). This AP prolongation (maximal at slow heart rates) facilitates the occurrence of early afterdepolarizations (EADs). In fact, long QT syndrome patients experience arrhythmogenic events preferentially at rest. Moreover, when simulating the effects of mexiletine administration, we observed further AP prolongation, leading to capture failures at fast heart rates.

We confirmed that LTCC inactivation is an important feedback mechanism that regulates Ca loading and duration of repolarization. When simulating the inhibition of VDI (in order to mimic Timothy syndrome), we obtained a prolongation of the AP. More drastic consequences were obtained when reducing CDI, thus suggesting that CDI is dominant (*vs*. VDI) in physiological conditions. We simulated the expression of a mutant calmodulin (unable to mediate CDI) and predicted the occurrence of phase 2 EADs. These have been commonly associated to I_{Ca} reactivation (January & Riddle, 1989; Luo & Rudy, 1994), but our modeling works showed that the reduction in CDI causes intracellular Ca overload and thus spontaneous SR Ca release, which enhances inward Na-Ca exchange current (I_{NaCa}) that depolarizes the membrane (Fig. 1, second column). The same triggering mechanism was found responsible for delayed afterdepolarizations (DADs) obtained by a further increase in mutant calmodulin expression (*i.e.* stronger inhibition of CDI) in rabbit, and by contemporary activation of βAR and CaMKII signaling pathways in our murine ECC model. Our LTCC model predicts phase 2 EADs due to I_{Ca} reactivation when simulating the effect of K currents block (Fig. 1, third column), as experimentally observed. In this case, the inhibition of repolarizing currents prolongs the AP, allowing the reactivation of some LTCCs and thus creating an inward current surge and net depolarization. We also demonstrated that the two triggering mechanisms are not mutually exclusive. For example, the SR Ca release-triggered NCX activity may produce only a very small depolarization that may then be amplified by recruiting I_{Ca} to cause a larger EAD, as we implied in simulating the crosstalk between βAR and CaMKII signaling in HF.

In conclusion, the present thesis shows how mathematical approach is suitable to provide new insights into the mechanisms controlling cardiac ECC in physiological and pathological conditions.

References

Bers DM. (2001). *Excitation-contraction coupling and cardiac contractile force*. Kluwer Academic Publishers, Dordrecht ; Boston.

Bers DM. (in press). Excitation-Contraction Coupling. In *Cardiac Electrophysiology: From Cell to Bedside*, 6th edn, ed. Zipes DP & Jalife J. Expert Consult.

Clancy CE & Rudy Y. (2002). Na(+) channel mutation that causes both Brugada and long-QT syndrome phenotypes: a simulation study of mechanism. *Circulation* **105,** 1208-1213.

Grandi E, Morotti S, Ginsburg KS, Severi S & Bers DM. (2010). Interplay of voltage and Ca-dependent inactivation of L-type Ca current. *Progress in biophysics and molecular biology* **103,** 44-50.

January CT & Riddle JM. (1989). Early afterdepolarizations: mechanism of

induction and block. A role for L-type Ca2+ current. *Circ Res* **64,** 977-990.

Luo CH & Rudy Y. (1994). A dynamic model of the cardiac ventricular action potential. II. Afterdepolarizations, triggered activity, and potentiation. *Circ Res* **74,** 1097-1113.

Mahajan A, Shiferaw Y, Sato D, Baher A, Olcese R, Xie LH, Yang MJ, Chen PS, Restrepo JG, Karma A, Garfinkel A, Qu Z & Weiss JN. (2008). A rabbit ventricular action potential model replicating cardiac dynamics at rapid heart rates. *Biophysical journal* **94,** 392-410.

Morotti S, Grandi E, Summa A, Ginsburg KS & Bers DM. (2012). Theoretical study of L-type Ca(2+) current inactivation kinetics during action potential repolarization and early afterdepolarizations. *The journal of physiology* **590,** 4465-4481.

Ruan Y, Denegri M, Liu N, Bachetti T, Seregni M, Morotti S, Severi S, Napolitano C & Priori SG. (2010). Trafficking defects and gating abnormalities of a novel SCN5A mutation question gene-specific therapy in long QT syndrome type 3. *Circulation research* **106,** 1374-1383.

Saucerman JJ & Bers DM. (2008). Calmodulin mediates differential sensitivity of CaMKII and calcineurin to local Ca2+ in cardiac myocytes. *Biophysical journal* **95,** 4597-4612.

Shannon TR, Wang F, Puglisi J, Weber C & Bers DM. (2004). A mathematical treatment of integrated Ca dynamics within the ventricular myocyte. *Biophysical journal* **87,** 3351-3371.

ten Tusscher KH & Panfilov AV. (2006). Alternans and spiral breakup in a human ventricular tissue model. *American journal of physiology Heart and circulatory physiology* **291,** H1088-1100.

Yang JH & Saucerman JJ. (2012). Phospholemman is a negative feed-forward regulator of Ca2+ in beta-adrenergic signaling, accelerating beta-adrenergic inotropy. *Journal of molecular and cellular cardiology* **52,** 1048-1055.

APPENDIX

Peer Reviewed Journal Publications

Morotti S *, Grandi E *, Summa A, Ginsburg KS & Bers DM. (2012). Theoretical study of L-type Ca^{2+} current inactivation kinetics during action potential repolarization and early afterdepolarizations. *The Journal of Physiology* **590,** 4465-4481.

Ruan Y, Denegri M, Liu N, Bachetti T, Seregni M, **Morotti S**, Severi S, Napolitano C & Priori SG. (2010). Trafficking defects and gating abnormalities of a novel SCN5A mutation question gene-specific therapy in long QT syndrome type 3. *Circulation Research* **106,** 1374-1383. **

Grandi E, **Morotti S**, Ginsburg KS, Severi S & Bers DM. (2010). Interplay of voltage and Ca-dependent inactivation of L-type Ca current. *Progress in Biophysics and Molecular Biology* **103,** 44-50.

Conference Proceedings

Morotti S, Grandi E & Bers DM. A Novel Computational Model of the Murine Ventricular Action Potential Integrating Ca, β-Adrenergic and CaMKII Signaling. *33rd International Society for Heart Research North American Section Meeting*, Banff, AB (CDN), May 28-31, 2012.

Morotti S, Grandi E, Summa A, Ginsburg KS, Severi S & Bers DM. An Improved Model of Voltage- and Ca-dependent Inactivation of the L-type Ca Channels. *Biophysical Society 55th Annual Meeting*, Baltimore, MD (USA), March 5-9, 2011, *Biophysical Journal* (2011) 100(3) S1:571a, 3096-Pos B201.

Morotti S, Grandi E, Summa A, Ginsburg KS, Bers DM & Severi S. An Improved Model of Ba Current through L-type Ca Channels Including Voltage- and Ion-Dependent Inactivation. *Computing in Cardiology*, Belfast (UK), September 26-29, 2010, p.176.

---

* These authors contributed equally to this work.

** Faculty of 1000 Recommended (f1000.com/3209956).

Cenci I, **Morotti S**, Negroni J, Rodriguez B & Severi S. Mechano-Electric Feedback Effects in a Ventricular Myocyte Model Subjected to Dynamic Change in Mechanical Load. *Computing in Cardiology*, Belfast (UK), September 26-29, 2010, p.50.

Morotti S, Ruan Y, Denegri M, Liu N, Bachetti T, Seregni M, Severi S, Napolitano C & Priori SG. Paradoxical Effect of Mexiletine Treatment in LQT3: in Vitro and in Silico Analysis. *2nd National Conference of Bioengineering*, Turin (IT), July 8-10, 2010, pp.117-118.

Awards

"First Contact Initiative Grant" from European Society of Cardiology, November 2010.